Optimisation and Dynamic Effect of Slip Couplers in Geared Wind Drivetrains

by

Juan Joseph Britz

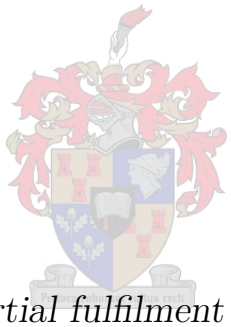

Thesis presented in partial fulfilment of the requirements for the degree of Master of Science in the Faculty of Engineering at Stellenbosch University

Supervisor: Prof. Maarten J. Kamper

April 2019

Declaration

By submitting this thesis electronically, I declare that the entirety of the work contained therein is my own, original work, that I am the sole author thereof (save to the extent explicitly otherwise stated), that reproduction and publication thereof by Stellenbosch University will not infringe any third party rights and that I have not previously in its entirety or in part submitted it for obtaining any qualification.

Date: April 2019 .....

Abstract

Optimisation and Dynamic Effect of Slip Couplers in Geared Wind Drivetrains

J.J. Britz

Department of Electric and Electronic Engineering,
Stellenbosch University,
Private Bag X1, Matieland 7602, South Africa.

Thesis: M.Sc Eng.

March 2019

Two electromagnetic (EM) torque couplers, which are referred to as slip couplers, are designed and optimised to be placed in a 2.2 kW wind turbine drivetrain. These slip couplers make the drivetrain more *robust*, by filtering unwanted torque oscillations. The slip coupler performance is evaluated using EM finite element method (FEM) software, implemented in a `Python/Semfem` script. The slip coupler is a polyphase electric machine, and a *dq* inductance estimation method is used to solve for different static rotor steps iteratively. Both slip coupler designs are optimised using genetic and gradient-based algorithms. The NSGA-II and MMFD optimisation algorithms are utilised in the `Visualdoc` environment, to minimise the total mass of the design. The optimisation constraints and influence of the design variables are evaluated using a colour-graded Pareto and dominated-solution space. One of the slip coupler designs improves upon a similar design found in literature, because the NSGA-II was used together with the MMFD optimisation algorithm. A time-transient analysis of both slip couplers is performed using `Ansys Maxwell`, and the currents and flux-linkage values compare well with `Semfem`. The torque ripple values generated by `Maxwell` casts doubt on some of the results and indicates that another EM-FEM software suite should be used. Finally, the wind turbine is modelled using `Matlab Simulink`, and the unforced and steady-state response to a wind gust and tower shadow component is determined. A two-mass drivetrain model, with flexible shafts going into and out of the gearbox, is tested. In conclusion, a slip coupler, when placed on the turbine side of the drivetrain, reduces higher-frequency torque vibrations and may be a viable wind turbine component in future designs.

Uittreksel

Optimering en Dinamiese Effek van Glip Koppelaars in Geratte Wind Assestelsels

("Optimisation and Dynamic Effect of Slip Couplers in Geared Wind Drivetrains")

J.J. Britz

Departement Elektries en Elektroniese Ingenieurswese,
Stellenbosch Universiteit,
Privaatsak X1, Matieland 7602, Suid Afrika.

Tesis: M.Sc Ing.

Maart 2019

Twee elektromagnetiese (EM) draaimoment-koppelaars, oftewel glipkoppelaars, word ontwerp en ge-optimeer vir gebruik in 'n 2.2 kW wind turbine assestelsel. Die glipkoppelaars maak die assestelsel meer *robuus*, deur ongewensde draaimoment ossilasies te filter. Die glipkoppelaar word ge-evalueer met 'n EM eindige-element metode (EEM) sagteware pakket, wat ge-implementeer word in `Python/Semfem`. Die glipkoppelaar is 'n multifase elektriese masjien, en word ge-analiseer met 'n *dq* induktansie estimasie metode. Dié metode los die strome in die masjien iteratief op, vir statiese rotor stappe. Die NSGA-II en MMFD optimerings algoritmes word toegepas in `Visualdoc` en die totale massa van die masjiene word geminimaliseer. Die optimeringsbeperkinge en invloed van ontwerpsveranderlikes word ge-evalueer deur 'n kleur-gradiëring toepassing op die Pareto- en domineerde-oplossings spasies. Een van die glipkoppelaars verbeter 'n soortgelyke ontwerp in die literatuur, omdat die NSGA-II tesame met 'n MMFD algoritme gebruik was. Die tyd oorgangstoestand van beide glipkoppelaars word gesimuleer in `Ansys Maxwell`, en die stroom- en vloedomsluitingswaardes lyk eenders as dié van `Semfem`. Weens 'n verskil in `Maxwell` se draaimoment-riffel waardes, word 'n ander EM-EEM sagteware pakket voorgestel vir verifiering. Laastelik, die wind turbine word gemodelleer in `Matlab Simulink` en die vry- en bestendige assestelsel reaksie tot rukwind en toringskadu toestande word gesimuleer. 'n Twee-massa model, met buigbare aste wat aan weerskante van die ratkas sit, word getoets. Ten slotte, 'n turbine-kant glipkoppelaar verminder hoër-frekwensie draaimoment vibrasies wat op die aste inwerk, en dié ontwerp kan moontlik 'n aanwins in enige wind turbine stelsel wees.

Acknowledgements

I would very my much like to thank the following people and institutions for their support:

Prof. Maarten Kamper, my supervisor, for his guidance and always ensuring that funding was made available.

Udochukwu Akuru, for being a very needed sounding board and always saying: "It may feel like you are going through this alone, but don't worry, we've all been there".

Mkhululi Mabhula, for always being willing to listen, and for providing me with that *final* piece of insight I needed to finish this study.

Monique Hugo, for always understanding, and constant support, encouragement and love.

My parents, for their continued support throughout my years of studying.

I acknowledge that without Jesus Christ, my Lord and King, none of this would be possible.

The author would like to sincerely thank the National Research Fund for their financial contribution towards this study.

Dedications

Vir my twee Oupas:

For my two Grandads:

Cas Britz & Hannes van der Bank

Contents

List of Figures

List of Tables

Nomenclature

Electric machines

B	Magnetic flux density	$[\mathrm{T}]$
f	Frequency	$[\mathrm{Hz}]$
H_c	Magnetic coercivity	$[\mathrm{A \cdot m^{-1}}]$
i	Instantaneous current	$[\mathrm{A}]$
I	Steady-state current	$[\mathrm{A}]$
J_c	Current density	$[\mathrm{A \cdot mm^{-1}}]$
L_{dq}	Steady-state dq inductance	$[\mathrm{H}]$
λ_{dq}	Steady-state dq flux-linkage	$[\mathrm{Wb-turns}]$
λ_m	PM flux contribution	$[\mathrm{Wb-turns}]$
μ_r	Relative permeability	$[-]$
n_i	Number of iterations	$[-]$
n_s	Number of static rotor steps	$[-]$
n_{sl}	Rotational slip speed	$[\mathrm{rpm}]$
N_P	Number of stator poles	$[-]$
N_S	Number of rotor slots	$[-]$
P_C	Conductor loss	$[\mathrm{W}]$
P_{fe}	Core loss	$[\mathrm{W}]$
P_w	Total wind power	$[\mathrm{W}]$
R_C	Per phase winding resistance	$[\Omega]$
T	Torque	$[\mathrm{N \cdot m}]$
ΔT_{ripple}	Torque ripple	$[\%]$
ρ_τ	Specific torque	$[\mathrm{N \cdot m \cdot kg^{-1}}]$
θ_{rotor}	Mechanical rotor angle	$[\mathrm{rad}]$
θ_S	Mechanical slot angle	$[\mathrm{rad}]$
θ_{Se}	Electrical phase angle	$[\mathrm{rad}]$
v	Instantaneous voltage	$[\mathrm{V}]$

Modelling

b	Dissipation constant	$[\mathrm{N \cdot m \cdot s \cdot rad^{-1}}]$
C_{sc}	Slip coupler constant	$[\mathrm{N \cdot m \cdot s \cdot rad^{-1}}]$
G	Modulus of rigidity	$[\mathrm{Pa}]$
G_R	Gear ratio	$[-]$
Γ	Time constant	$[\mathrm{s}]$
J	Mass moment of inertia	$[\mathrm{kg \cdot m^2}]$
J_{sh}	Shaft polar moment of inertia	$[\mathrm{m^4}]$
K_{sh}	Shaft stiffness constant	$[\mathrm{N \cdot m \cdot rad^{-1}}]$
ω	Rotational speed	$[\mathrm{rad \cdot s^{-1}}]$
Ω	Rotational speed	$[\mathrm{rad \cdot s^{-1}}]$
τ	Torque	$[\mathrm{N \cdot m}]$

Optimisation

m	Component mass	$[\mathrm{kg}]$
t_{sol}	Computation time for single solution	$[\mathrm{s}]$
α_k	Accepted step length from line search	
$\mathcal{F}$	Feasible subset	
H	Hessian matrix	
N	Population size	
n_o	Number of objective function evaluations	
n_x	Number of decision variables	
n_I	Number of optimisation algorithm iterations	
$\mathcal{O}$	Objective subset	
$\mathcal{P}*$	Pareto-optimal set	
P_{cr}	Probability of cross-over	
$\boldsymbol{p}_k$	Search vector for major iteration k	
P_{mu}	Probability of mutation	
$\mathbb{R}^{n_O}$	Objective space	
$\mathbb{R}^{n_x}$	Decision space	
$\mathcal{S}$	Search subset	
$\boldsymbol{x}$	Decision vector	

Wind energy

A_t	Turbine swept blade area	$[\mathrm{m}^2]$
β	Blade pitch angle	$[\mathrm{rad}]$
C_p	Turbine power coefficient	$[-]$
E_w	Available energy in the wind	$[\mathrm{J}]$
η_b	Betz' limit	$[-]$
λ_t	Tip speed ratio	$[-]$
$\dot{m}_v$	Fluid mass flow rate	$[\mathrm{kg} \cdot \mathrm{s}^{-1}]$
ρ_v	Fluid density	$[\mathrm{kg} \cdot \mathrm{m}^{-3}]$
R_t	Turbine rotor radius	$[\mathrm{m}]$
v_w	Instantaneous wind speed	$[\mathrm{m} \cdot \mathrm{s}^{-1}]$
V_h	Wind velocity at hub height	$[\mathrm{m} \cdot \mathrm{s}^{-1}]$

Subscripts

A	Active mass
B	Breakdown
C	Conductor
dq0	Direct-, quadrature- and zero-axis
e	Electrical
g	Generator
R	Rotor
S	Stator
sc	Slip coupler
sh	Shaft
sl	Slip
sle	Electrical slip speed
t	Turbine
w	Wind

Abbreviations

AGE	Air gap element
EM	Electromagnetic
FE	Finite element
FEM	Finite element method
FEA	Finite element analysis

MMFD Modified method of feasible direction

MOO Multi-objective optimisation

MOP Multi-objective problem

NSGA Non-dominated sorting genetic algorithm

PM Permanent magnet

SG Synchronous generator

S-PMC Slip permanent magnet coupler

Chapter 1

Introduction

Small-scale wind turbines (< 100 kW) need to be robust, especially when they are erected in areas where skilled maintenance crews are not readily available. A robustly designed wind turbine can operate under various weather and grid conditions without failure. Adding too much strength to a drivetrain causes the *nacelle*, or enclosed turbine unit, to be too bulky. For large wind turbines, too much weight is detrimental. Wind turbine drivetrains experience unwanted torsional vibrations and are an inevitable design consideration in any power producing system. Various torque coupler designs have been proposed to mitigate these torsional vibrations, in the hope of increasing the wind turbine system lifetime. An electromagnetic torque coupler, which can minimise these torsional vibrations, is proposed in this thesis.

The torque coupler operates under the principle of *slip*, which means that electromagnetic torque is produced when there is a speed difference between the two rotating parts of the coupler. This torque is produced by the magnetic field interaction between a conductive material and surface mounted permanent magnets (PMs). For this reason, the torque coupler is referred to as a slip coupler.

Slip couplers, which operate using PM material, has the potential to be cost effective due to the ever decreasing cost of ferromagnetic materials. However, herein lies the second problem that all wind turbine designers face: how small can the design be without compromising its performance? Lowered mass means cost reductions but, generally, also a reduction in power output or efficiency if the turbine components are designed carelessly. Design optimisation is an inevitable component of a well-designed slip coupler, and minimising the total mass of the slip coupler is of primary concern.

In this chapter, a brief history of torque couplers in the context of wind turbines is presented. Some of the standard wind turbine concepts used in the thesis are clarified, and the objectives of this study are discussed. Finally, the thesis outline is shown.

1.1 Electromagnetic torque couplers

Electromagnetic torque couplers are by no means a recent concept. Prototype synchronous torque couplers have been investigated as early as 1976 [2, 3], due to the availability of PM material. Electromagnetic torque couplers fall into two broad categories, namely asynchronous and synchronous torque couplers. Both of these types of torque couplers are categorised by an absence of contact between the two rotating parts and make use of PMs. An asynchronous type torque coupler functions by use of eddy currents induced in a conductive material. These asynchronous slip couplers can be subdivided into axial and radial type couplers [4]. Figure 1.1 shows a radial eddy-current coupler as designed in [5].

Synchronous type torque couplers are typically machines where both halves are fitted with PMs. Both halves move at the same speed, as long as there is a relative positional difference between these two halves [6]. An early example of a synchronous torque coupler is shown in Figure 1.2. There are also hybrid torque couplers, which have characteristics of both asynchronous and synchronous couplers. A hysteresis torque coupler is an example of such a machine [7].

Regardless of the type of coupler, they act as low-pass filters by removing torque oscillations which are typically present in any mechanical drivetrain. Previously, this concept was adapted to a direct-drive wind turbine, by combining the PM torque coupler and PM synchronous generator (PMSG) into a single unit [8]. There, the torque coupler is also referred to as a slip PM coupler (S-PMC). Later on, the decision was made to separate the generator and coupler designs to accommodate a geared wind turbine drivetrain. The polyphase slip coupler design in this thesis is a continuation of the extensive research done in [1]. Figure 1.3 shows the slip coupler with a fundamental pole-to-slot ratio of 14:15. Each winding is considered a complete electrical phase, and each PM a single pole. The winding arrangement is known as a side-by-side topology. The number of poles is an important consideration because it directly determines the electrical slip frequency of the slip coupler. The pole-to-slot ratio directly relates to what is known as the winding factor [9]. In the case of a non-overlap winding PM machine, a higher winding factor is related to a lower torque ripple component. Therefore, the fundamental 14:15 is an excellent choice for a slip coupler.

In this thesis, there are two slip coupler designs based on the 14:15 pole-to-slot ratio, namely the 28:30 and 84:90 slip couplers. These two slip couplers are placed on either side of a geared wind drivetrain. The performance of these slip couplers is evaluated in the subsequent chapters of the thesis.

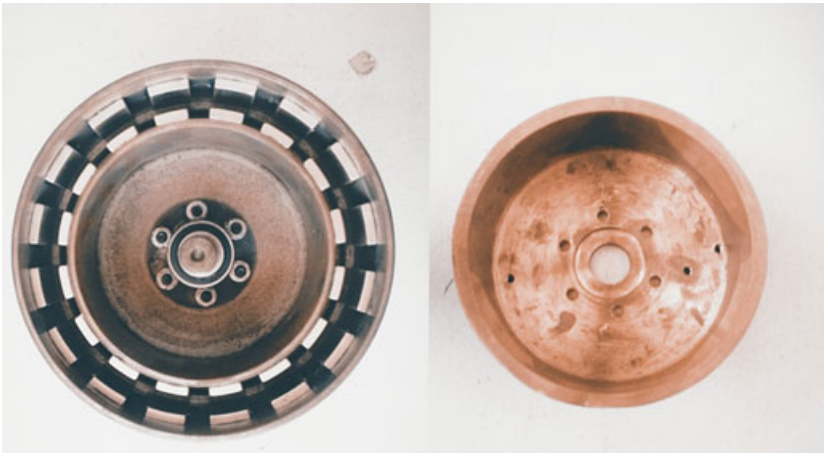

Figure 1.1: Typical radial asynchronous electromagnetic coupler, showing the radial magnet outer part (left) and inner conductive ring (right). Image found in [5].

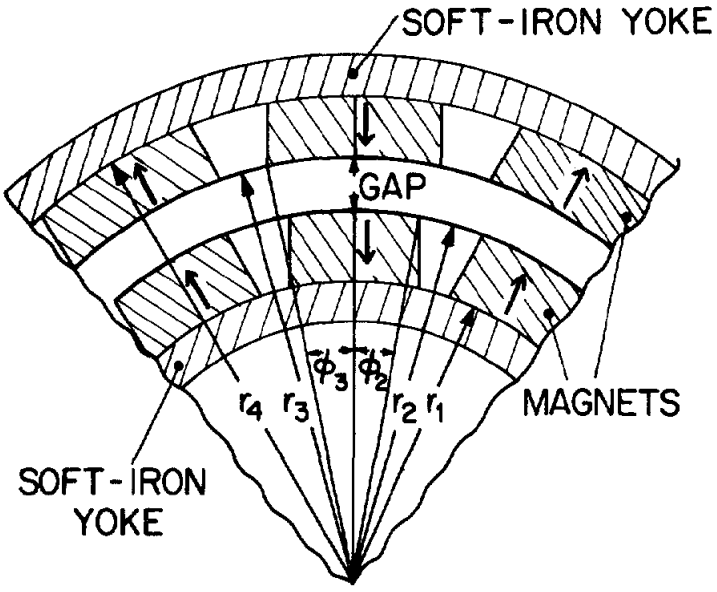

Figure 1.2: Example of radial synchronous electromagnetic coupler, developed in 1978. Image found in [3].

1.2 Aspects of small-scale wind turbines

In this section, the universal aspects of a small-scale wind turbine are discussed. This discussion includes a brief look at standard small-scale wind turbine components, an overview of wind energy, and finally a description of the slip coupler placements in the wind turbine drivetrain.

1.2.1 Common drivetrain components

The wind turbine which is used as a case study in this thesis is classified as a 2.2 kW, horizontal axis wind turbine (HAWT). Figure 1.4 shows a diagram of a typical HAWT

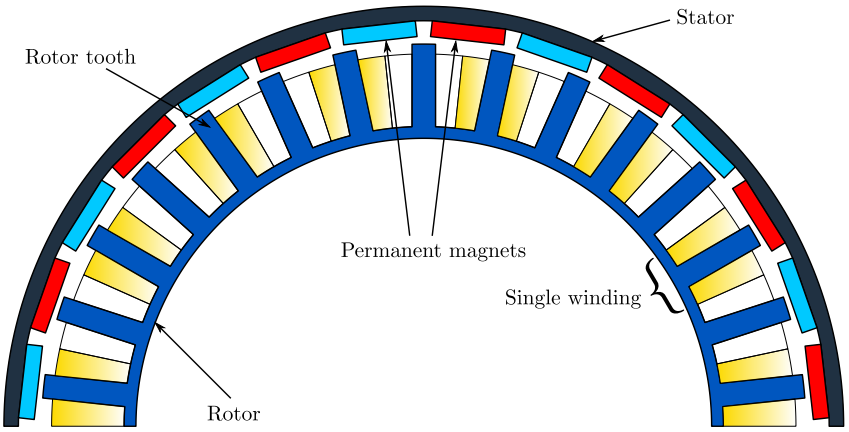

Figure 1.3: Slip coupler terminology, showing the fundamental pole-to-slot ratio of 14:15.

and indicates some of the standard terminology used in the wind energy industry. This wind turbine has three blades, which is common in most modern turbines due to the balance between efficiency and cost (more blades increase the power yielded from the wind, but also increases costs). The slip coupler is shown fixed to the rotor hub of the turbine with a shaft connecting the slip coupler to a planetary gearbox. Planetary gearboxes are a common feature in wind turbines because the operating speed can be increased, which means the generator size is also reduced. Helical gearboxes are not uncommon, but planetary gearboxes are preferred due to their more compact size. When many gearboxes are connected in series, it is referred to as a gear train. Gear trains are typical, especially when high gear ratios (> 10) need to be achieved [10]. The wind turbine gearbox in this study has a gear ratio of $G_R = 1 : 3.78$.

When modelling a wind turbine drivetrain, a trade-off exists between accuracy and complexity. Two-mass and three-mass drivetrain models are more commonplace [11–13]. In this study, a two-mass model with flexible shafts, gearbox and slip coupler is modelled.

1.2.2 Wind energy concepts

In this section, the basic principles of wind energy generation are discussed, and two examples of common wind disturbances are presented. The total amount of kinetic energy extracted from the wind is determined by the instantaneous wind speed, size- and type of wind turbine blades. The total kinetic energy is

$$E_w = \tfrac{1}{2}\dot{m}{V_h}^2, \tag{1.1}$$

where $\dot{m}_v$ is the fluid mass flow rate expressed as

$$\dot{m}_v = A_t \rho V_h, \tag{1.2}$$

where

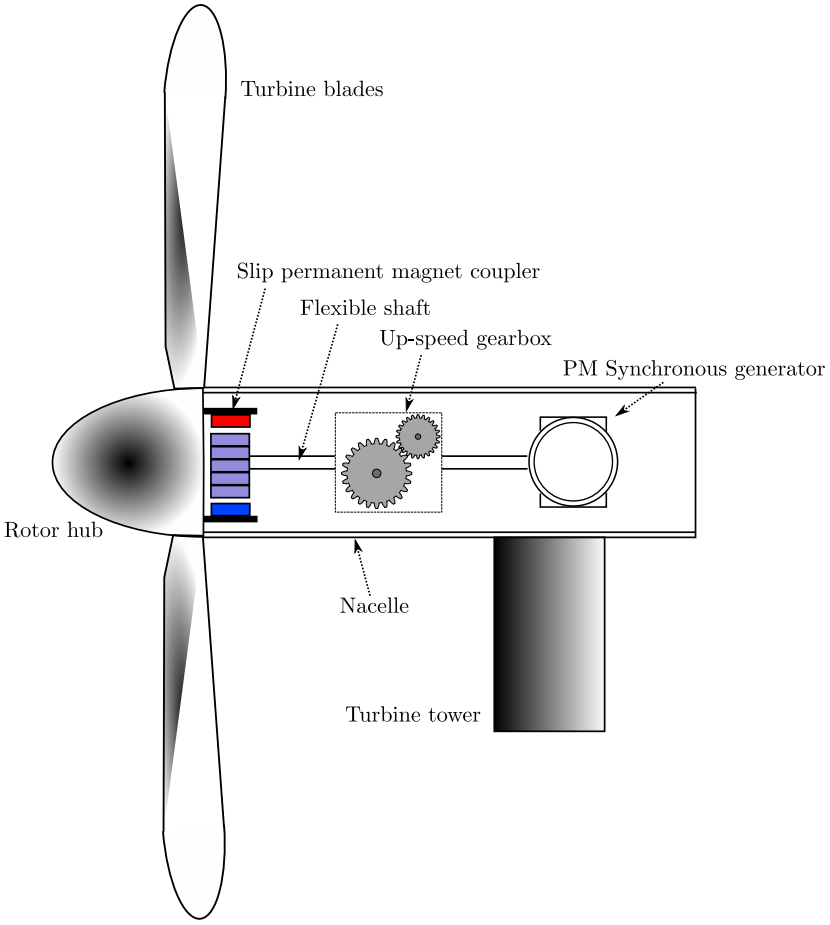

Figure 1.4: Typical aspects of a HAWT turbine.

A_t = Turbine swept blade area,
ρ_v = Fluid density,
V_h = Velocity of wind at hub height.

The total power available in the wind is expressed as

$$P_w = E_w \dot{m}_v = \tfrac{1}{2}\rho_v A_t V_h^3. \tag{1.3}$$

It is not possible to harvest the total available energy in the wind. Albert Betz, a German physicist, proved that wind turbines have a maximum theoretical efficiency limit. This efficiency is proven to be $\eta_b = 16/27 = 59.3\%$ [14]. The total available power in the wind is sensitive to changes in wind speed, as shown in Eq. (1.3). The turbine power coefficient, C_p, is a measure of a turbine's ability to extract power from the wind. The power coefficient is a function of the blade pitch angle, β and tip speed ratio λ_t. For a typical wind turbine, C_p is equal to the Betz limit η_b. Utilising Eq. (1.3), the power produced by the turbine is

$$P_t = C_p P_w = \tfrac{1}{2}\rho A_t C_p(\lambda_t, \beta) V_h^3, \tag{1.4}$$

where the tip-speed ratio is defined as

$$\lambda_t = \frac{R_t \Omega_t}{V_h}, \tag{1.5}$$

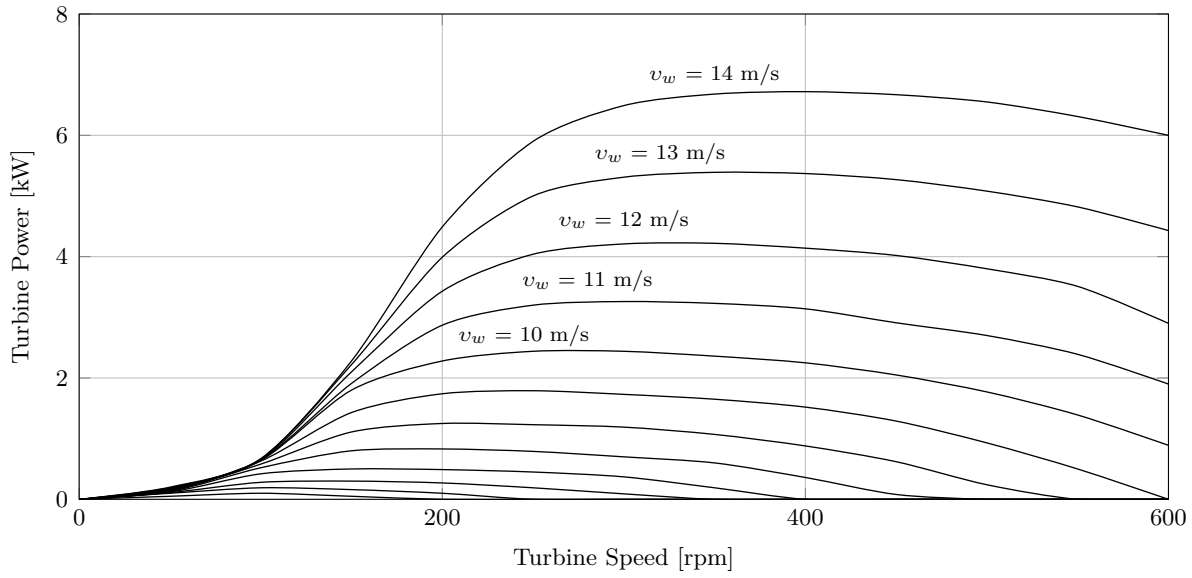

Figure 1.5: Turbine power versus turbine speed for $v_w = 1$ to 14 m $\cdot$ s^{-1}.

and

R_t = Turbine rotor radius,
Ω_t = Angular speed of the rotor.

Figure 1.5 shows the mechanical turbine power vs turbine rotational speed curve, which is constructed using Eq. (1.4). There are some wind disturbances which affect power generation. Of these, wind gust is very common [15]. Figure 1.6 (a) shows a typical wind gust waveform over time. When considering Eq. (1.4) it should be clear that the power generation is directly affected by a wind gust. Due to the transient nature of a gust, it also does not contribute to sustained power generation. Another disturbance is a component known as tower shadow interference. The disturbance in the wind due to the tower shadow depends on the blade radius, instantaneous blade position and hub distance from the tower [16]. The tower momentarily obstructs wind flow, causing a sudden loss in power. Figure 1.6 (b) shows an example of how the wind flow is affected by tower shadow. A slip coupler should ideally be able to minimise or completely remove both of these two wind disturbance components.

1.2.3 Slip coupler placements in drivetrain

The principal purpose of the slip coupler is to remove unwanted higher-frequency vibrational torque components in the drivetrain. These components originate either on the turbine or generator side of the gearbox. Figure 1.7 shows the possible slip coupler placements along the drivetrain of the wind turbine. Each slip coupler has to be designed and optimised due to their specific placements along the drivetrain. The performance criteria, such as torque and speed output, needs to be selected.

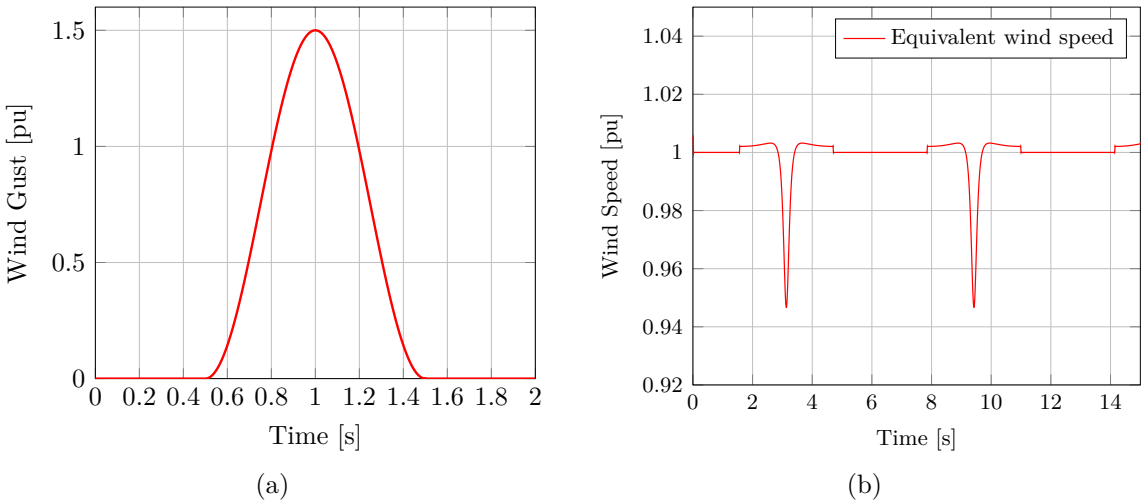

(a) (b)

Figure 1.6: Common wind disturbances, showing (a) a typical wind gust over a given period of time and (b) the tower shadow interference which affects the wind-flow experienced by the turbine.

1.3 Objectives and scope of research

In this thesis, a trusted method of evaluating the performance of the slip coupler is applied to two different designs for a small-scale wind turbine. The slip coupler designs are optimised with the objective of minimising the total mass using genetic and gradient-based optimisation algorithms. As will be shown, genetic algorithms are superior in their ability to find true global objective minima. Figure 1.8 shows the basic optimisation procedure proposed in this thesis. The slip coupler designs are validated using commercial software, and the benefits of placing the slip coupler in a wind turbine drivetrain are evaluated. The specific objectives include:

- Understanding the core electromagnetic concepts behind slip coupler design and estimating the performance using a software script. The script makes use of a proven solution method and uses an electromagnetic FEM module developed at `Stellenbosch University`. The software utilised include `Python` and `Semfem`.
- Evaluating the ideal number of rotor positions needed to obtain an accurate solution and efficiently generating a geometric mesh to reduce the script simulation time as far as possible.
- Evaluation of gradient and genetic-based optimisation algorithms, based on the Pareto-front generation and design objectives of the slip couplers. The main optimisation objective is to minimise the total slip coupler mass. The optimisation is limited to the NSGA-II and MMFD algorithms.
- To compare the optimisation results of the side-by-side winding slip coupler with the top-bottom winding slip coupler found in [1].

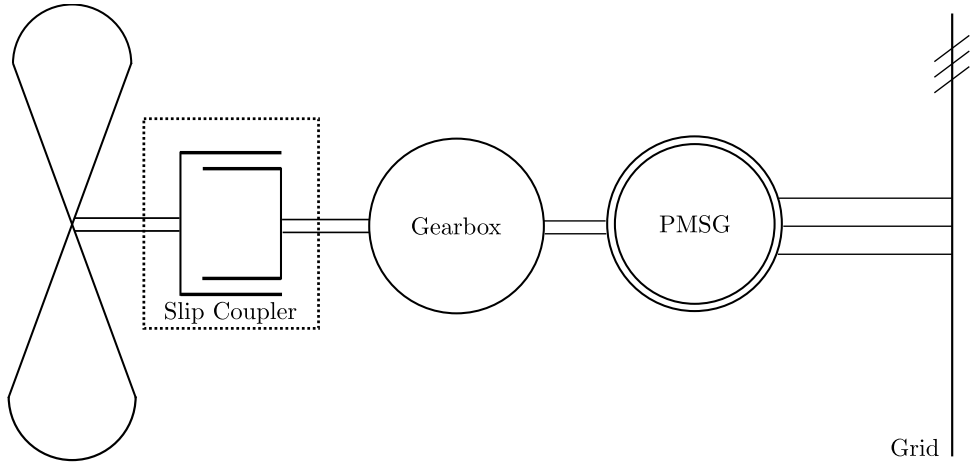

(a)

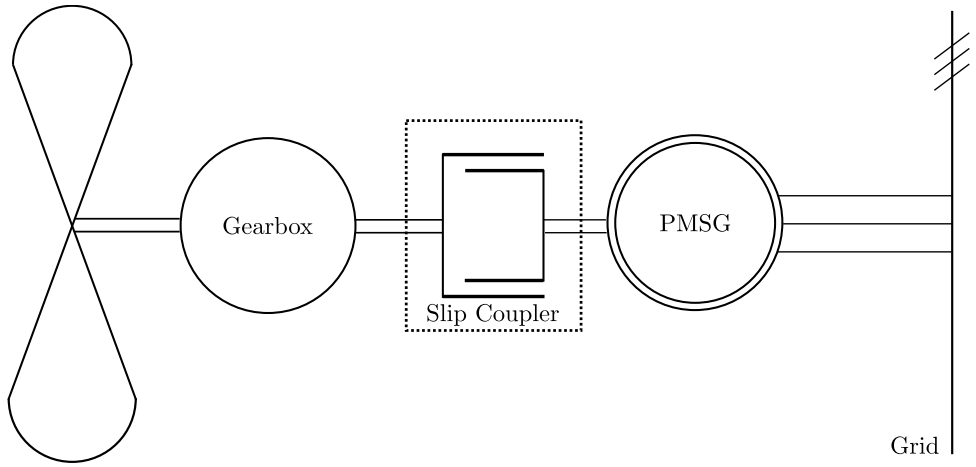

(b)

Figure 1.7: Wind turbine drive train with a slip coupler on (a) the turbine-side and (b) the generator-side of the gearbox.

- To verify the performance of the slip couplers using the `Ansys Maxwell` software, which is commercially available and widely used in electric machine design. The verification includes comparing the torque, current and flux-linkage magnitude and waveforms produced by `Semfem` and `Maxwell`.
- Simulation of the small-scale wind turbine in `Matlab Simulink`. The simulation includes the unforced response evaluation, investigating the effect of the gearbox gear ratio and steady-state response to wind disturbances. The wind turbine is simulated with and without a turbine-side slip coupler, to determine its advantages.
- The steady-state simulations are limited to a simple wind gust disturbance and tower shadow interference. The turbine simulations are focussed on the torque transfer in the shafts leading into and out of the gearbox, as well as the generator torque response.

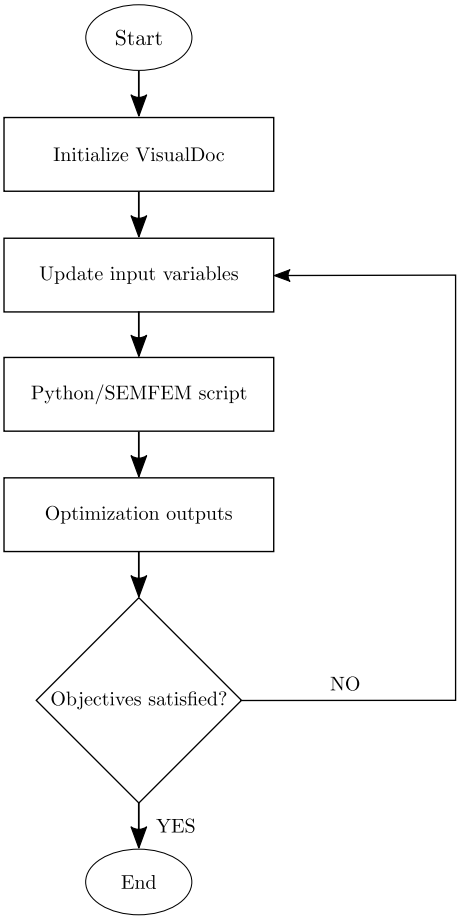

Figure 1.8: General optimisation procedure using `Visualdoc` linked with `Python/Semfem` script.

1.4 Thesis outline

The remaining chapters of this thesis are structured in the following way:

- **Chapter 2:** The performance of the two slip coupler designs is evaluated using electromagnetic FEM software. The methodology is explained, and some of the factors that influence the performance and accuracy of the FEM solutions are investigated. These factors include the number of iterations needed to converge to an accurate solution, the number of static rotor position evaluations and the airgap mesh fineness.

- **Chapter 3:** The total mass of the slip couplers is minimised using the NSGA-II and MMFD optimisation algorithms. This includes generating a Pareto-optimal front for both slip coupler designs. The influence of the design variables on the constraints and performance of the optimisation outcomes are determined. The ideal machine sizes are determined and discussed.

- **Chapter 4:** The two slip coupler designs are verified using a time-transient analysis in `Ansys Maxwell`. The slip coupler performance at operating speed is verified, which

includes generating the torque, torque ripple, flux-linkage and current waveforms. Also, the slip coupler performance over a wider range of slip speeds is determined, and compared with the `Semfem` results.

- **Chapter 5:** The turbine-side slip coupler (84:90) is simulated in a 2.2 kW wind turbine as a case study. This includes a discussion on the individual components of the wind turbine model. The unforced response to a turbine-side pulse is investigated, along with the effect of changing the gear ratio on the system response. The turbine is simulated at steady-state, and the effect of a wind gust and tower shadow interference on the system is evaluated.
- **Chapter 6:** Conclusions and recommendations are made based on the outcomes of the thesis results.
- **Appendix A:** The Park's transformation equations are presented for quick reference.
- **Appendix B:** Winding resistance calculation and end-winding inductance equations are presented. These calculations are used in Chapters 2 and 3.
- **Appendix C:** Various wind drivetrain model equations of motion are derived and presented. This includes the final two drivetrain models used in the simulations in Chapter 5.
- **Appendix D:** The transfer functions, derived from the equations in Appendix C, is presented. These transfer functions are evaluated in Chapter 5.
- **Appendix E:** The inductance estimation algorithm, as implemented in `Python/Semfem`, is presented.

Figure 1.9: Small-scale wind turbine at `Stellenbosch University`.

1.5 Concluding remarks

Small-scale wind turbines need to be robust, and two slip coupler designs are proposed which can potentially minimise unwanted torque oscillations in the drivetrain. The proposed slip coupler is a continuation of an existing design, but instead of a top-bottom winding topology, the two slip couplers have a side-by-side winding topology. The two slip coupler designs are optimised for the 2.2 kW turbine shown in Figure 1.9, which means proper selection of the performance criteria and minimising the total mass of the two couplers. Two common wind disturbance components are going to be modelled, and a two-mass model is selected to evaluate the performance of the system as a whole. This system has a turbine-side slip coupler placed along the drivetrain. In the following chapter, the performance of the slip coupler is determined, along with the simulation requirements of the `Python/Semfem` script.

Chapter 2

Electromagnetic Slip Coupler Performance

In this chapter, the application and performance calculation of an electromagnetic torque coupler is discussed. The performance calculation is implemented using FE software. This electromagnetic torque coupler is usually referred to as a slip permanent magnet coupler (S-PMC), or merely a slip coupler. Figure 2.2 shows the slip coupler type and placement along the 2.2 kW wind turbine drivetrain. The equivalent electrical circuit, machine topology, parameter calculations such as torque, efficiency, losses, inductances and flux linkages are determined. The FE software uses an iterative inductance calculation method, and the accuracy and computation considerations of the software are discussed. Finally, the FE mesh fineness is investigated to determine the ideal mesh setup.

2.1 Slip coupler concept

As mentioned in Chapter 1, the slip coupler concept is a continuation of the work done in [1] and [17]. The slip coupler design operates similarly to an induction machine. Torque is produced due to an electric speed difference between the rotating magnetic flux in the stator and the induced magnetic field in the rotor. The stator of the slip coupler consists of surface mounted PMs, referred to as poles. The windings of the rotor are phase separated, placed side-by-side and each is short-circuited. Although electrical energy is produced due to the relative motion of the rotor and stator, only mechanical energy is transferred to the drivetrain of the wind turbine. The main benefit of a slip coupler is that it acts as a low pass filter in a mechanical system, filtering out any unwanted higher-frequency vibrational components. Besides, the slip coupler does not add significant losses to the system when operating at low slip speeds.

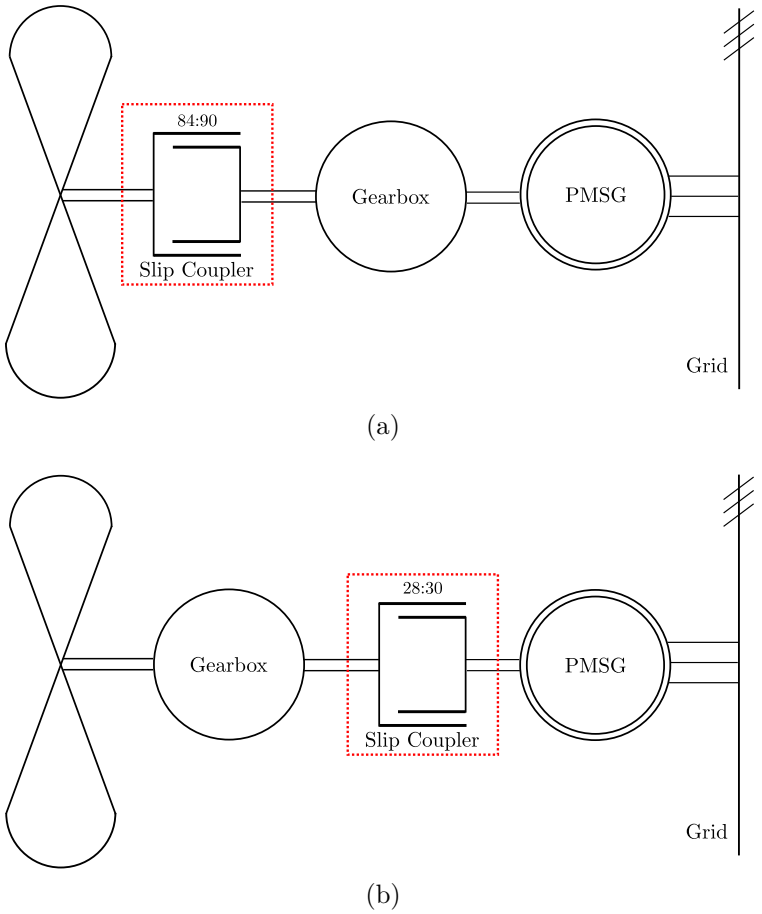

Figure 2.1: Wind turbine drivetrain with a (a) 84:90 slip coupler on the turbine-side and (b) 28:30 slip coupler on the generator-side of the gearbox.

2.1.1 Machine topography and winding selection

Figure 2.2 shows the 28:30 and 84:90 slip coupler designs. The relative sizes are determined in Chapter 3. The slip coupler needs to rotate at the correct slip speed, which is determined by the number of PM poles of the stator. A fundamental pole-to-slot ratio of N_P:N_S = 14:15 is chosen, and each slip coupler is a multiple of that ratio. Therefore, the 28:30 slip coupler is twice the fundamental ratio, and the 84:90 slip coupler is six times the ratio. The winding factor of this fundamental ratio is 0.952, as determined in [9], which in turn determines the torque ripple component at steady-state operation. The electrical slip frequency at rated operating speed needs to be below 5 Hz [17] and is expressed as

$$f_{sl} = \frac{n_{sl} N_P}{120}, \tag{2.1}$$

where n_{sl} is the slip speed of the slip coupler. Higher slip frequencies will result in a higher induced winding current, which causes heat to be generated and thereby degrades the performance of the slip coupler. Higher slip frequencies also introduce unacceptably high losses in the wind turbine drivetrain. Using Eq. (2.1), the 28:30 slip coupler frequency is calculated to be 3.15 Hz and the 28:30 slip coupler at 4.2 Hz.

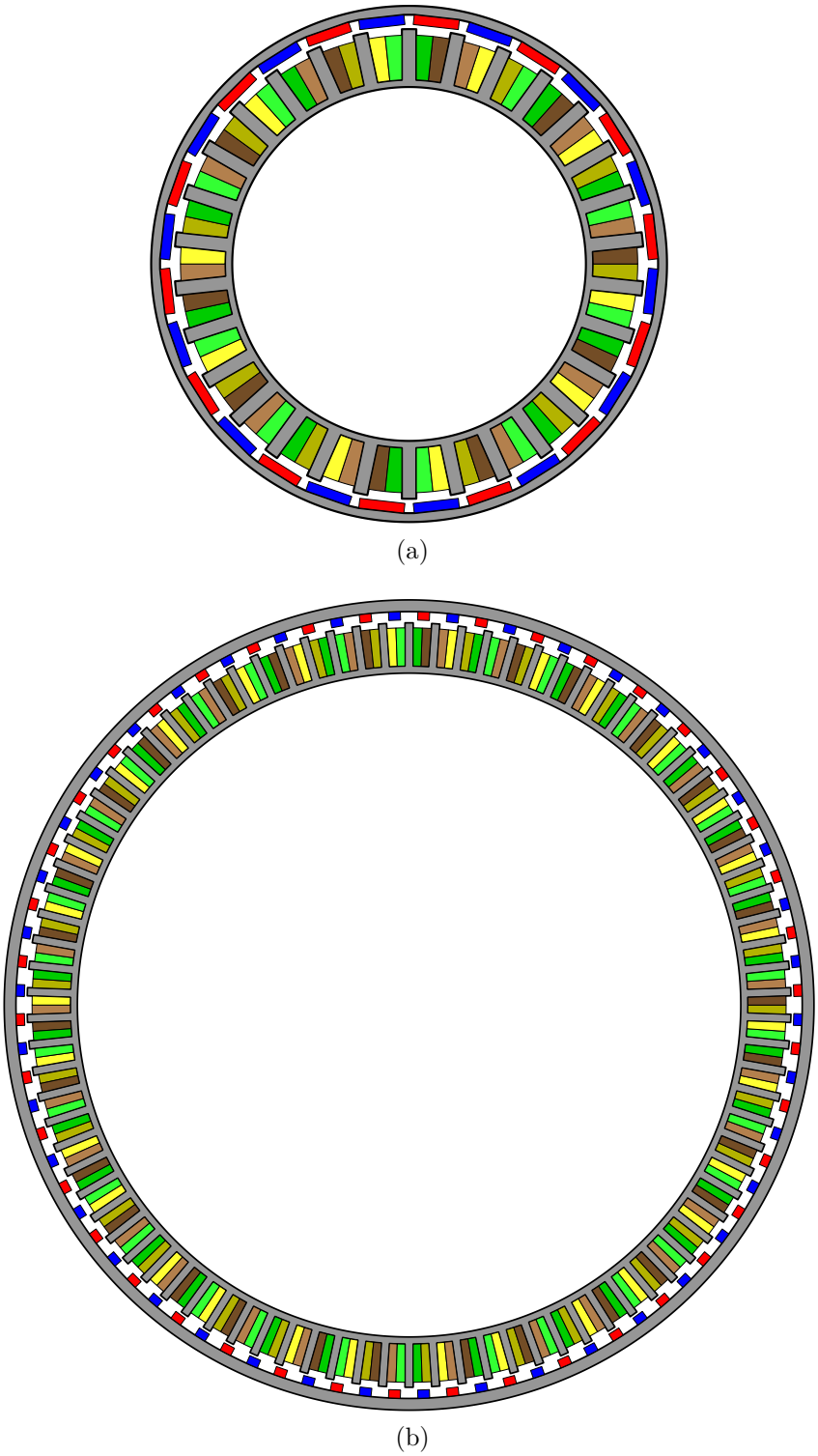

(a)

(b)

Figure 2.2: Slip coupler sectional views and relative size difference between the (a) 28:30, generator-side slip coupler and (b) the 84:90, turbine-side slip coupler.

2.2 Derivation of equivalent circuit

In this section, some simplifications and assumptions are shown that simplifies the analysis of the slip coupler performance. The winding current assumptions are discussed, as well as the torque calculation. The software used to make these calculations is introduced. All of the methods presented here have been developed in [1].

2.2.1 Slip coupler currents

As mentioned previously, both slip couplers have a side-by-side rotor winding topology, with each coil isolated from its neighbour, and the end-windings short-circuited. The peak current in each winding is assumed to be equal, such that when the slip coupler is operating at steady-state speed, the dq currents are

$$I_{d,1} = I_{d,2} = ... = I_{d,i}, \tag{2.2}$$

$$I_{q,1} = I_{q,2} = ... = I_{q,i}, \tag{2.3}$$

where $I_{d,i}$ and $I_{q,i}$ is the direct- and quadrature axis current for the i^{th} phase set of the slip coupler. A slip coupler is inherently a polyphase machine, with each winding being an independent phase. Therefore, the number of phases is equal to the number of rotor slots N_S. Figure 2.3 shows the current orientation (in or out of the coil) as defined in the FE program. Figure 2.4 shows the vector diagram for the currents flowing in the slip coupler. Each phase is separated by the electrical angle

$$\theta_{Se} = \frac{N_P}{2}\theta_S, \tag{2.4}$$

where

θ_{Se} = Electrical phase angle,
N_P = Number of PM poles,

and the slot angle is defined as $\theta_S = \frac{2\pi}{N_S}$.

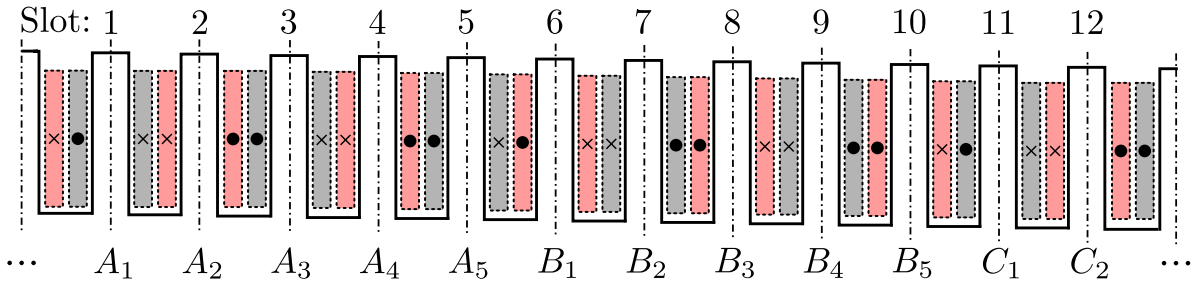

Figure 2.3: Slip coupler side-by-side topology, showing phases A_1 to C_2 and current orientation in windings.

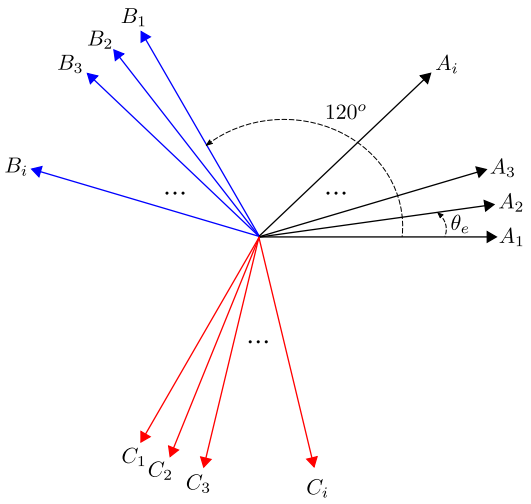

Figure 2.4: Multiphase current vector diagram, grouped into three-phase sets, indicating slot angle θ_{Se}

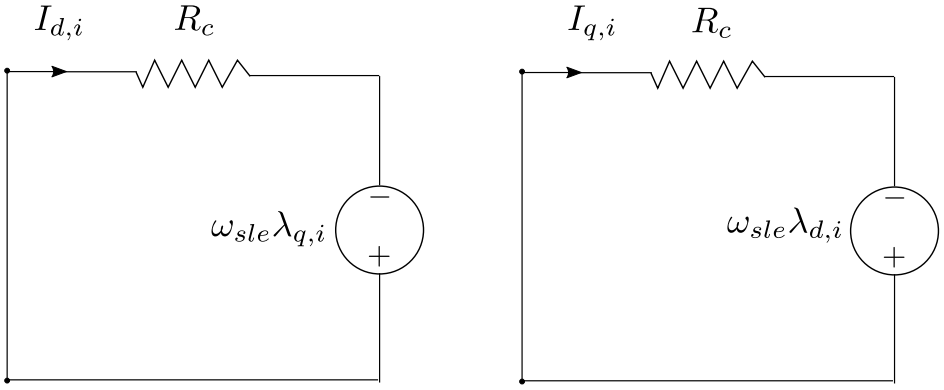

Figure 2.5: Steady-state dq equivalent electric circuits.

2.2.2 Electromagnetic torque production

The FEA is implemented in `Python`, which uses a module named `Semfem` [18]. `Semfem` is an accurate and powerful FE program capable of solving electrical machine currents, voltages and other machine performance parameters using built-in FEM technology. It is capable of accurately solving the polyphase slip coupler currents and other parameters required to evaluate the slip coupler. To do so, we will assume that the slip coupler winding currents are perfectly sinusoidal and are grouped into balanced, three-phase pairs. The abc reference frame currents can then be obtained using standard dq reference frame transformation equations. Furthermore, we will assume that the slip coupler is operating at steady-state speed. Therefore, any time-derivative component is zero. Figure 2.5 shows the dq equivalent electric circuit of the slip coupler. For general analysis, van Wyk and Kamper [1] have shown that the steady-state equations for the slip coupler can be expressed as

$$0 = R_c I_{d,i} - \omega_{sle}\lambda_{q,i}, \tag{2.5}$$

$$0 = R_c I_{q,i} - \omega_{sle}\lambda_{d,i}, \tag{2.6}$$

where

$\lambda_{dq,i} = dq$ Flux linkages,
R_c = Per phase winding resistance,

and the electrical speed is expressed as $\omega_{sle} = \frac{N_P}{2} \cdot (\omega_{in} - \omega_{out})$. Also, the dq flux linkages are

$$\lambda_{d,i} = L_{d,i} I_{d,i} + \lambda_{m,i}, \tag{2.7}$$
$$\lambda_{q,i} = L_{q,i} I_{q,i}, \tag{2.8}$$

where

$L_{dq,i} = i^{th}$ dq inductance values,
λ_m = Flux contribution due to the presence of the PMs.

When Eq. (2.5)–(2.8) are combined, the dq currents can be expressed as

$$I_{d,i} = \frac{-\omega_{sle}^2 (L_{q,i} + L_e)\lambda_{m,i}}{R_c^2 + \omega_{sle}^2 (L_{q,i} + L_e)(L_{d,i} + L_e)}, \tag{2.9}$$
$$I_{q,i} = \frac{-\omega_{sle}^2 R_c \lambda_{m,i}}{R_c^2 + \omega_{sle}^2 (L_{q,i} + L_e)(L_{d,i} + L_e)}. \tag{2.10}$$

Finally, the torque for a single three-phase set is expressed in the dq reference frame as

$$T_{dq,i} = \left(\frac{2}{3}\right)\left(\frac{N_P}{2}\right)(\lambda_{d,i} I_{q,i} - \lambda_{q,i} I_{d,i}). \tag{2.11}$$

Remembering that the slip coupler is a polyphase machine, divided into $N_S/3$ number of three-phase circuits, the total torque generated by the slip coupler at a given slip may be expressed as

$$T_{sc} = \sum_{i=1}^{N_S/3} \frac{3}{2}\left(\frac{N_P}{2}\right)(\lambda_{d,i} I_{q,i} - \lambda_{q,i} I_{d,i}). \tag{2.12}$$

2.3 Slip coupler losses

In this section, the slip coupler core-, friction- and conductor losses are briefly discussed. Firstly, the core loss in an electric machine, according to Steinmetz, can be expressed as

$$P_{fe} = C_{SE} f^{\alpha_S} B_{max}^{\beta_S}, \tag{2.13}$$

where

P_{fe} = Time averaged core loss per volume,
f = Frequency,
B_{max} = Peak flux density,
$C_{SE}, \alpha_S, \beta_S$ = Steinmetz coefficients.

The conductor losses, or ohmic losses, is the sum of each three-phase loss component. The conductor losses are

$$P_c = \sum_{i=1}^{N_p/3} 3{I_{RMS}}^2 R_c, \tag{2.14}$$

where

$${I_{RMS}}^2 = \frac{{I_{d,i}}^2 + {I_{q,i}}^2}{2}. \tag{2.15}$$

The rotor winding resistance equation, R_c, is shown in Appendix B. As shown in the previous section, both slip couplers have slip frequencies of below 5 Hz, and the peak magnetic flux density values are expected to be $|B_{max}| < 2$ T. Therefore, it is expected that $P_{fe} << P_c$ and for this reason, the core losses are neglected in the analysis. The friction losses are neglected due to the low slip speeds of machines. Figure 2.6 shows the power flow diagram of the slip coupler. From Eq. (2.14), the output power of the slip coupler is defined as

$$P_{out} = P_{in} - P_c, \tag{2.16}$$

which means that the efficiency of the slip coupler may be expressed as

$$\eta_{eff} = \frac{P_{out}}{P_{in}} = \left(1 - \frac{P_c}{P_{in}}\right). \tag{2.17}$$

The slip coupler efficiency and output power are, therefore, entirely characterised by calculating only the conductor losses.

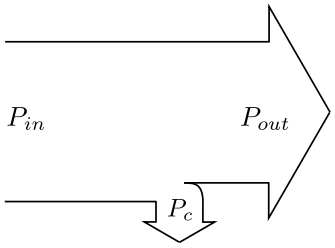

Figure 2.6: Power flow of the slip coupler, showing conductor losses as the main loss considered in the analysis.

2.4 Finite element method

Figure 2.7 shows the FE procedure as implemented in `Semfem`. The `Semfem` module is used in a `Python` script and the complete coded solution is given in Appendix E. In this section, the analytical method used to estimate the slip coupler inductances, currents, and torque is evaluated. The effect of the number of estimation iterations on the simulation time and accuracy are investigated. Finally, the air gap mesh is discussed.

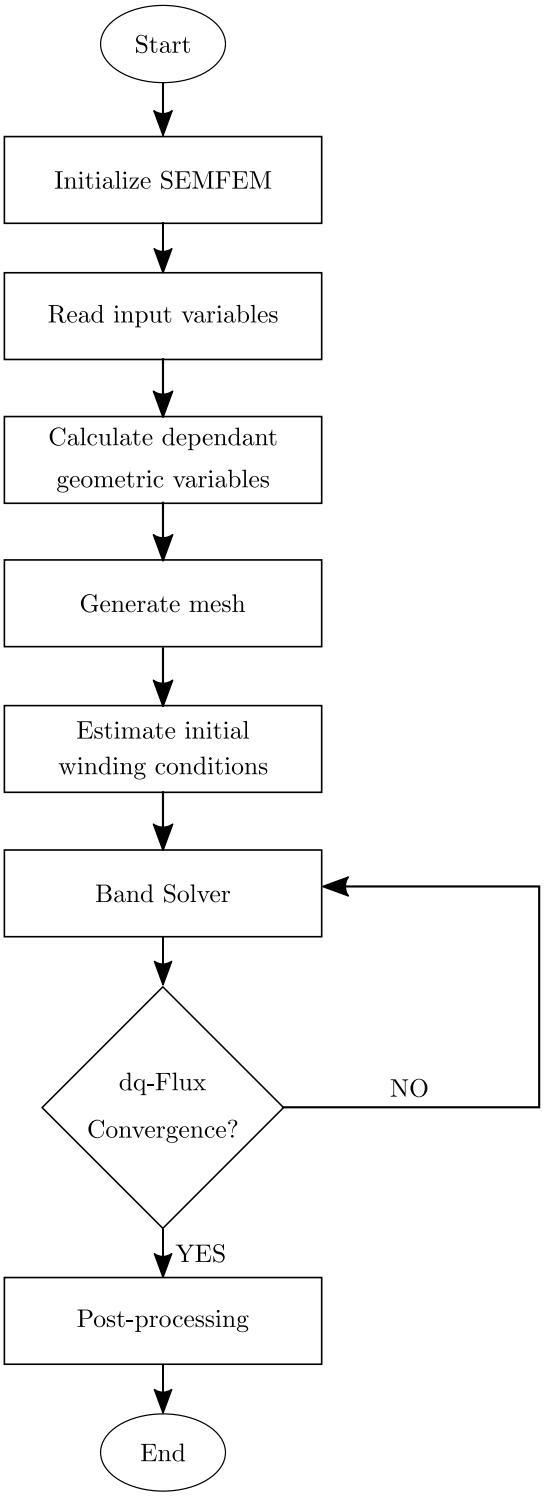

Figure 2.7: FEA procedure to estimate machine performance using `Semfem`.

2.4.1 Calculation of L_d and L_q using an iterative inductance method

The inductance calculation method, derived in [1], is used in this analysis. The procedure makes use of a positionally-stepped static FEM to solve the machine parameters. The estimation methods is a powerful, analytical approach which has been proven to produce

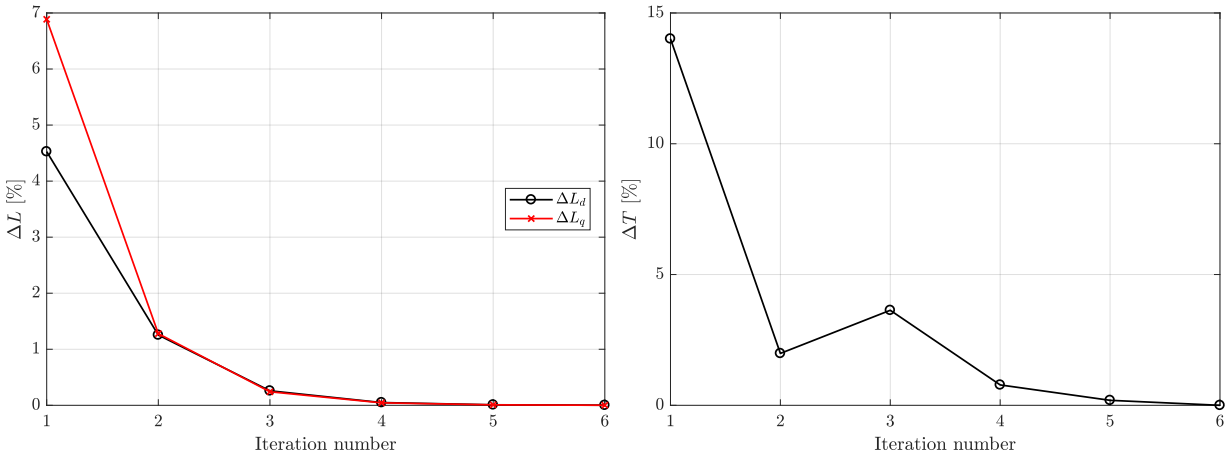

(a) (b)

Figure 2.8: Effect of number of algorithm iterations on solution accuracy as shown in (a) the ΔL_d and ΔL_q values per iteration and (b) the percentage change in torque.

accurate results. An implication of the assumption in Eq. (2.2) and (2.3), is that computation time can be shortened by only calculating a single three-phase set of currents, flux linkages and inductances. `Semfem` requires the currents in the rotor windings to be specified to correctly calculate the performance parameters of the slip coupler. However, the rotor winding currents are not known beforehand and initially need to be estimated. The inductance procedure iteratively estimates the static winding currents based on the values of the FE output. Initially, these currents are assumed to be acting along the quadrature axis only ($I_{d,0} = 0$). From Eq. (2.16), the initial current is specified as

$$I_{q,0} = \sqrt{\frac{2P_c}{\left(\frac{N_S}{3}\right) R_c}}. \tag{2.18}$$

The inductance method used in this analysis is described in Algorithm 2.4.1. The `Semfem` solution is two-dimensional in nature, and the end-winding inductance term, L_e should be included in the dq flux linkage calculation. The end-winding inductance for both slip couplers is calculated in Appendix B. Depending on the number of static rotor positions specified, the algorithm can converge to a solution within a couple of seconds. In this study, only the *Band* solver is considered when solving the FE airgap mesh, as shown in the Algorithm. However, *AGE* may also be used to obtain more accurate results, at the cost of computation time [19].

2.4.2 Effect of the number of iterations on solution accuracy

The number of iterations needed, as outlined in Algorithm 2.4.1, to sufficiently estimate an accurate solution is investigated. To accomplish this, the number of static rotor positions that the FE solver steps through are kept constant at 50 steps. The slip speed for both slip couplers is kept constant at 3 % slip. Figure 2.8 (a) shows the relative change in inductance

Algorithm 2.4.1 Inductance Estimation Algorithm

Initialise variables

$i \leftarrow 0; j \leftarrow 0; k \leftarrow 0; i_{d0} \leftarrow 0; m \leftarrow 0$
$n_i \leftarrow$ Number of iterations
$n_s \leftarrow$ Number of position steps
$i_{q0} \leftarrow$ Initial current ▷ Eq. (2.18)
$\theta_{PM} \leftarrow \frac{2\pi}{N_P}$ ▷ Pole pitch angle
$\theta_{Slot} \leftarrow \frac{2\pi}{N_S}$ ▷ Rotor slot angle
for $i \leftarrow 0, n_i$ **do**
  for $j \leftarrow 0, n_s$ **do**
    $k \leftarrow 0$
    $\theta_{rotor}(j) \leftarrow 3 \cdot i \cdot ({}^{\theta_{PM}}/_{n_s}) + \theta_{offset}$ ▷ Rotor position at step j
    for $m \leftarrow 0, {}^{N_S}/_3$ **do**
      if $k \pmod 2 == 0$ **then**
        $\theta_e \leftarrow [m \cdot \theta_{Slot} + \theta_{rotor}(j) - {}^{\pi}/_2] \cdot ({}^{N_P}/_2)$
      else
        $\theta_e \leftarrow [m \cdot \theta_{Slot} + \theta_{rotor}(j)] \cdot ({}^{N_P}/_2)$ ▷ Electrical angle
      end if
      $\boldsymbol{I}_{abc}(m) \leftarrow \boldsymbol{K}_P^{-1}(\theta_e)\boldsymbol{I}_{dq(m)}$ ▷ Park's transformation to `Semfem`
      $k \leftarrow k + 1$
    end for
  end for
  → Call `Semfem` Band Solver
  for $j \leftarrow 0, n_s$ **do**
    $\boldsymbol{\lambda}_{dq}(j) \leftarrow \boldsymbol{K}_P(\theta_e)\boldsymbol{\lambda}_{abc}(j)$ ▷ From `Semfem` solver
    $\boldsymbol{I}_{dq}(j) \leftarrow \boldsymbol{K}_P(\theta_e)\boldsymbol{I}_{abc}(j)$ ▷ From `Semfem` solver
  end for
  if i == 0 **then**
    $\boldsymbol{\lambda}_m = \boldsymbol{\lambda}_d$ ▷ PM flux contribution
    $\boldsymbol{L}_q \leftarrow {}^{\boldsymbol{\lambda_q}}/_{\boldsymbol{I}_q} + \boldsymbol{L}_e$
    $\boldsymbol{L}_d \leftarrow \boldsymbol{L}_q$
  else
    $\boldsymbol{L}_q \leftarrow {}^{\boldsymbol{\lambda_q}}/_{\boldsymbol{I}_q} + \boldsymbol{L}_e$
    $\boldsymbol{L}_d \leftarrow \dfrac{\boldsymbol{\lambda}_d - \boldsymbol{\lambda}_m}{\boldsymbol{I}_q} + \boldsymbol{L}_e$
  end if
  $\boldsymbol{I}_d \leftarrow f(L_{dq}, \lambda_{dq}, \lambda_m, \omega_{sle}, R_c)$ ▷ Eq. (2.9)
  $\boldsymbol{I}_d \leftarrow g(L_{dq}, \lambda_{dq}, \lambda_m, \omega_{sle}, R_c)$ ▷ Eq. (2.10)
  $\boldsymbol{I}_{dq}$ becomes new input current for next iteration
end for
End

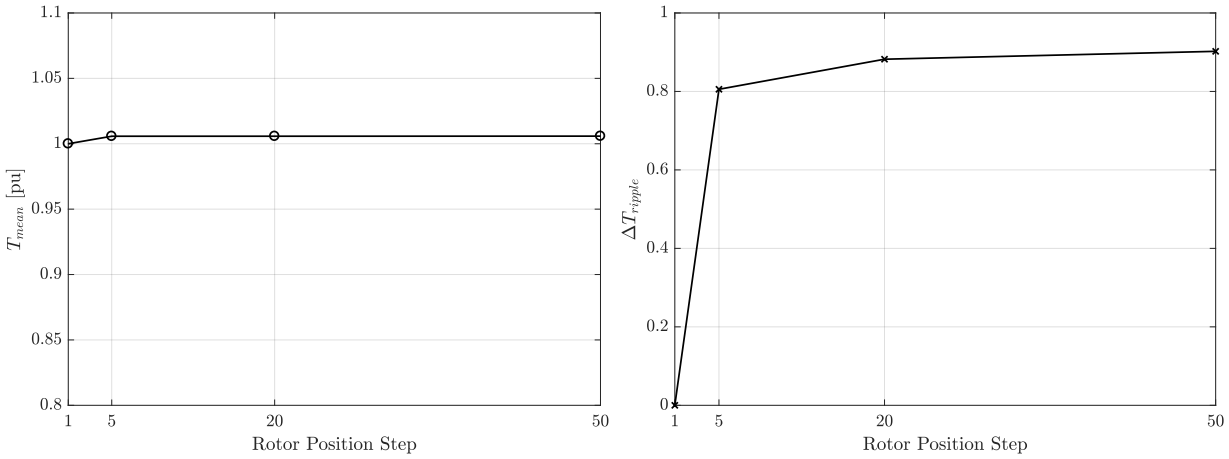

Figure 2.9: Effect of number of static rotor position evaluation steps on (a) the mean output torque and (b) the calculated torque ripple.

values after each algorithm iteration. Figure 2.8 (b) shows the calculated torque for a given number of iterations, which shows that at least four iterations are required to produce a sufficiently accurate solution. However, five iterations are preferred if accuracy is critical. For optimisation, four algorithm iterations are used to reduce the computation time.

2.4.3 Effect of the number of evaluated rotor positions on solution accuracy

In this investigation, only five iterations are considered when varying the number of static rotor steps. The slip speed for both couplers is kept constant at 3 %. The torque ripple value is determined for a different number of static rotor steps. The torque ripple is expressed as

$$\Delta T_{ripple} = \frac{T_{max} - T_{min}}{T_{avg}}, \tag{2.19}$$

where T_{max} and T_{min} is the maximum and minimum torque, respectively. Figure 2.9 (a) shows the mean torque output after a given number of rotor position evaluations. There is no significant variation in solution accuracy for a change in the number of steps when considering the calculated torque. Figure 2.9 (b) shows the ΔT_{ripple} value of the slip coupler for a given number of steps. Although a single step does not provide any insight into the ΔT_{ripple} value, it is assumed to always be $\Delta T_{ripple} < 3\%$. The validity of this assumption is evaluated in Chapter 4. Due to this assumption, and when considering the significant computation time reduction when only evaluating a single static step, only a single rotor position step is evaluated when optimising these designs in Chapter 3.

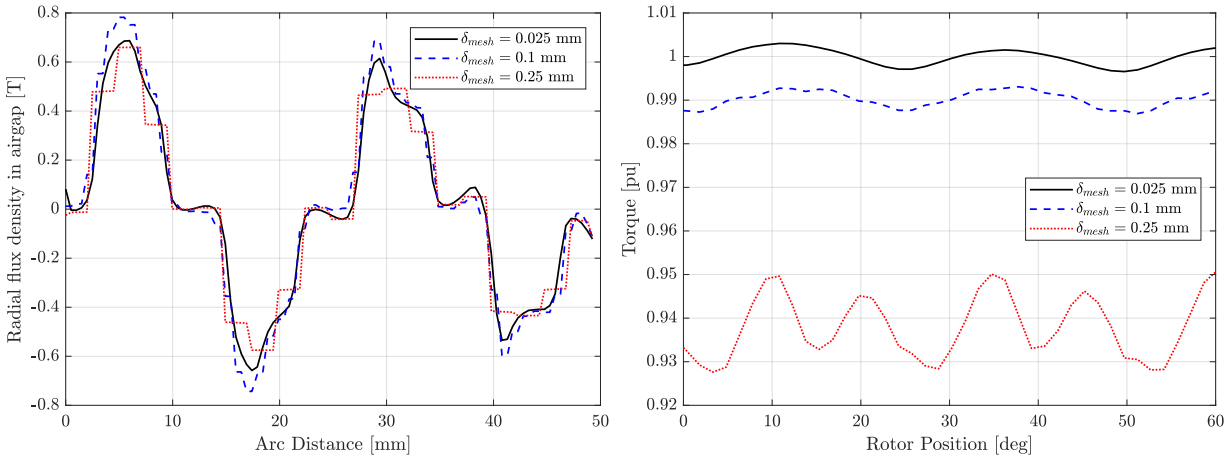

(a) (b)

Figure 2.10: Effect of mesh fineness on (a) the radial flux density waveform in the airgap and (b) the rated torque for different mesh parameters.

2.4.4 Influence of the FE airgap mesh on solution accuracy

`Semfem` can automatically generate an FE mesh using the Triangle algorithm [18]. Each line defined in `Semfem` requires the number of nodes along that line to be specified, which in turn determines how the mesh is generated. The smallest node-to-node distance, δ_{mesh} mm, is considered representative of the airgap mesh fineness. Figure 2.10 (a) shows the radial flux density in the air-gap for different values of δ_{mesh}. Figure 2.11 visually shows the effect of δ on the generated mesh. Although the crude mesh ($\delta_{mesh} = 0.25$ mm) approximates the *true* flux density waveform closely, Figure 2.10 (b) shows there is a significant difference in the calculated output torque for differently defined meshes. Generating a fine mesh takes significant computation time, and a trade-off between time and accuracy is inevitable. Therefore, for the optimisation, a value of $\delta_{mesh} = 0.075$ mm is selected.

2.5 Concluding remarks

In this chapter, the performance of the inductance estimation algorithm has been evaluated and implemented in the design of two slip couplers. This method, when implemented in `Python/Semfem`, is sufficient to quickly and accurately solve the slip coupler output parameters. Both slip couplers have a fundamental pole-to-slot ratio of 14:15 and high winding factor. The slip coupler performance parameters are calculated using the inductance estimation algorithm. The algorithm requires at least four iterations to produce a sufficiently accurate solution. It is assumed that the torque ripple is negligible for simulation purposes. Therefore, only a single static rotor position step is evaluated. A minimum node-to-node airgap mesh distance of $\delta_{mesh} = 0.075$ mm is chosen to produce the FE mesh. In conclusion, the FE software can be successfully implemented for optimisation in the subsequent chapter.

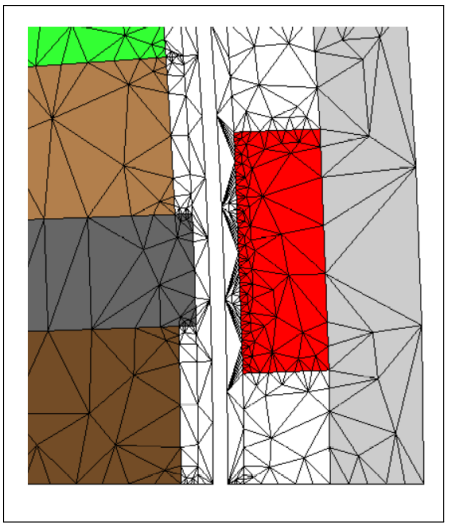

(a) Coarse airgap mesh, with δ = 0.25 mm

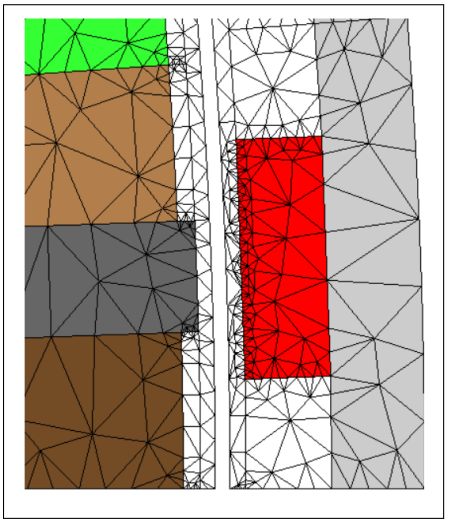

(b) Medium airgap mesh, with δ = 0.1 mm

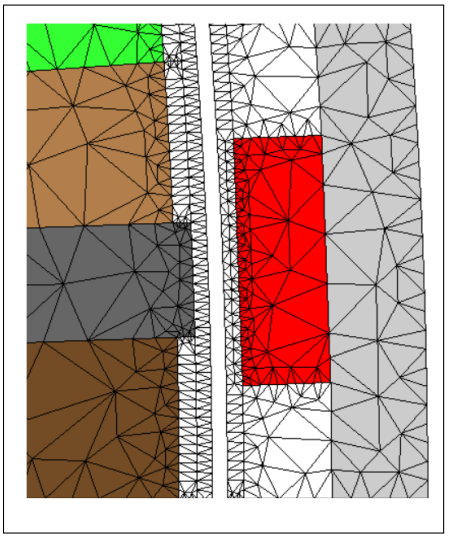

(c) Fine airgap mesh, with δ = 0.025 mm

Figure 2.11: Generated airgap mesh, showing the mesh parameter δ.

Chapter 3

Design Optimisation

In this chapter, the design optimisation of the slip coupler is investigated. Both the 28:30 and 84:90 slip couplers are optimised. The `Visualdoc` optimisation software, developed by Dr Vanderplaats [20], is capable of easily optimising the slip coupler designs. However, some insight into the underlying optimisation algorithms is required. The non-dominated sorting genetic algorithm (NSGA-II) and modified method of feasible direction (MMFD) algorithms are discussed and applied. The NSGA-II generated Pareto-fronts, optimisation constraint performance and input variable influence are discussed in detail.

3.1 Multi-objective optimisation procedures

The `Visualdoc` software [21] is used to optimise the slip coupler designs. Figure 3.1 shows how the `Semfem` script communicates with the optimisation procedure. The slip coupler is a multi-objective problem (MOP), requiring simultaneous minimisation of the active and PM mass. In general, let $\mathcal{S} \subseteq \mathbb{R}^{n_x}$ be within a n_x-dimensional search subset defined by a finite set of decision variables. Let $\boldsymbol{x} = (x_1, x_2, \ldots, x_{n_x}) \in \mathcal{S}$ refer to a decision vector within the search space subset. The objective vector function is defined such that

$$f(x) = \{f_1(\boldsymbol{x}), f_2(\boldsymbol{x}), \ldots, f_{n_O}(\boldsymbol{x})\} \in \mathcal{O} \subseteq \mathbb{R}^{n_O}, \tag{3.1}$$

where

$\mathbb{R}^{n_O}$ = Objective space,
n_0 = Number of objective function evaluations,
$\mathcal{O}$ = Objective subset.

Let $\mathcal{F} \subseteq \mathcal{S}$ be the feasible subset, constrained by n_g-inequality and n_h-equality constraints, such that

$$\mathcal{F} = \{x : g_m(\boldsymbol{x}) \leq 0, h_l(\boldsymbol{x}) = 0, m = 1, \ldots, n_g; l = 1, \ldots, n_h\}, \tag{3.2}$$

where g_m and h_l are the inequality and equality constraints, respectively. With the above definitions, the general expression for a MOO problem

$$\text{minimise} \qquad f(\boldsymbol{x}),$$

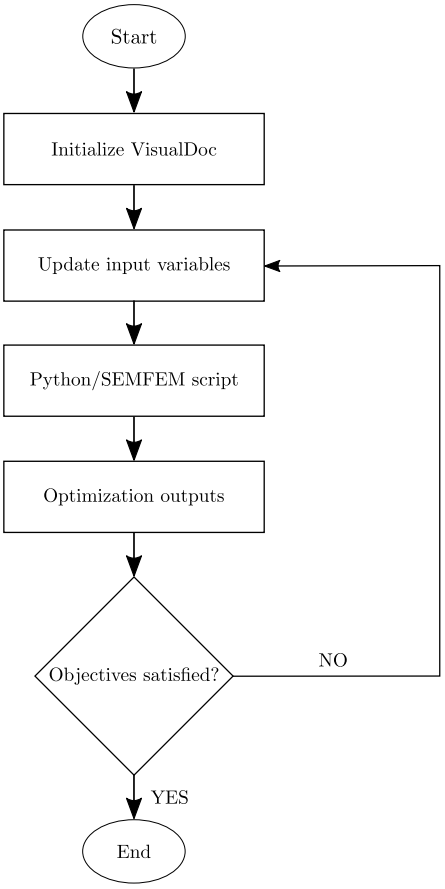

Figure 3.1: General optimisation procedure using `Visualdoc` linked with `Python/Semfem` script.

$$\begin{aligned} \text{subject to} \qquad & \boldsymbol{x} \in \mathcal{F}, \\ & \boldsymbol{x} \in [x_{min}, x_{max}]^{n_x}. \end{aligned} \tag{3.3}$$

For any solution, $\boldsymbol{x}^*$, to be viable, it has to be in the feasible solution subset $\mathcal{F} \subseteq \mathcal{S}$. The solution also has to remain within the equality and inequality constraints. Usually, the improvement of one objective causes the deterioration of the other.

The optimisation algorithm needs to be capable of searching an adequately large feasible space $\mathcal{F} \subseteq \mathcal{S}$, to avoid generating solutions which, although viable, do not represent true optimal solutions. In other words, an algorithm which does not search wide enough is in danger of generating local, and not global objective minima. Minimising the slip coupler active mass is the first objective, where the active mass is

$$f_1(m_A) = m_c + m_R + m_S, \tag{3.4}$$

where

m_C = Total conductor mass,
m_R = Rotor mass,
m_S = Stator mass.

Minimising the PM mass is the second objective, where the PM mass is the sum of all the PMs, such that

$$f_2(m_{PM}) = \sum_{j=1}^{N_P} m_{PM(j)}, \tag{3.5}$$

where $m_{PM,j}$ is the j^{th} PM and N_P is total number of poles of the slip coupler. The optimisation objectives and constraints are summarised in Table 3.1. Also, the NdFe35 magnetic material is used in both slip couplers. The material has a magnetic coercivity of $H_c = -890$ kA $\cdot$ m^{-1} and a relative permeability value of $\mu_r = 1.09978$ at 22 °C.

3.2 NSGA-II algorithm

The non-dominated sorting genetic algorithm (NSGA-II) is discussed in this section. The reader is referred to [22, 23] for an in-depth discussion on the NSGA-II algorithm procedures and applications. Some of the major concepts of the NSGA-II algorithm includes dominance, the Pareto-optimal front, mutation- and crossover probabilities, and solution population. These definitions are presented here.

Definition 3.2.1. Domination: Given two decision vectors $\boldsymbol{x}$ and $\boldsymbol{z}$, $\boldsymbol{x}$ dominates $\boldsymbol{z}$, noted as $\boldsymbol{x} \prec \boldsymbol{z}$, if and only if $\boldsymbol{x}$ is equally good or better than $\boldsymbol{z}$ for each of the objectives to optimise.

Figure 3.2 (a) shows the concept of dominance in a given feasible space.

Definition 3.2.2. Weak domination: A decision vector, $\boldsymbol{x}$, weakly dominates a decision vector, $\boldsymbol{z}$, noted as $\boldsymbol{x} \preceq \boldsymbol{z}$, if and only if $\boldsymbol{x}$ is not worse than $\boldsymbol{z}$ for each of the objectives to optimise.

Table 3.1: Optimisation constraints and objectives

		Slip Coupler	
Optimisation parameter		**28:30**	**84:90**
Constraints	Rated Torque T_{rated} [N $\cdot$ m]	$34 \leq T \leq 36$	$132 \leq T \leq 134$
	Torque Ripple ΔT	$\leq 3\%$	
	Slip frequency f_{sl} [Hz]	≤ 5	
	Rated slip s_{rated}, [pu]	0.03	
	Current Density J_r, [A $\cdot$ mm^{-2}]	≤ 4	
Objectives	$f_1(m_A)$ [kg]	Minimize	
	$f_2(m_{PM})$ [kg]	Minimize	

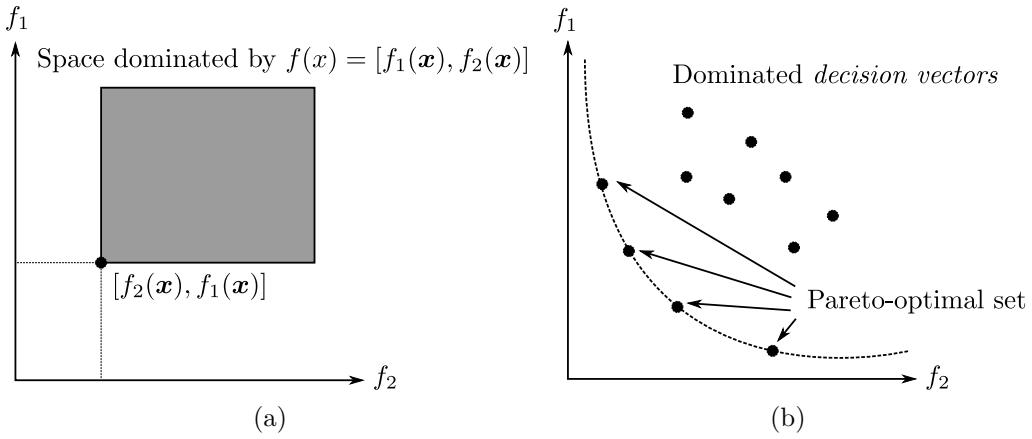

Figure 3.2: NSGA-II definitions of (a) the dominance of $f(x)$ in the feasible solution subset $\mathcal{F} \subseteq \mathcal{S}$ and (b) the Pareto-optimal set of decision vectors.

Definition 3.2.3. Pareto-optimal: A decision vector, $\boldsymbol{x}^* \in \mathcal{F}$, is termed a Pareto-optimal solution if there does not exist a decision vector $\boldsymbol{x}$ that dominates $\boldsymbol{x}^*$.

Definition 3.2.4. Pareto-optimal set: The set of all Pareto-optimal decision vectors that form the Pareto-optimal set, $\mathcal{P}^*$, which can be expressed as

$$\mathcal{P}^* = \{\boldsymbol{x}^* \in \mathcal{F} | \nexists \boldsymbol{x} \in \mathcal{F} : \boldsymbol{x} \prec \boldsymbol{x}^*\} \tag{3.6}$$

Definition 3.2.3 in words says that should a decision vector $\boldsymbol{x}^*$ be found, which is not dominated by any other decision vector $\boldsymbol{x}$, then this solution is said to be Pareto-optimal. Figure 3.2 (b) shows the Pareto-optimal set of solutions.

3.2.1 Parameter selection and general considerations

The general NSGA-II procedure is shown in Figure 3.3. The NSGA-II is an elitist algorithm, meaning that a part of the *parent* generation is used unaltered in the next generation of solutions. This method has significant computational advantages to non-elitist algorithms because the solver does not have to re-search certain areas of the feasible space. An initial population is randomly generated based on the constraints presented. The first iteration evaluates and ranks each decision vector $\boldsymbol{x}$ based on the objective function $f(\boldsymbol{x})$. These solutions undergo selection, crossover and mutation.

The probability of crossover, P_{cr}, is a user selected parameter that represents the likelihood of a solution being passed on to the next generation. In general, a likelihood of $0.5 \leq P_{cr} \leq 0.9$ is typical for the NSGA-II algorithm.

The probability of mutation, P_{mu}, is a function of the number of decision (independent) variables of the optimisation. In general $P_{mu} = {}^1/_{n_x}$, which would mean that a

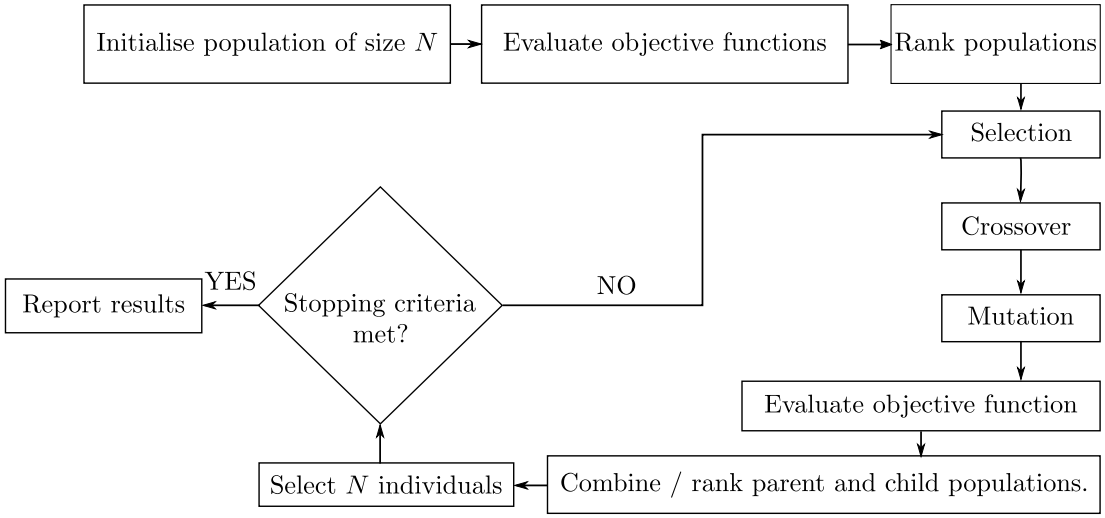

Figure 3.3: General NSGA-II procedure.

problem with 10 input parameters would have probability of mutation value of $P_{mu} = 0.1$. The computation time for a given MOP can be approximated by

$$f(t) = t_{sol} \cdot N \cdot n_i, \tag{3.7}$$

where

t_{sol} = Computation time for single solution,
N = Population size,
n_i = Number of optimisation algorithm iterations.

MOPs, therefore, can take a significant amount of time to complete. A trade-off exists for the designer and care should be taken in setting up an optimisation correctly.

3.3 MMFD algorithm

The modified method of feasible direction (MMFD) optimisation algorithm is a gradient-based optimisation technique. The `Visualdoc` software allows the user to optimise complex problems without needing insight into the underlying optimisation techniques used, or its architecture. Nonetheless, gradient-based optimisation is briefly discussed in this section, which is based on gradient-optimisation fundamentals in [24, 25].

3.3.1 General algorithm for smooth functions

As an introduction, the objective function in Eq. (3.3) is considered non-linear, but a sufficiently smooth function of $\boldsymbol{x}$. Gradient-based optimisation techniques use the derivatives of the objective function $f(\boldsymbol{x})$ to determine the most promising directions along which the algorithm should search. All unconstrained gradient-based optimisation

algorithms follow the same form as shown in Algorithm 3.3.1. Gradient-based algorithms search for more optimal points along a line in n-dimensional space. As shown in the main loop in the algorithm, the design variable $\boldsymbol{x}$ is updated at each iteration k, such that

$$\boldsymbol{x}_{k+1} = \boldsymbol{x}_k + \Delta\boldsymbol{x}_k, \tag{3.8}$$

where

$\alpha_k \boldsymbol{p}_k = \Delta\boldsymbol{x}_k$,
$\boldsymbol{p}_k$ = The search direction for major iteration k,
α_k = The accepted step length from the line search.

It is here that the gradient-based algorithms are classified: based on the method of calculating search direction $\boldsymbol{p}_k$ and step length α_k. In general, the gradient of a function $f(\boldsymbol{x})$ is expressed by a vector of partial derivatives for each independent (decision) variable which is expressed as

$$\nabla f(\boldsymbol{x}) \equiv g(\boldsymbol{x}) \equiv \begin{bmatrix} \frac{\partial f}{\partial x_1} \\ \frac{\partial f}{\partial x_2} \\ \cdots \\ \frac{\partial f}{\partial x_n} \end{bmatrix}, \tag{3.9}$$

The gradient of a function of n variables is an n-vector. Next, the conditions of optimality are discussed.

Algorithm 3.3.1 Algorithm for smooth functions

1: **Input:** Initial guess, $\boldsymbol{x}_0$
2: **Output:** Optimum, $\boldsymbol{x}^*$
3: $k \leftarrow 0$
4: **while** != converged **do**
5: Calculate new search direction $\boldsymbol{p}_k$
6: Find step length $\alpha_k \rightarrow f(\boldsymbol{x}_k + \alpha_k \boldsymbol{p}_k) < f(\boldsymbol{x}_k)$
7: $\boldsymbol{x}_{k+1} \leftarrow \boldsymbol{x}_k + \alpha_k \boldsymbol{p}_k$
8: $k \leftarrow k + 1$
9: **end while**

3.3.2 Optimality

The optimality conditions can be derived from the Taylor-series expansion of f about $\boldsymbol{x}^*$, expressed as,

$$f(\boldsymbol{x}^* + \epsilon\boldsymbol{p}) = f(\boldsymbol{x}^*) + \epsilon\boldsymbol{p}^T g(\boldsymbol{x}^*) + \tfrac{1}{2}\epsilon^2 \boldsymbol{p}^T H(\boldsymbol{x}^* + \epsilon\theta\boldsymbol{p})\boldsymbol{p}, \tag{3.10}$$

where

H = Hessian matrix,
ϵ = Scalar value,

and $\theta \in (0, 1)$. From Eq. (3.10) the definition of optimality for a gradient-based optimisation algorithm, in general, is discussed.

Definition 3.3.1. Optimality: For $\boldsymbol{x}^*$ to be considered a local minimum, then for any vector $\boldsymbol{p}$ there needs to be a finite ϵ such that,

$$f(\boldsymbol{x}^* + \epsilon \boldsymbol{p}) \leq f(\boldsymbol{x}^*), \tag{3.11}$$

meaning there is a region in the feasible space where Eq. (3.11) is true. Should this be true, then

$$f(\boldsymbol{x}^* + \epsilon \boldsymbol{p}) - f(\boldsymbol{x}^*) \geq 0, \tag{3.12}$$

and the first and second order terms of in Eq. (3.10) must be greater than or equal to zero.

Simply, when the definition of the vector gradient in Eq. (3.9) is considered, the necessary conditions for a solution $\boldsymbol{x}^*$ to be considered a local minimum are

$$||g(\boldsymbol{x}^*)|| = 0, \tag{3.13}$$

and $H(\boldsymbol{x}^*)$, the Hessian matrix of the proposed solution vector, is either a positive semi-definite or positive definite.

Practically, the algorithm requires each decision vector to be a normalised value such that $x_n \in (0, 1) \in \mathcal{F}$. The gradient calculation will not produce any reliable result otherwise. The starting values $\boldsymbol{x}_0$ need to be varied if this algorithm is used in isolation, as the locally minimised objective function may not be close to the global minimum. The major advantage of this method, however, is that it is quick and well suited to multi-variable optimisation problems.

3.4 Optimised designs

In this section, the optimised results of the slip coupler designs are presented. Figure 3.4 shows the cross-sectional view of the slip coupler, indicating the design variables used in optimisation. The optimised 28:30 slip coupler design is compared to the top-bottom winding topology presented in [1]. The 84:90 slip coupler does not have such a comparison.

3.4.1 Optimised 28:30 slip coupler

The 28:30 slip coupler optimisation results is shown in Table 3.2. A total of 20 MMFD optimisation procedures were completed, each taking about 50 minutes. The NSGA-II

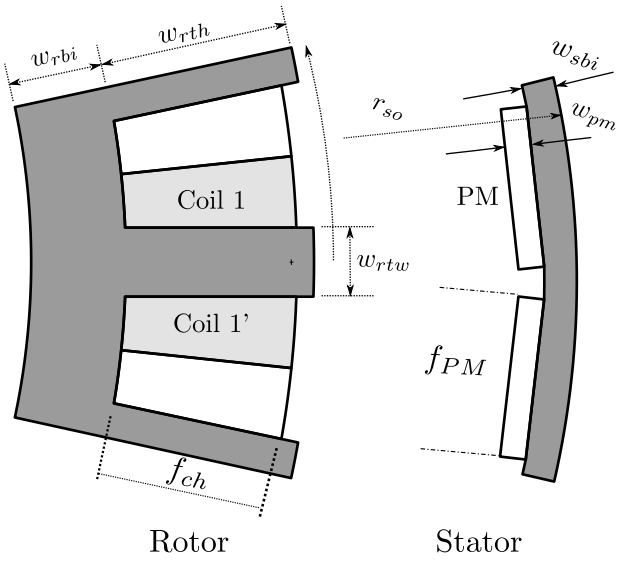

Optimisation parameters
w_{rbi} = Rotor back iron width
w_{rth} = Rotor slot height
w_{rtw} = Rotor slot width
f_{ch} = Coil height (as fraction of slot height)
r_{so} = Stator outer radius
w_{sbi} = Stator back iron width
f_{PM} = Magnet width (as fraction of magnet pitch)
w_{PM} = Magnet height

Figure 3.4: Cross-sectional view of the slip coupler.

implemented optimisation uses a probability of crossover value of $P_{cr} = 0.9$, a probability of mutation value of $P_{mu} = 0.111$, population size of $N = 70$, and 60 iterations are specified. The MMFD and NSGA-II optimisation solutions compare well with one another because of the way the search space of the MMFD has been constrained. Therefore, although the MMFD solution presented here serves as a confirmation of the NSGA-II result, the reader should not make the mistake of thinking that the MMFD would have found the same solution with wider geometric constraints. The input parameters were restricted, such that:

$$\begin{aligned} \mathcal{F}_{MMFD} = \quad & \{83 \leq r_{so} \leq 90, \\ & 79 \leq \delta_{pm} \leq 85, \\ & 45 \leq SL \leq 60, \ldots\}. \end{aligned} \tag{3.14}$$

The side-by-side winding topology design is compared with the top-bottom winding topology in [1]. The active mass has been reduced from 7 kg to 3.64 kg. The PM mass has been reduced from 0.88 kg to 0.57 kg. This improvement is considered a significant reduction in mass.

3.4.2 Optimised 84:90 slip coupler

The 84:90 slip coupler optimisation results is shown in Table 3.3. A number of NSGA-II optimisation procedures were necessary because the algorithms tend to violate certain constraints, which is only noticeable after the optimisation is complete. The NSGA-II optimisation used a probability of crossover value of $P_{cr} = 0.6$, a probability of mutation value of $P_{mu} = 0.111$, population size of $N = 150$ and 90 iterations. If a higher crossover probability is used, such that $P_{cr} > 0.6$, then the likelihood of generating, and passing

along solutions which have violated the optimisation constraints increase. When $P_{cr} = 0$, the genetic algorithm is considered as a non-elitist optimisation, which is computationally too expensive. When using Eq. (3.7), a single solution takes roughly 18 seconds, which means a total computation times of around 70 hours. The MMFD was again constrained around the NSGA-II algorithm optimal Pareto-front, such that

$$\begin{aligned} \mathcal{F}_{MMFD} = \quad & \{165 \leq r_{so} \leq 175, \\ & 38.5 \leq \delta_{pm} \leq 43.0, \\ & 65 \leq SL \leq 75, \ldots\} \end{aligned} \tag{3.15}$$

The final active mass is 12.197 kg, with a PM mass of 0.832 kg.

3.5 Pareto front generation

In this section, the Pareto-optimal set generated by the NSGA-II algorithm is discussed. The dominated solutions are shown alongside the Pareto-optimal front for both slip

Table 3.2: Design optimisation of the 28:30 slip coupler. The MMFD and NSGA-II optimisation outputs are compared, as well as presenting the top-bottom winding topology design of [1].

Design Variable	**NSGA-II**	**MMFD**	**Side-by-side design**
r_{so} [mm]	86.73	86.21	105
w_{sbi} [mm]	2.99	3.00	5.0
SL [mm]	54.74	55.34	65
δ_{pm} [%]	81.30	81.23	87
w_{pm}[mm]	3.27	3.28	4.0
w_{ag} [mm]	1.2	1.2	1.5
δ_{ch} [%]	0.88	0.88	-
w_{rtw} [mm]	4.86	4.87	6.4
w_{rth} [mm]	17.03	16.81	17.3
w_{rbi} [mm]	2.43	2.43	8.0
Constraints			
T_{rated} [Nm]	34.55	34.38	34.9
ΔT [%]	1.40	1.56	1.4
J_r [A $\cdot$ mm^{-2}]	3.71	3.73	2.72
Objective			
Active Mass [kg]	3.645	3.648	7
PM Mass [kg]	0.568	0.572	0.880

Table 3.3: Design optimisation of the 84:90 slip coupler, comparing MMFD and NSGA-II output.

Design Variable	NSGA-II	MMFD
r_{so} [mm]	172.64	172.41
w_{sbi} [mm]	5.00	4.89
SL [mm]	74.58	72.15
δ_{pm} [%]	40.11	40.73
w_{pm}[mm]	3.55	3.54
w_{ag} [mm]	1.2	1.2
δ_{ch} [%]	0.885	0.891
w_{rtw} [mm]	3.50	3.54
w_{rth} [mm]	18.389	19.301
w_{rbi} [mm]	3.04	3.14
Constraints		
T_{rated} [N · m]	135.23	134.85
ΔT [%]	1.23	0.716
J_r [A · mm^{-2}	3.787	3.648
Objective		
Active Mass [kg]	12.197	12.031
PM Mass [kg]	0.832	0.716

couplers. The Pareto-optimal fronts represented here are not necessarily the absolute optimum. Generating such a front requires careful algorithm parameter tuning. Adjusting P_{cr}, P_{mu}, and N to their ideal values is not a trivial matter and can significantly affect the optimisation outcome. It is deemed outside the scope of this thesis to find the true Pareto-optimal front for each slip coupler.

3.5.1 Optimised 28:30 slip coupler

Figure 3.5 shows the Pareto-optimal solution set. The dominated solutions are shown as black circles, whereas the Pareto-optimal set is shown as red triangles. The selected solution A is known as the upper extreme and solution C the lower extreme. The upper extreme represents solutions with higher active mass, and the lower extreme are solutions with higher PM mass. Solution B is in the middle of these. Figure 3.6 illustrates the geometric differences between these three slip coupler designs. The distinct space between the upper and lower solutions groups are not uncommon with GA optimisations. The possible reasons for this phenomena are briefly discussed.

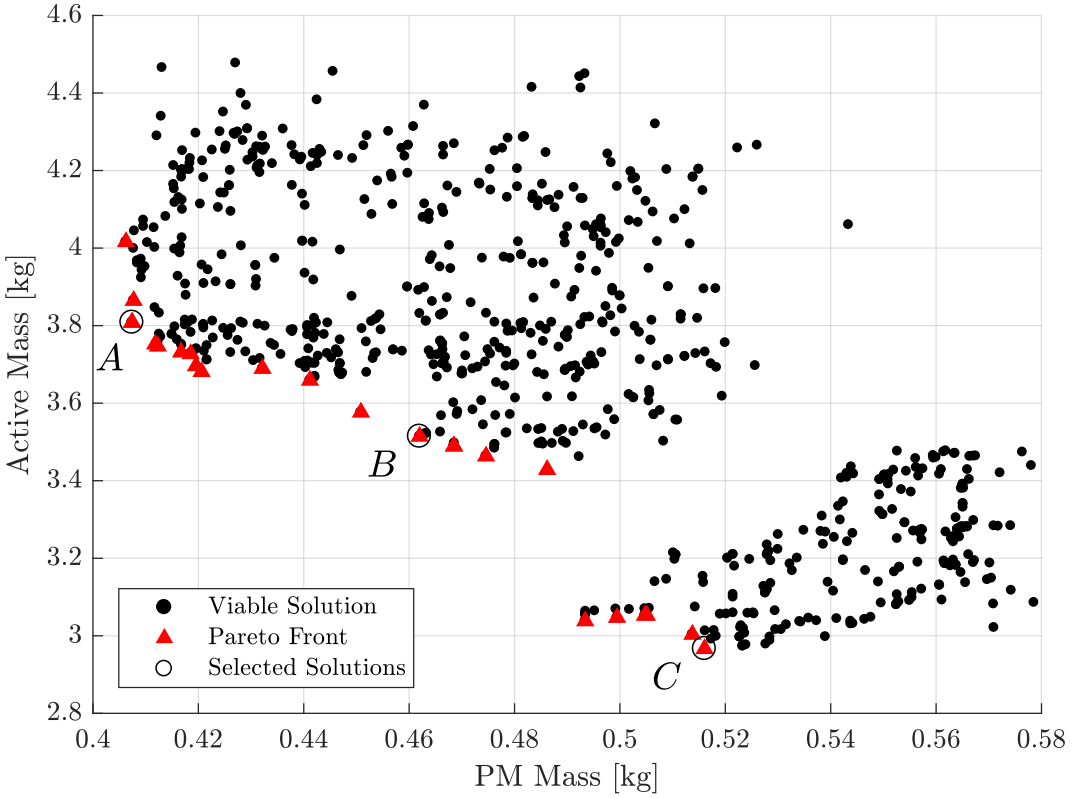

Figure 3.5: Feasible solution subset $\mathcal{F}$ created by the NSGA-II algorithm for the 28:30 slip coupler, showing Pareto-front solutions.

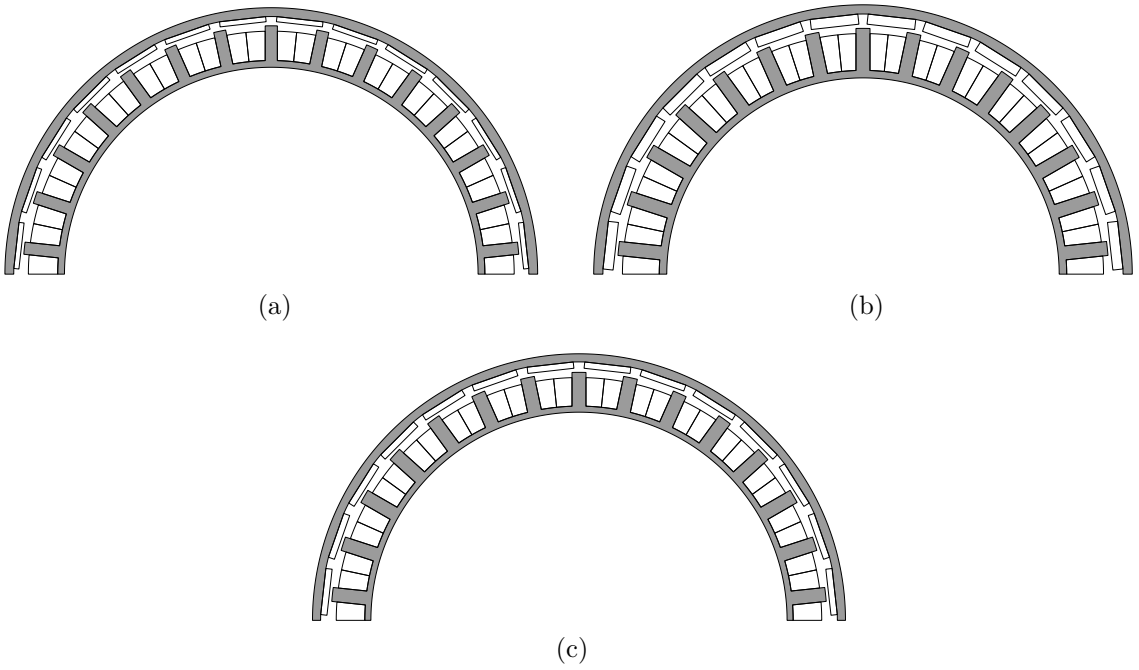

Figure 3.6: Selected designs from the 28:30 slip coupler Pareto-front, showing (a) the upper extreme A, (b) the center selected design B and (c) the lower extreme design C.

Initial population N, the distribution index of mutation and crossover (which affects the crowding distance between solutions) will affect the search space $\mathcal{S}$ area *covered* by the algorithm. It is mentioned that a population of $N = 70$ is chosen, where $N = 150$ is usually recommended. Population size is strongly related to the convergence quality of GAs and the duration of their run [26]. Smaller population sizes are not necessarily inadequate in producing an acceptable solution space, but it is entirely possible that the optimisation produces only a small portion of the total Pareto-optimal set. Therefore, it is in the opinion of the author that smaller population sizes may in some cases produce a discontinuous Pareto-optimal set, such that two separately dominated solution vectors are produced, as shown in the figure.

Continuing on parameter selection, different values of P_{mu} and P_{cr} will highlight different non-dominated solutions $\boldsymbol{x}^*$ on the Pareto-optimal front. For more information, the reader is directed to the research paper presented in [27], in which the effect of initial optimisation parameters is investigated.

3.5.2 Optimised 84:90 slip coupler

Figure 3.7 shows the Pareto-optimal solution space. The dominated solutions are shown as black circles, whereas the Pareto-optimal set is shown as red triangles. The solutions A, B and C are shown as selected solutions on the figure. Figure 3.8 illustrates the geometric differences between these three slip coupler designs. These solutions are nearly identical, but stator back iron width and stack length are the biggest contributors to active mass. The stator outer radius values for each of these solutions are nearly identical. There is a near 2.5 kg difference in active mass between pareto-optimal solution A and C. There is more than 0.2 kg difference in PM mass between solution A and C. The Pareto-optimal front is discontinuous, but there are dominated solutions between these Pareto-optimal sets, unlike the 28:30 slip coupler.

3.6 Constraint evaluations

The feasible subset $\mathcal{F}$ for both slip coupler designs is a function of the equality and inequality constraints imposed on the search space $\mathcal{S}$. Two of these constraints, namely current density and specific torque, which is a more indirect measurement of slip coupler performance, is evaluated in this section. Specific torque, ρ_τ, is measured in $\mathrm{N \cdot m \cdot kg^{-1}}$. The reader is reminded that the current density for both designs is limited to $J_c \leq 4\ \mathrm{A \cdot mm^{-2}}$. The torque constraints for each design is summarised in Table 3.1. Each solution $\boldsymbol{x}$ on the active- vs PM mass graph is colourised by firstly defining a normalised scale which indicates

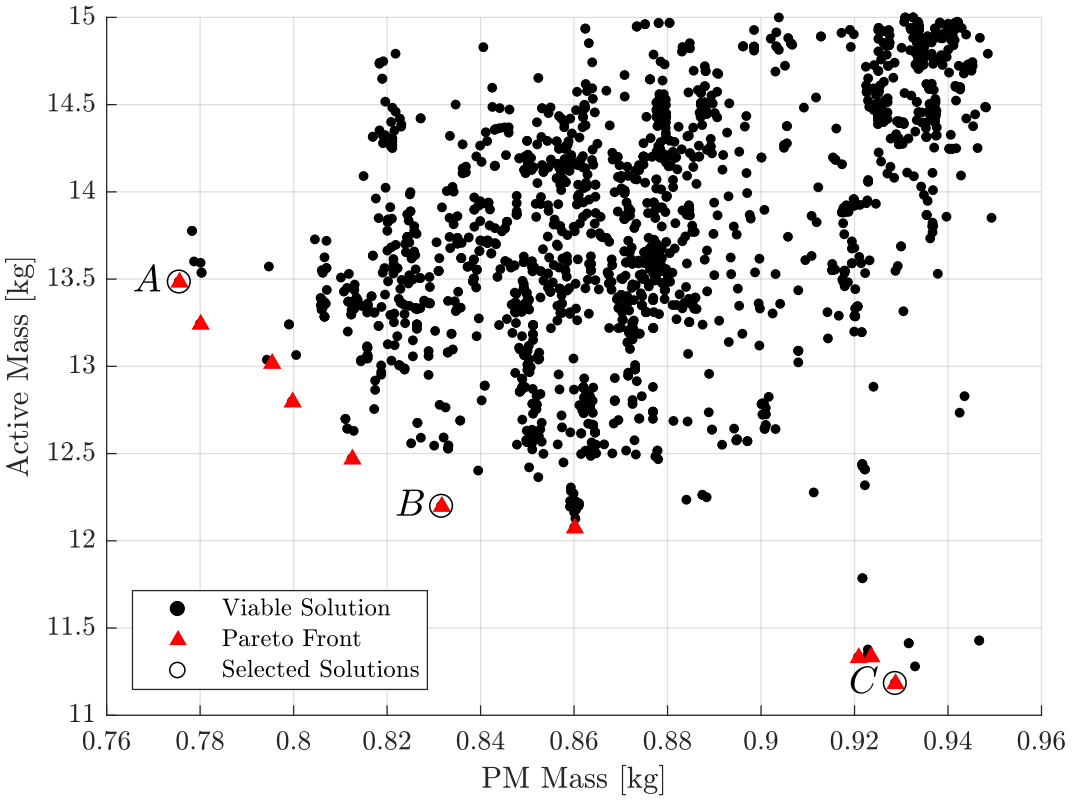

Figure 3.7: Feasible space $\mathcal{F}$ created by the NSGA-II algorithm for the 84:90 slip coupler, showing Pareto-front solutions.

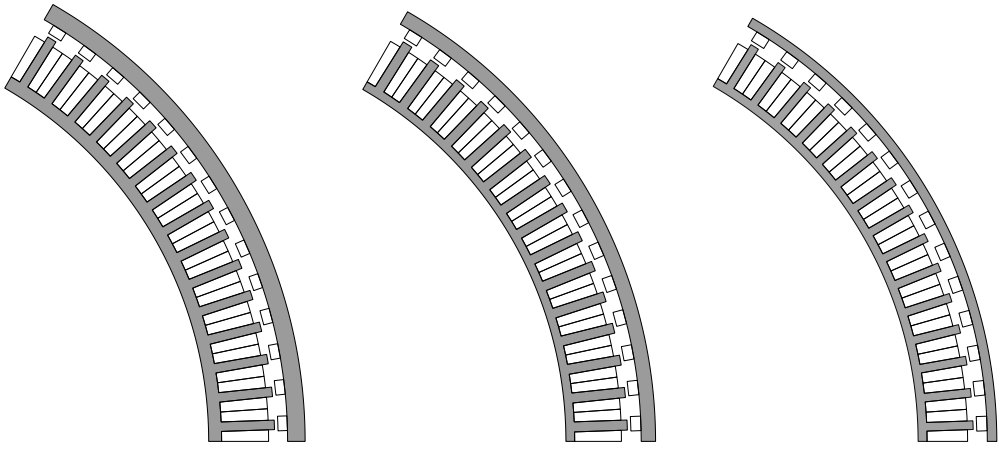

Figure 3.8: Selected 84:90 designs shown on the Pareto-front, with (a) the upper extreme A, (b) the center selected design B, and (c) the lower extreme design C.

the variable value magnitude relative to the minimum and maximum, such that

$$x_{n,norm} = \frac{x_{n,i} - x_{n,min}}{x_{n,max} - x_{n,min}} \cdot x_{n,i}, \tag{3.16}$$

where

$x_{n,i}$ = The i^{th} constraint/variable n,
$x_{n,min}$ = Minimum variable value in given feasible space,
$x_{n,max}$ = Maximum variable value in given feasible space.

The color gradient is then based on the normalised value of the constraint or variable. A similar approach is used in [28].

3.6.1 Evaluation of the 28:30 slip coupler

Figure 3.9 shows the current and specific torque of the 28:30 slip coupler. Before discussing each individual graph, it is clear that two solution *regions* have formed, as is evident by the colourised gradient applied over the feasible solution space. There are clear high- current density and specific torque regions, as well as lower density regions. These regions are distinctly separated from one another. The higher density regions have higher PM mass m_{PM}, ranging from $0.5 \leq m_{PM} \leq 0.58$ kg. This high density region also has a lower active mass, m_A, ranging from $3 \leq m_A \leq 3.5$ kg. From Figure 3.9 (a), the current density for the dominated and non-dominated solutions are such that $3.413 \leq J_c \leq 3.998$ A $\cdot$ mm^{-2}. There is therefore a 0.586 A $\cdot$ mm^{-2} variation across the presented solution space, which is comparatively low. A current density of 3.998 A $\cdot$ mm^{-2} is very close to the 4 A $\cdot$ mm^{-2} limit. It is concluded that there is little variation in either the winding cross-sectional area or winding current, due to this low variation in current density.

From Figure 3.9 (b), the specific torque ranges from $6.971 \leq \rho_\tau \leq 10.081$ N $\cdot$ m $\cdot$ kg^{-1}. There is a variation of 3.111 N $\cdot$ m $\cdot$ kg^{-1} across the presented solution space, which is comparatively high. Higher torque densities are found where the PM mass is increased, because increasing the PM has the effect of decreasing the active mass. The lowest torque densities are present in the $4 \leq m_A \leq 4.5$ kg region. It is concluded that the specific torque of this slip coupler can be increased without a significant increase in current density.

3.6.2 Evaluation of the 84:90 slip coupler

Figure 3.10 shows the current density and specific torque of the 84:90 slip coupler. The general feasible solution space indicated on the graphs does not resemble the 28:30 slip coupler space in Figure 3.9.The current density in Figure 3.10 (a) ranges between $3.629 \leq J_c \leq 3.999$ A $\cdot$ mm^{-2}, which means a variation of 0.371 A $\cdot$ mm^{-2}. The optimisation algorithm has found feasible solutions closer to the upper limit of the current density

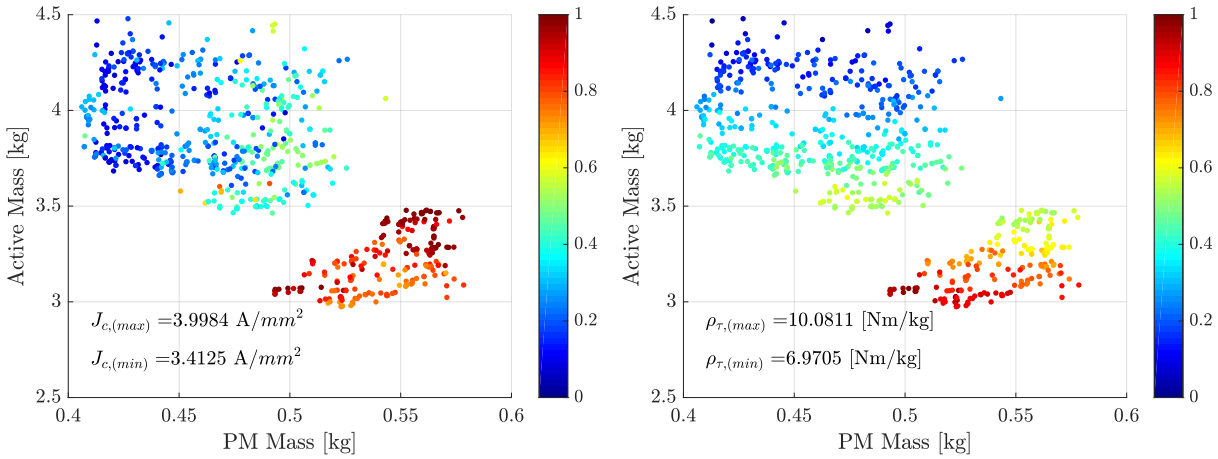

(a) Current density J_c (b) Specific torque ρ_T

Figure 3.9: Constraint evaluation of the 28:30 slip coupler.

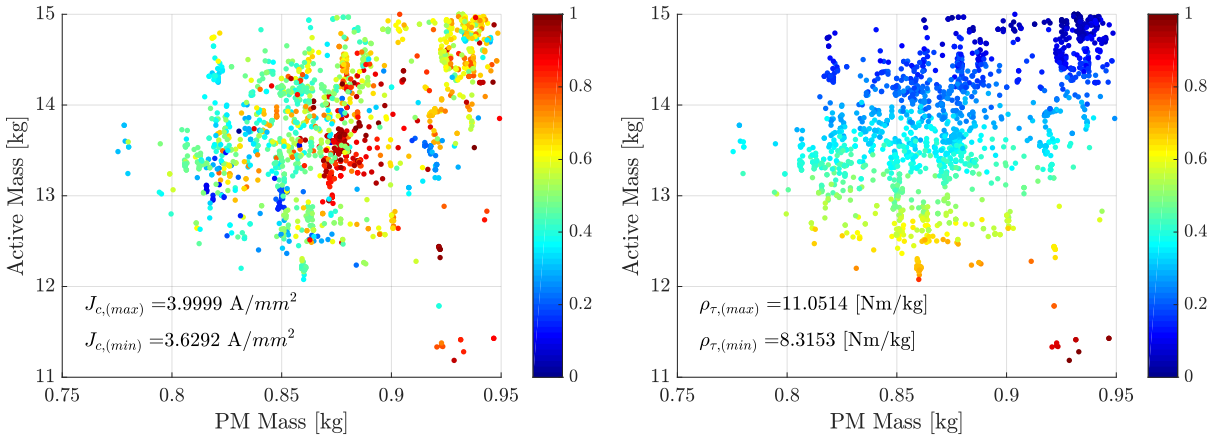

(a) Current Density J_c (b) Specific torque ρ_T

Figure 3.10: Constraint evaluation of the 84:90 slip coupler.

constraint. There is a group of very high current density solutions near the middle of the figure. All the non-dominated solutions are on the lower end of the current density scale. As with the 28:30 slip coupler, the consistent current density throughout the feasible solution space indicates that neither the coil area or winding current varies significantly.

The specific torque in Figure 3.10 (a) varies between $8.315 \leq \rho_\tau \leq 11.051$ N $\cdot$ m $\cdot$ kg^{-1}. The highest specific torque is present at the lower active mass regions and very steadily decreases to the higher active mass areas; which may indicate that the developed torque for all these solutions is consistent. Therefore, if a higher specific torque is desired, then the PM mass should be increased. There is no clear correlation between current density and specific torque for the 84:90 slip coupler. In conclusion, the optimisation algorithm has struggled to keep the 84:90 slip coupler within the current density limit and may indicate

that it is not as well suited to the drivetrain power rating as is the case with the 28:30 slip coupler.

3.7 Input parameter population trends

This section discusses the influence of the independent variables on the generated feasible solution space for both slip couplers. Each solution $\boldsymbol{x}$ shown on the active- vs PM mass graphs are colourised according to a normalised input value scale as shown in Eq. (3.16).

3.7.1 The 28:30 slip coupler evaluation

Each independent variable has an effect on the generated solution distribution in the feasible space. Figure 3.11 shows the colourized active vs. PM mass graphs for the 28:30 slip coupler. Using Figure 3.11 (a)–(i), the variation and mean of each independent variable across the feasible solution space is summarised. This summary is shown in Table 3.6. Most variables have physically small variations of < 5 mm, except the stack length which varies by more than 25 mm. Colour groupings are evident from the graphs. The two *regions* formed is briefly discussed. The first *region*, with $m_A < 3.5$ kg is characterised by shorter stack length (SL), larger PM height w_{pm}, larger coil height δ_{ch} and larger tooth height w_{rth}. Therefore, the larger the PMs and cross-sectional area, the shorter the stack length needs to be. The larger *region* with $m_A > 3.5$ kg is characterised by longer stack lengths, shorter PMs and smaller coils. An interesting conclusion may be made, namely that the 'empty' space between the two feasible solution *regions* may be a natural consequence of this specific slip coupler design.

Table 3.6: Variation in variables for the 28:30 slip coupler.

Independent variable	**Variation** (mm)	**Mean** (mm)
r_{so}	6.779	101.607
w_{sbi}	2.105	3.772
SL	25.485	46.761
δ_{pm}	5.21 [%]	82.60 [%]
w_{pm}	2.319	3.159
δ_{ch}	4.04 [%]	85.75 [%]
w_{rtw}	3.347	5.321
w_{rth}	4.332	14.677
w_{rbi}	3.320	3.695

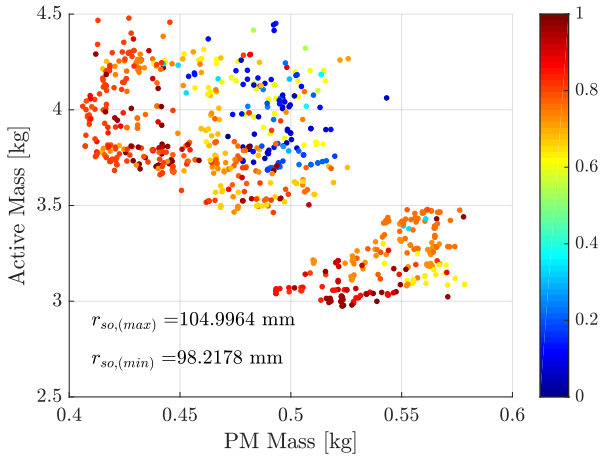

(a) Stator outside radius, r_{so}

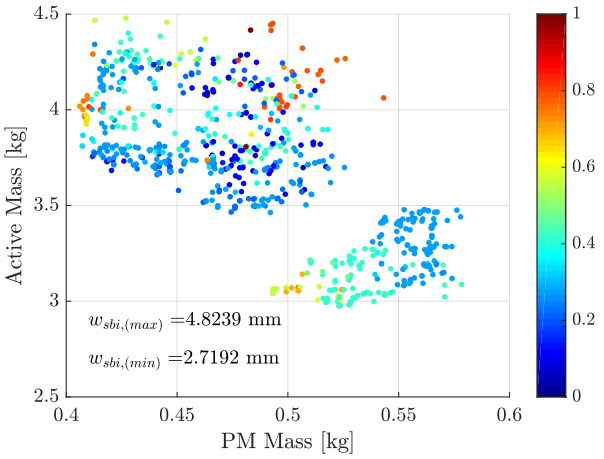

(b) Stator back iron width, w_{sbi}

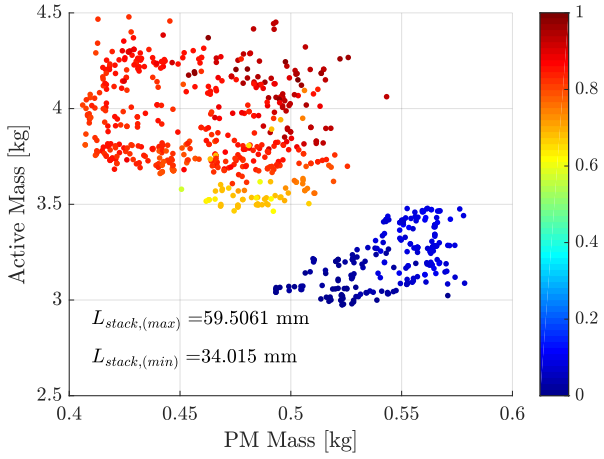

(c) Stack length

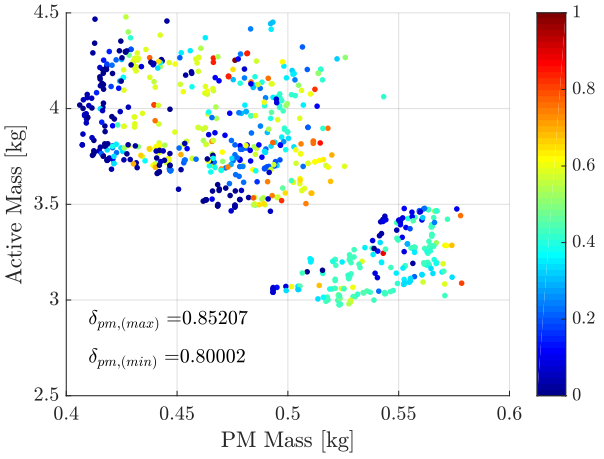

(d) PM width pitch, δ_{PM}

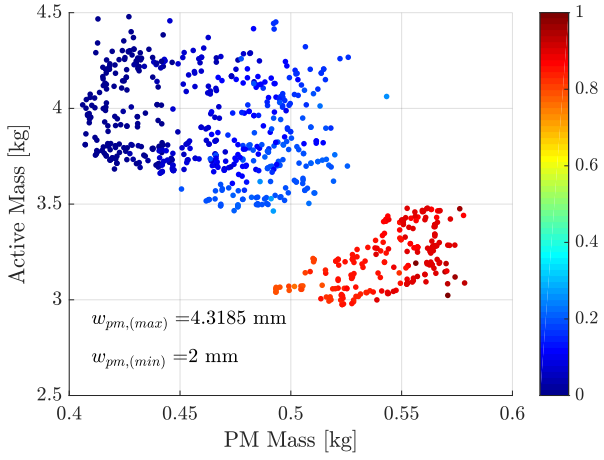

(e) PM height, w_{PM}

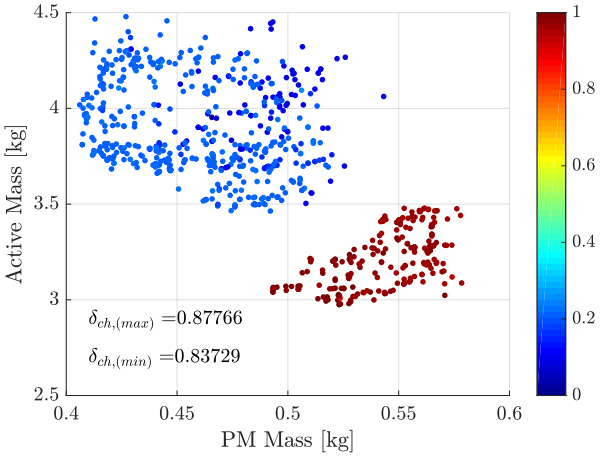

(f) Coil height, expressed as fraction of tooth height, δ_{ch}

Figure 3.11: Scatter charts showing the Active vs. PM Mass of the 28:30 slip coupler, with colourization indicating the effect of the independent variables.

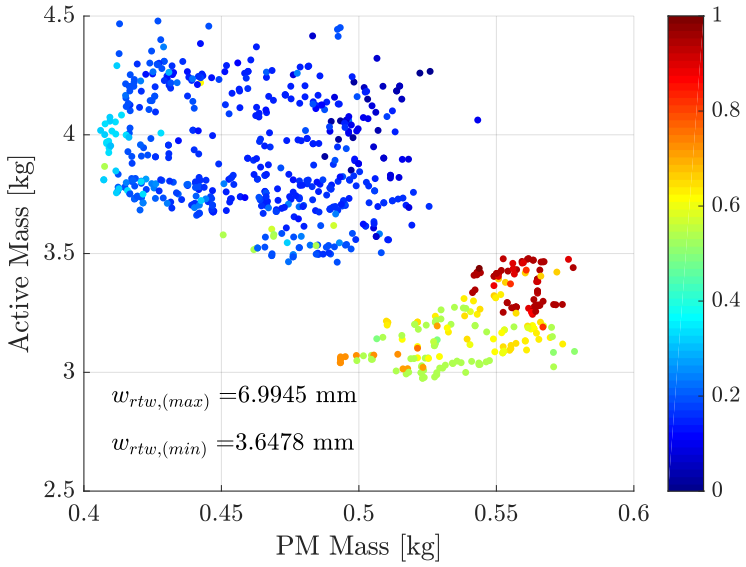

(g) Tooth width, w_{rtw}

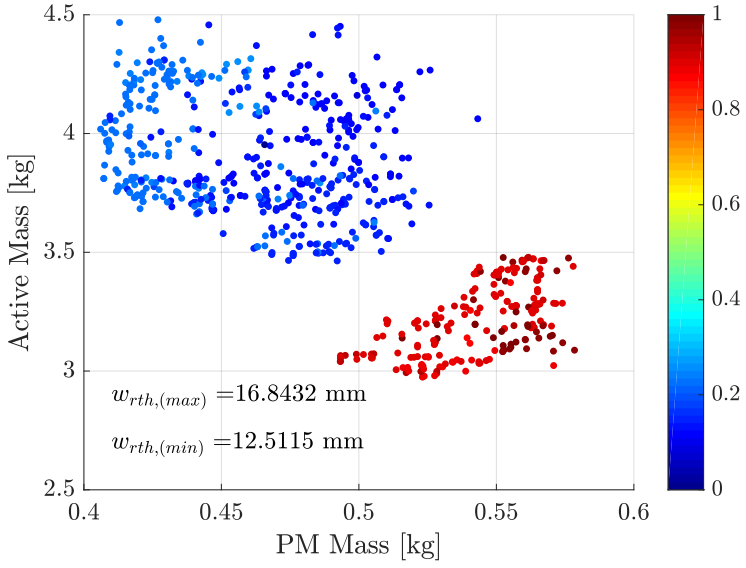

(h) Rotor tooth height, w_{rth}

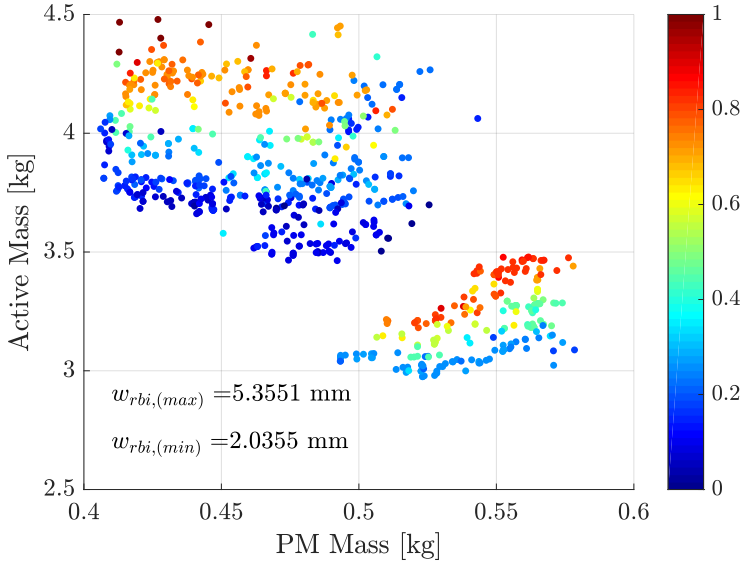

(i) Rotor back iron width, w_{rbi}

Figure 3.11: Scatter charts showing the Active vs. PM Mass of the 28:30 slip coupler, with colourization indicating the effect of the independent variables.

3.7.2 The 84:90 slip coupler evaluation

Figure 3.12 shows the colourised feasible solution space generated by the NSGA-II algorithm for the 84:90 slip coupler. The variation and mean of each independent variable across the feasible solution space is summarised in Table 3.8. The variations in design are not as consistent as is the case with the 28:30 slip coupler. The stack length and stator radius vary the most of all the design variables, followed by the coil height.

The feasible solutions $\boldsymbol{x}$ generated by the optimisation shows a single trend, namely maximised stator radius r_{so} and minimised magnet width pitch δ_{pm} as shown in Figure 3.12 (a) and (d), respectively. The current density constraint, as shown in Figure 3.10 (a), was close to 4 $\mathrm{A \cdot mm^{-2}}$ throughout the entire feasible solution space. The non-dominated solutions $\boldsymbol{x}^*$ show the smallest magnet height values closest to the Pareto-front. The optimised tooth height w_{rth} and width w_{rtw} remain remarkably consistent throughout each iteration of the optimisation. There is no significant variation in stack length, except for a small number of outliers.

Table 3.8: Variation in variables for the 84:90 slip coupler.

Independent variable	**Variation** (mm)	**Mean** (mm)
r_{so}	17.012	170.301
w_{sbi}	5.503	5.897
SL	10.984	75.871
δ_{pm}	4.47 [%]	42.36 [%]
w_{pm}	0.847	3.688
δ_{ch}	11.72 [%]	86.13 [%]
w_{rtw}	0.977	3.489
w_{rth}	2.496	17.361
w_{rbi}	2.708	4.363

3.7.3 Comparative summary

Before showing the relationships between the independent variables and objective functions of the two designs, the reader is reminded that the rated speed of the two slip couplers differs by a factor of 3.78 (the gear ratio in the wind turbine drivetrain, as is shown later). For the sake of brevity, the 28:30 slip coupler is denoted by subscript SM and the 84:90 by LM. The mean values as summarised in Tables 3.6 and 3.8 is used to define the relationships between the two machines. The independent variables of the two machines

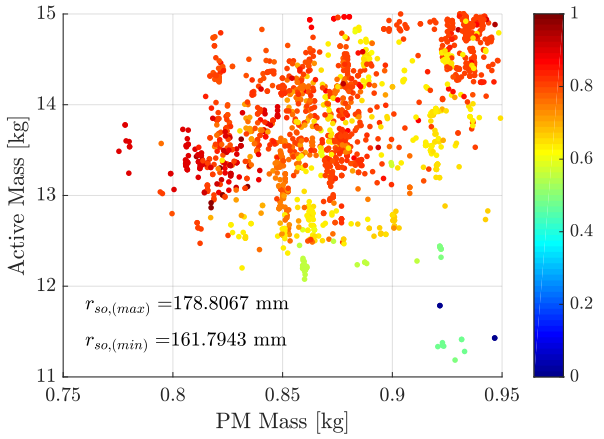

(a) Stator outside radius, r_{so}

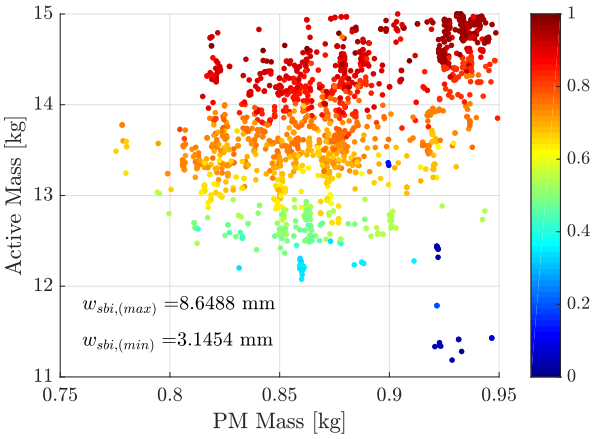

(b) Stator back iron width, w_{sbi}

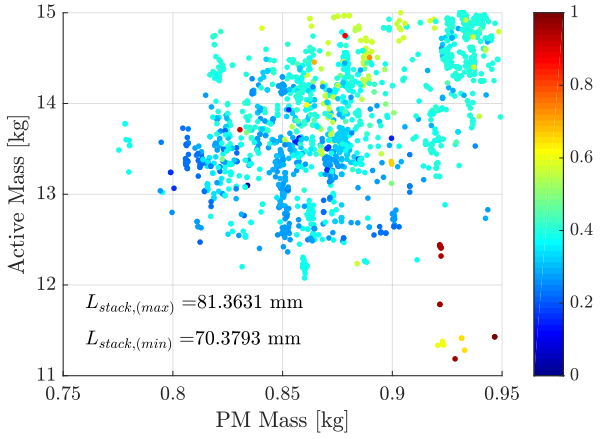

(c) Stack length

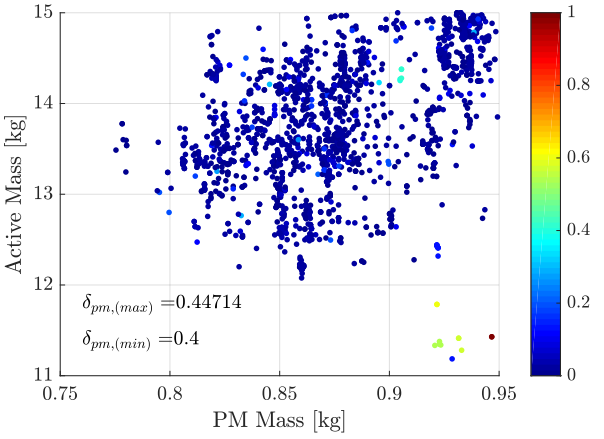

(d) PM width pitch, δ_{PM}

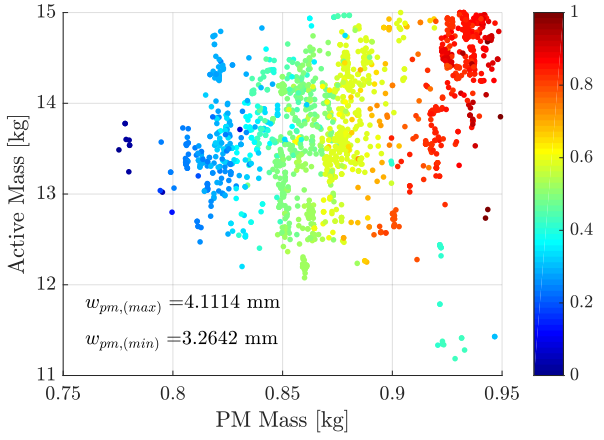

(e) PM height, w_{PM}

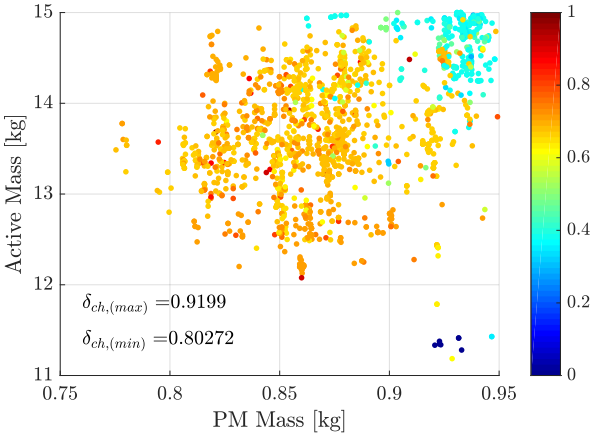

(f) Coil height, expressed as fraction of tooth height, δ_{ch}

Figure 3.12: Scatter charts showing the Active vs. PM Mass of the 84:90 slip coupler, with colourization indicating the effect of the design variables.

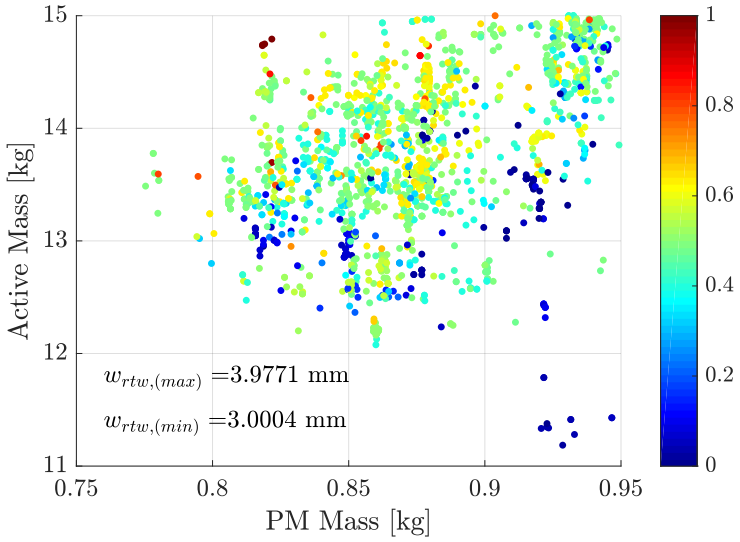

(g) Tooth width, w_{rtw}

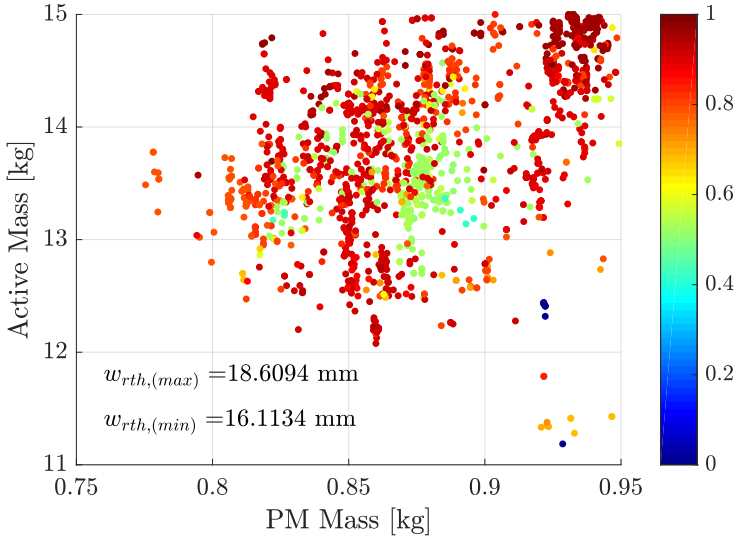

(h) Rotor tooth height, w_{rth}

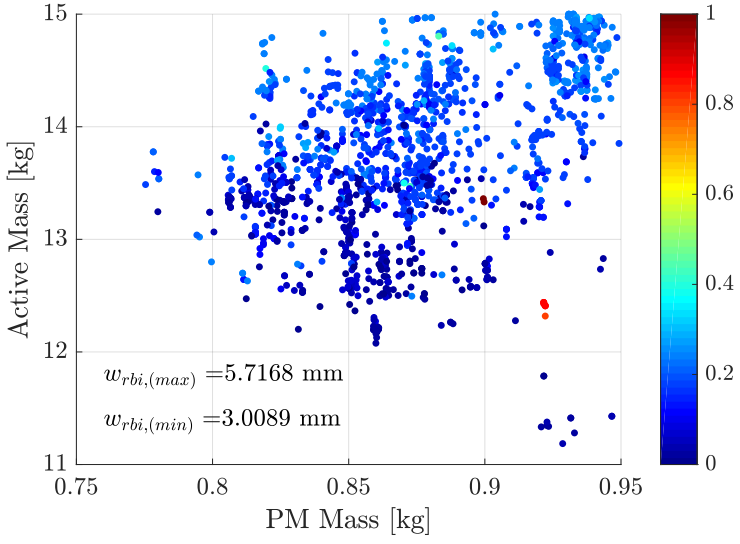

(i) Rotor back iron width, w_{rbi}

Figure 3.12: Scatter charts showing the Active vs. PM Mass of the 84:90 side slip coupler, with colourization indicating the effect of the design variables.

relate as follows:

$$\begin{aligned} r_{so,LM} &= 1.67 \cdot r_{so,SM} \\ w_{sbi,LM} &= 1.56 \cdot w_{sbi,SM} \\ SL_{LM} &= 1.62 \cdot SL_{SM} \\ \delta_{pm,LM} &= 0.51 \cdot \delta_{pm,SM} \\ w_{pm,LM} &= 1.17 \cdot w_{pm,SM} \\ \delta_{ch,LM} &= 1.00 \cdot \delta_{ch,SM} \\ w_{rtw,LM} &= 0.66 \cdot w_{rtw,SM} \\ w_{rth,LM} &= 1.18 \cdot w_{rth,SM} \\ w_{rbi,LM} &= 1.18 \cdot w_{rbi,SM} \end{aligned} \tag{3.17}$$

The selected solutions shown in Table 3.2 and 3.3 is compared in terms of active and PM mass. Hence,

$$m_{A,LM} = 3.35 \cdot m_{A,LM} \tag{3.18}$$

$$m_{PM,LM} = 1.46 \cdot m_{PM,LM} \tag{3.19}$$

When considering the total mass, $m_{T,LM} = 3.09 \cdot m_{T,SM}$; which is close to the speed ratio of 3.78. From Eq. (3.17) the stator outer radius r_{so}, stator back iron width w_{sbi} and stack length SL differ by a factor of roughly 1.6 between the two machines. The magnet pitch, which determines the magnet width, is half in the 84:90 machine.

3.8 Concluding remarks

The MOO problem for the slip coupler has been defined. The optimisation algorithms used in this study, namely the NSGA-II and the MMFD have been discussed. The NSGA-II requires careful parameter selection regarding initial population size, and the mutation and crossover probabilities. The MMFD algorithm requires less input, but careful consideration is required when selecting the starting points of the optimisation as well as defining the geometric bounds of the optimisation problem. A Pareto-optimal front has been generated for both designs. The 28:30 slip coupler has a final active mass of 3.645 kg and PM mass of 0.568 kg. The mass reduction is a significant improvement over the 28:30 slip coupler with a top-bottom winding topology, with which the results were compared. The 84:90 slip coupler has a final active mass of 12.197 kg and PM mass of 0.832 kg. The current density and specific torque of both machines have been discussed. The influence of the independent variables on the generated feasible region of each slip coupler is discussed. The total mass of the two slip couplers differs by 3.09, which is close to the speed ratio of 3.78. These results are verified in the subsequent chapter, using commercially available software.

Chapter 4

Design Performance Evaluation

In this chapter, the performance of the two slip coupler designs are determined by comparing the `Semfem` optimisation results with commercially available FE software. The `Ansys Maxwell 16.0` software is chosen because it has a trustworthy history in the use of electric machine design. Firstly, the time-transient performance of the slip couplers are evaluated at steady-state slip speed. The performance over a broader range of slip speeds is also discussed. There are harmonic components present in the `Maxwell` solutions, and the influence of this harmonic component on the slip coupler performance is discussed. Finally, the results are discussed and general recommendations on the design performance are made.

4.1 Verification software

In this section, some aspects of the verification software are briefly discussed. The `Ansys Maxwell 16.0` is a commercially available software package, capable of solving complex 3D FE problems [29]. There are two options available for 2D designs, namely *2D Solution* and *RmxPart*. The former was chosen, due to the flexibility of constructing the geometry of the slip coupler. The user does not have any influence on the underlying architecture of the *Maxwell 2D solver*. However, as was shown in the latter part of Chapter 2, the solution mesh and correct winding resistance and inductance values are crucial for an accurate solution.

4.1.1 Transient finite element solver

Figure 4.1 shows the magnetic flux lines and geometries as generated in `Maxwell` and `Semfem`. The *Transient magnetic solver* is used to determine the currents, flux linkages, developed torque and other machine performance parameters. The voltages in the windings are forced to zero, and the solver is allowed to determine the currents and flux linkages generated over time. The conductor types are *stranded* (as opposed to *solid*) with each

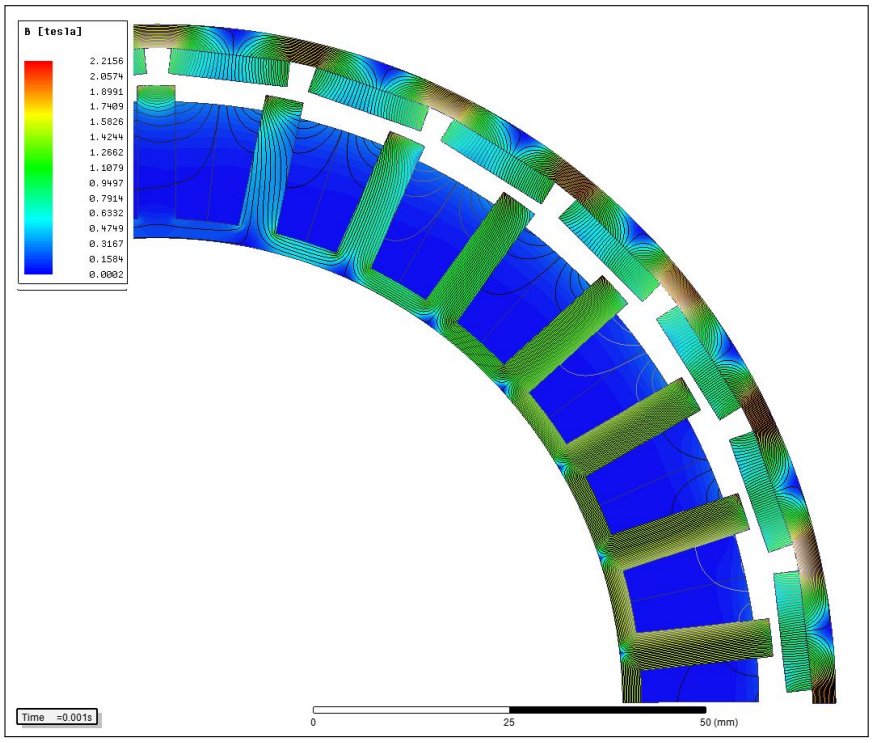

(a)

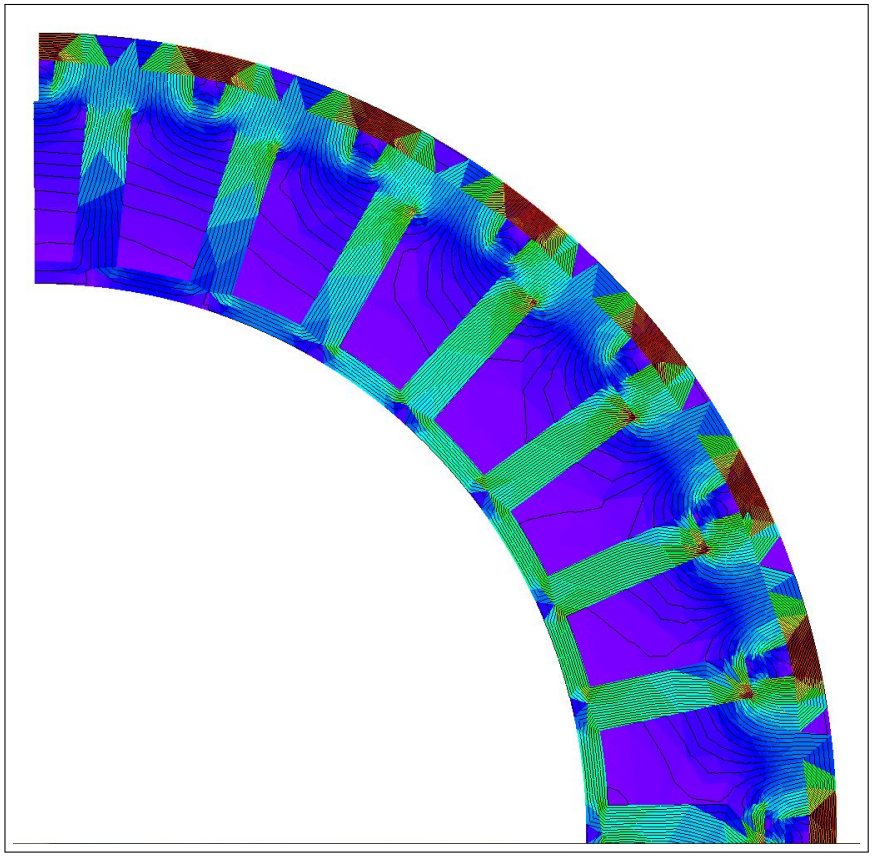

(b)

Figure 4.1: Magnetic flux lines as generated in (a) `Ansys Maxwell` and (b) `Semfem`.

winding defined as a single conductor coil. The *stranded* option requires the user to specify the winding resistance and end-winding inductance. Conductor losses are defined by I^2R and eddy effect losses only. Due to the low slip frequency, the skin effects are neglected in the analysis. As mentioned in Chapter 2, the core losses are neglected.

4.1.2 Limitations of results

The results obtained in this chapter have a number of limitations, which are:

- The slip coupler performance is only evaluated at 22 °C and all thermal effects are neglected.
- Mechanical stresses have not been considered in either the design or performance evaluation.
- There is no physical system with which to compare the results obtained by either software package.
- The fill factor cannot be set in the `Maxwell 2D Solution` solver. Therefore, although the windings are geometrically equivalent in `Semfem` and `Maxwell`, the effective cross-sectional area is 5 % larger in `Maxwell` (in `Semfem` the fill-factor is 0.95). This 5 % difference in conductor cross-sectional area will result in a 5 % decrease in resistance (see Appendix B). Ohm's law states that $I = {}^{V}/_{R}$ (A), therefore, a 5 % decrease in resistance will mean a 5 % increase in the current flowing through the conductor. Therefore, it is expected that the current solved for in `Maxwell` is roughly 5 % larger than the current solved in `Semfem`.

4.2 Rated performance characteristics

The performance characteristics of the 28:30 and 84:90 slip couplers, operating at their respective steady-state slip speeds, are discussed in this section. This discussion includes a comparison of the torque, radial flux density in the airgap as well as the flux linkages and current waveforms in the windings.

4.2.1 28:30 slip coupler

Figure 4.2 shows the flux linkages and current waveforms present in the windings. Figure 4.2 (a) shows that the flux linkage in the winding is very much sinusoidal. Both `Semfem` and `Maxwell` produce nearly identical waveforms. The flux linkage peaks at about 817 mWb·t. Figure 4.2 (b) shows the current waveforms of the A and B phases of a three-phase set. Here, the peak current according to `Semfem` is roughly 374.2 A, and according to `Maxwell` it is roughly 392 A; a 4.54 % difference in results. Referring back

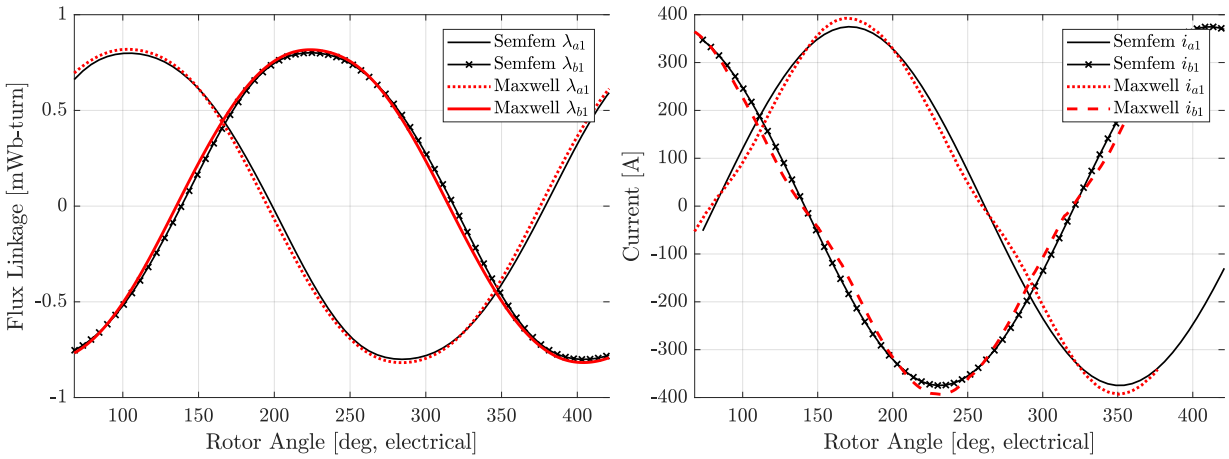

(a) (b)

Figure 4.2: The 28:30 slip coupler `Semfem` and `Maxwell` solutions at rated conditions, showing (a) the winding flux linkage and (b) the current waveform for a single winding.

to Section 4.1, this discrepancy is due to the winding cross-sectional area difference and is, therefore, correct. Both waveforms are slightly distorted. This distortion is due to the presence of a third harmonic current component and is addressed in the subsequent section.

Figure 4.3 (a) shows the rated torque of the 28:30 slip coupler. The mean torque for both `Semfem` and `Maxwell` is roughly 1 *pu*. However, the `Semfem` torque ripple (see Eq. (2.19)) is 1.40 % and in `Maxwell` it is 6.13 %, which is a large and unexpected difference. In Chapter 2, the torque ripple is assumed to be < 3 %, which is disproven here. The radial flux density in the airgap, $\boldsymbol{B}_R$, across two poles is compared in Figure 4.3 (b). The `Maxwell` curve is slightly more jagged than in `Semfem`. However, as was shown in Chapter 2, if the mean torque is the same for the two machines, then the mesh is deemed acceptable. The $\boldsymbol{B}_R$ is roughly trapezoidal, and the density peaks at around 888.9 mT.

4.2.2 84:90 slip coupler

Figure 4.5 (a) shows the flux linkage waveforms in the windings of the 84:90 slip coupler. `Maxwell` shows a peak of 1.316 mWb·t, whereas `Semfem` shows a value of 1.466 mWb·t. This means a difference of 10.23 %. Figure 4.5 (b) shows the current waveforms at rated conditions, where some distortion is evident in the current waveforms. The peak `Semfem` current is roughly 290 A and `Maxwell` 277 A, which means there is 4.55 % difference in peak current.

Figure 4.4 (a) shows the torque comparison between `Maxwell` and `Semfem` at rated operating conditions. The `Semfem` output torque is 132 N · m (considered to be 1 pu), and the `Maxwell` torque is roughly 0.878 pu. This means a 0.112 pu difference between `Semfem` and `Maxwell`. The radial flux density, $\boldsymbol{B}_r$, in of the 84:90 slip coupler is shown in Figure 4.4 (b). The peak $\boldsymbol{B}_r$ value is 762 mT in `Semfem` and 816 mT in `Maxwell`. Both curves show similar

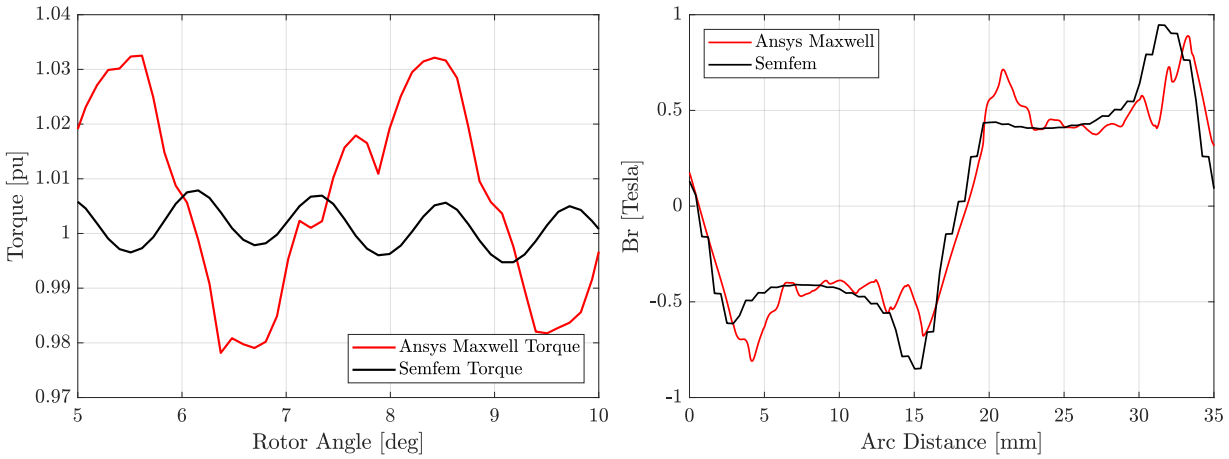

(a) (b)

Figure 4.3: The 28:30 `Semfem` and `Maxwell` generated solutions at rated conditions, showing (a) the stead-state torque and (b) the radial flux density over two pole pitches in the airgap.

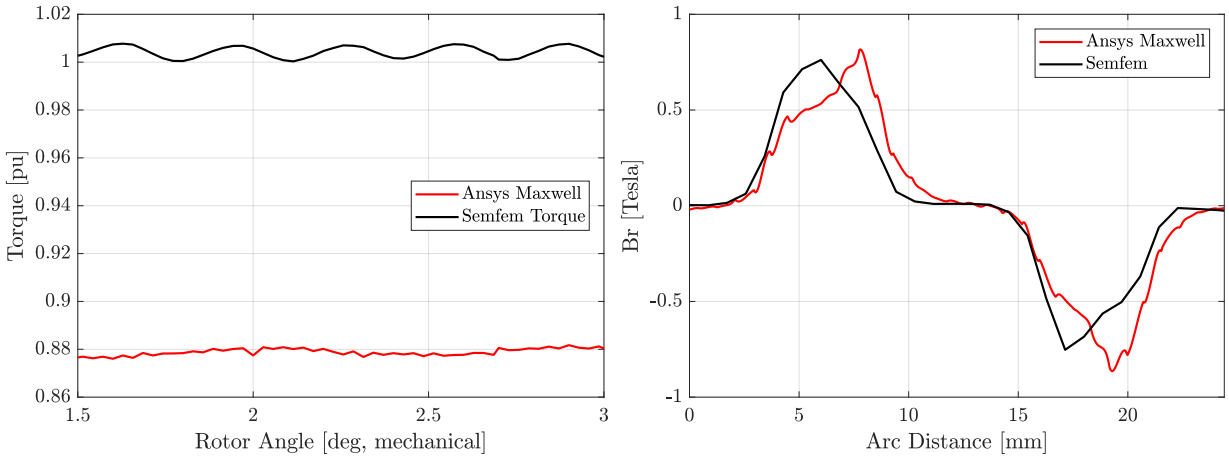

(a) (b)

Figure 4.4: The 84:90 slip coupler `Semfem` and `Maxwell` solutions at rated conditions, showing (a) the steady-state torque and (b) the radial flux density over two pole pitches in the airgap.

trends, with a large *flat* section at 0 T, followed by a peak $\boldsymbol{B}_r$; which may be due to the width of the PMs, which are about $0.41 \cdot \theta_{PM}$. Explained differently, the width of the PM is 41 % the arc of the pole pitch angle of the slip coupler. Compared to the width of a slot, this is quite small and it follows that the waveforms are not perfectly sinusoidal.

4.3 Characteristic machine performance

In this section, the characteristic machine performance of each slip coupler is evaluated. The torque, torque ripple, current density and losses are evaluated at different slip values.

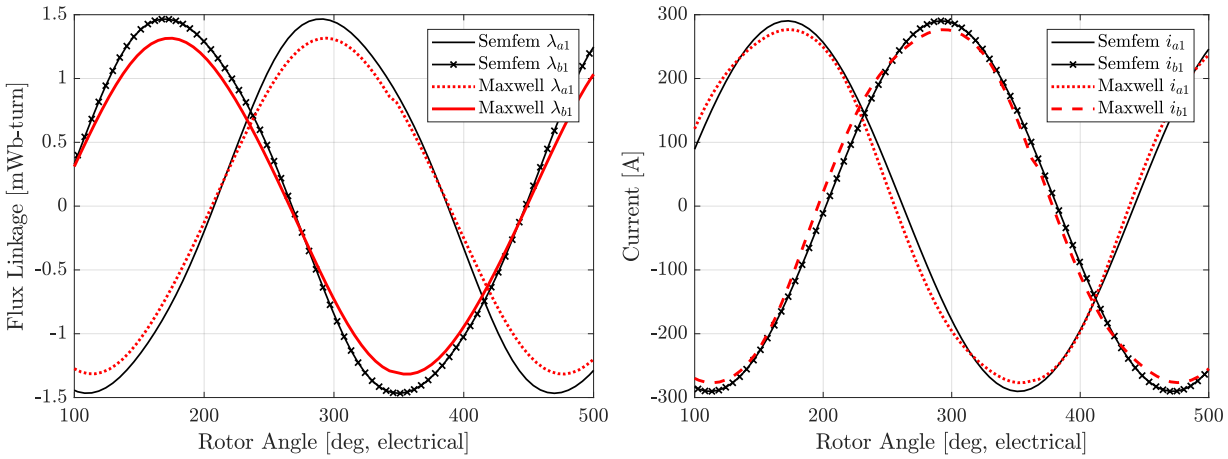

Figure 4.5: The 84:90 slip coupler `Semfem` and `Maxwell` solutions at rated conditions, showing (a) the winding flux linkage and (b) the current waveform for a single winding.

4.3.1 28:30 slip coupler

Figure 4.7 shows the current density and conductor losses vs. slip comparison. Figure 4.7 (a) shows a good correlation between the `Semfem` and `Maxwell` results. The current density is nearly identical up to 4 % slip. A deviation occurs between the two curves at a slip of more than 4 %. Figure 4.7 (b) shows that there is a good correlation between the two curves up to 4 % slip.

Figure 4.6 shows the torque and torque ripple vs slip for the 28:30 slip coupler. Figure 4.6 (a) shows good correlation between `Semfem` and `Maxwell`. The breakdown torque, defined as the point at which the developed torque begins to decrease, is 1.896 of the rated torque in `Semfem` and 1.844 in `Maxwell` at roughly 10 % slip. There is a 5 % difference between the breakdown torque values for the two software packages, which confirms that the `Semfem` solution is correct. However, from Figure 4.6 (b), the torque ripple in `Semfem` compares poorly with the `Maxwell` estimation. The torque ripple becomes roughly constant after 4 % slip for both cases. At lower slip values, the `Maxwell` torque ripple is much larger than `Semfem` and further investigation is required. Overall, the `Semfem` and `Maxwell` solutions compare well and this confirms the `Semfem` solution. The deviation in torque ripple is cause for concern and needs to be confirmed using either other EM software or to construct this slip coupler and physically test the torque ripple.

4.3.2 84:90 slip coupler

Figure 4.8 shows the `Semfem` and `Maxwell` current density J_c and conductor losses. From (a), the current density values are very much the same. The current density is nearly identical at 5 % slip. At 3 % slip, however, there is a 8.56 % difference between the J_c values as

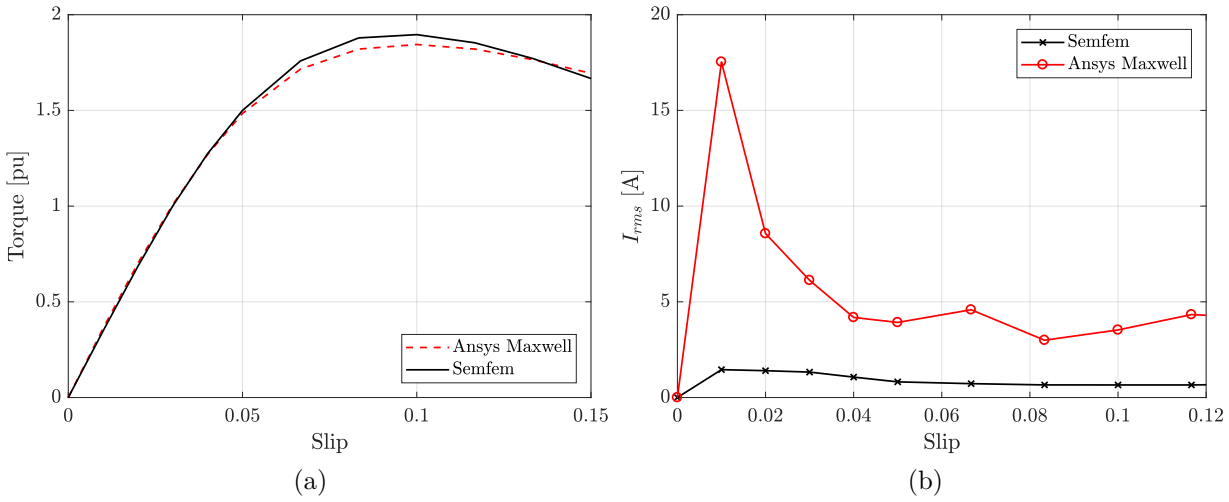

Figure 4.6: Characteristic torque performance of the 28:30 slip coupler showing (a) the torque vs slip and (b) the torque ripple for different slip values.

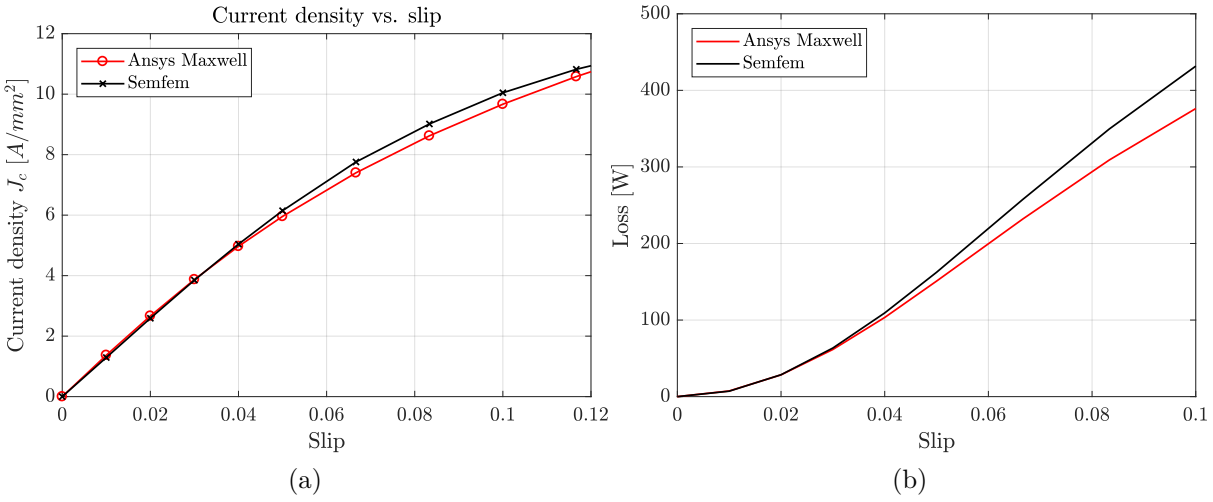

Figure 4.7: Characteristic current performance of the 28:30 slip coupler showing (a) the current density curve (b) the conductor losses for different slip values.

generated by `Semfem` and `Maxwell`. This error is consistent with the 10 % difference in the torque and flux linkages peak magnitude in the windings at steady-state operation. Figure 4.8 (b) shows the estimated conductor losses of the two software packages. At 3 % slip there `Semfem` estimates the conductor losses at 57 W and `Maxwell` at 54 W, indicating a 5 % error in results. Again, these results indicate that the `Semfem` results are acceptable.

The characteristic torque vs slip curve and torque ripple of the 84:90 slip coupler is shown in Figure 4.9. From (a), the estimated torque is nearly identical at 2 % slip. For higher slip values deviation occurs, with the `Maxwell` solution indicating that the breakdown torque point occurs at around 4 % slip at 0.91 the rated torque. This is far below what `Semfem` estimated the breakdown torque to be. From Figure 4.9 (b), the torque ripple

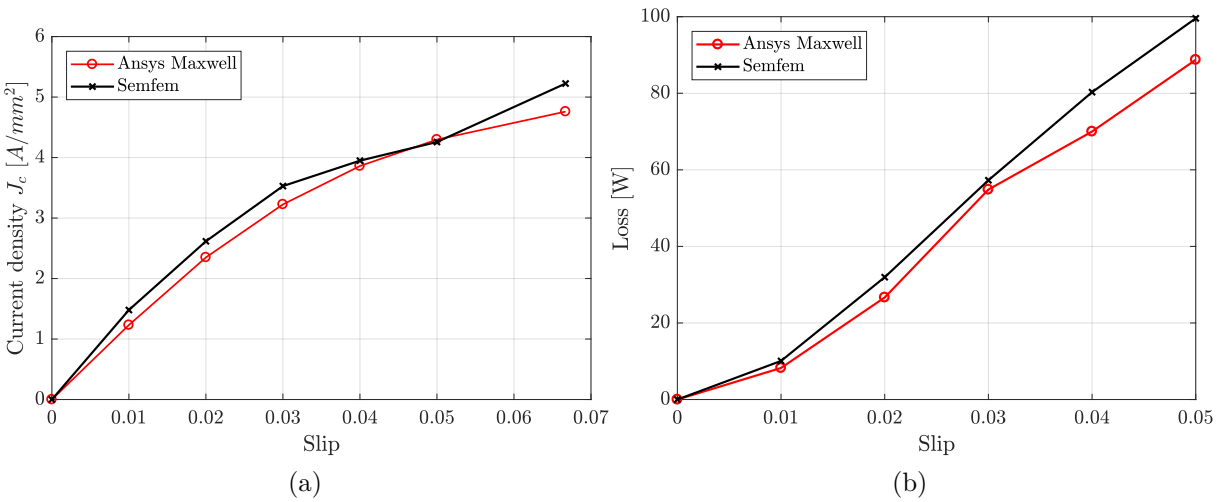

Figure 4.8: Characteristic performance of the 84:90 slip coupler showing (a) the current density curve (b) the conductor losses for different slip values.

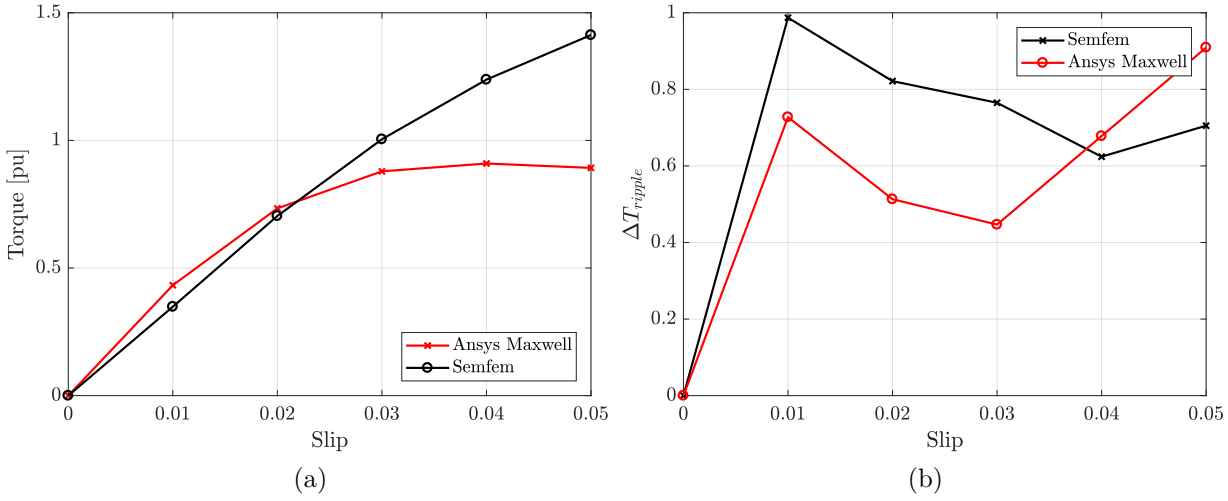

Figure 4.9: Characteristic performance of the 84:90 slip coupler showing (a) the torque vs slip and (b) the torque ripple for different slip values.

for the 84:90 slip coupler is below 1 %. Unlike the 28:30 slip coupler, `Maxwell` estimates a lower torque ripple than `Semfem`. This `Maxwell` outcome is worrisome because both slip couplers have the same winding factor, which should mean that there is a small difference in torque ripple values between the two slip couplers.

4.4 Influence of zero-component current

In this section, the influence of the zero-component current on the performance of the slip coupler is discussed. The current waveforms generated by `Maxwell`, as shown in Section 4.2, are not perfectly sinusoidal. This waveform distortion is due to higher harmonic components which are present in the slip coupler designs. Only the third-harmonic component

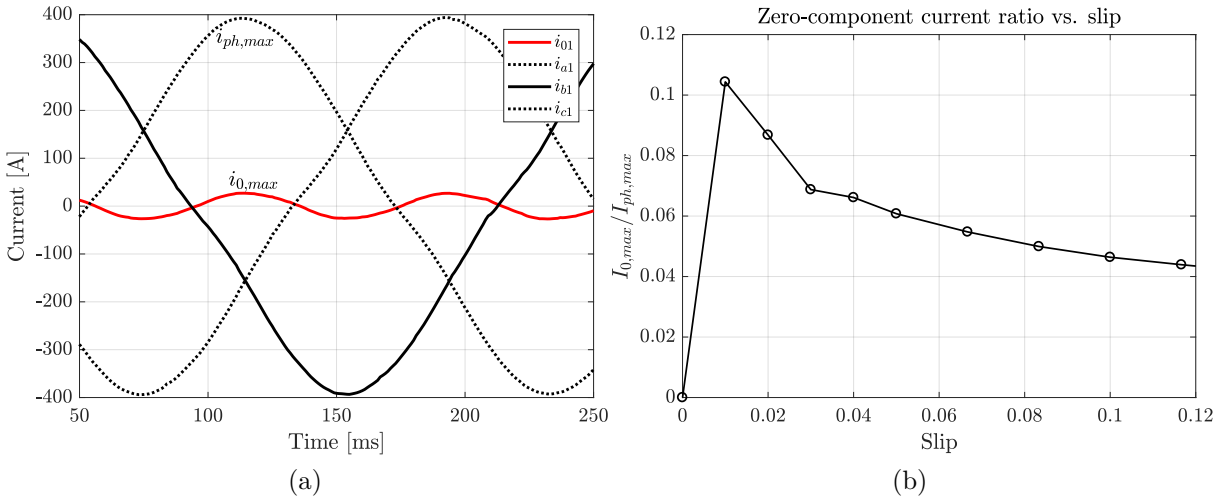

(a) (b)

Figure 4.10: Zero-component current for the 28:30 slip coupler with (a) the *abc* phase current with zero-component current and (b) ratio of maximum zero-component current to real phase current for different slip values.

is considered in this section which, according to the Park's transformation shown in Appendix A, is considered the same as the zero-component flux-linkage in the windings. This zero-component flux-linkage is

$$\lambda_{0,i} = \tfrac{1}{3}(\lambda_{a,i} + \lambda_{b,i} + \lambda_{c,i}) \tag{4.1}$$

where subscript i refers to the i^{th} three-phase set in the slip coupler. This zero-component flux-linkage causes a zero-component current in the windings

4.4.1 28:30 slip coupler

The effect of the instantaneous zero-component current, i_0, on the current waveforms of the 28:30 slip coupler is discussed. Figure 4.10 (a) shows the *abc* currents generated by `Maxwell`, with the i_0 shown. The figure shows the definition of the maximum phase current, $i_{ph,max}$ and zero-component current $i_{0,max}$ at 3 % slip speed. The i_0 current has a frequency of $3f_{sle}$, where f_{sle} is the electrical slip frequency of the slip coupler. To determine the magnitude of $i_{0,max}$ compared to the $i_{ph,max}$, Figure 4.10 (b) shows the $i_{0,max}/i_{ph,max}$ for different slip values. For a 1 % slip speed, $i_{0,max}$ is nearly 10 % that of the phase current maximum. This ratio steadily decreases as the slip speed increases. This may account for the torque ripple found in Figure 4.6 (b), because the harmonic component distorts the current wave, which in turn distorts the developed torque. The decrease in $i_{0,max}/i_{ph,max}$ means that although $i_{ph,max}$ increases as slip increases, $i_{0,max}$ remains relatively unchanged.

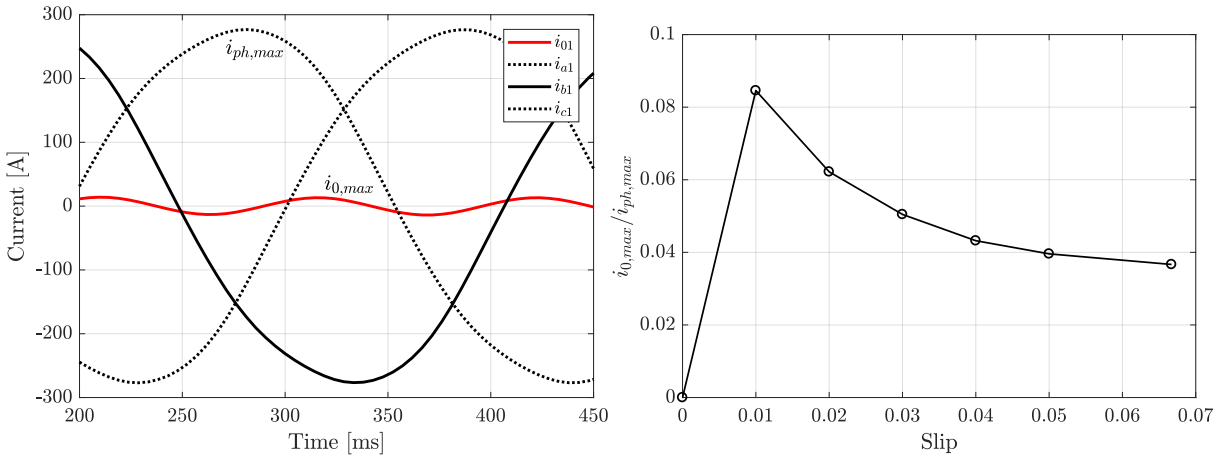

(a) (b)

Figure 4.11: Zero-component current of the 84:90 slip coupler with (a) the *abc* phase current with zero-component current and (b) ratio of maximum zero-component current to real phase current for different slip values.

4.4.2 84:90 slip coupler

The effect of instantaneous zero-component current, i_0, on the current waveforms of the 84:90 slip coupler is discussed. Figure 4.11 (a) shows the maximum zero-component current, $i_{0,max}$, as well as the *abc* phase current, $i_{ph,max}$, in `Maxwell`. These windings currents are generated at rated conditions of 3 % slip. There are a number of observations that can be made from the figure, especially when compared to Figure 4.10 (a). Firstly, note that $i_{0,max}$ is not in phase with the *abc* phase currents. The i_0 current again has a frequency of $3f_{sle}$, which means it is a third-harmonic component. The $^{i_{0,max}}/_{i_{ph,max}}$ ratio of the two slip couplers, shown in Figure 4.11 (b), are similar in magnitude and shape, yet the `Maxwell` torque ripple of the 84:90 slip coupler is much lower than that of the 28:30 slip coupler.

Therefore, even though there are similarly sized third-harmonic current and flux components in both slip couplers, there is no clear link between the harmonic component and the `Maxwell` torque ripple. The torque ripple in `Semfem` in both slip couplers is < 3 %, which is not the case for the 28:30 slip coupler in `Maxwell`. The only way to validate the `Maxwell` results is by using similar FEM software and validating this result, or physically constructing the two slip couplers and verifying the torque ripple.

4.5 Discussion of results

Table 4.1 summarises the results of the `Semfem` and `Maxwell` generated solutions. The slip coupler designs were optimised using `Semfem` for a slip of 0.03 and the results at rated conditions are compared in this section. The rated torque of the 28:30 slip coupler is lower than the optimisation constraint of $32 < T < 36$ Nm as described in Chapter 3. This may

necessitate a slight adjustment to the final dimensions of the slip coupler. Regardless, the `Maxwell` and `Semfem` current density, flux-linkage and radial flux density results compare well for both designs. The 84:90 slip coupler has a 12.51 % error in peak torque and flux-linkage results at rated conditions, but this may be due to a difference in `Semfem` and `Maxwell` torque angle. The torque ripple ΔT_{ripple} of the 28:30 slip coupler is greater than the 84:90 slip coupler, with a near 6 % point difference in `Maxwell` results. This lack of consistency in the `Maxwell` ΔT_{ripple} results necessitates further investigation, possibly by using alternative EM-FEM software and also physically constructing the slip couplers.

There are third-harmonic flux-components present in the windings, which causes the developed current waveforms in the windings to distort. There is no clear link, however, to this harmonic component and the torque ripple in the slip couplers. Overall, the `Semfem` results are confirmed by `Maxwell`, and a stress and thermal analysis is recommended. The 28:30 slip coupler is especially promising, because it has a low active mass and its performance is confirmed by `Maxwell`. The 84:90 slip coupler design requires some adjustment, due to the low torque breakdown value in `Maxwell`, but this design remains promising due to the low torque ripple value.

Table 4.1: Summary of results for the two slip coupler designs.

Performance parameter	**28:30**		**84:90**	
	Semfem	**Maxwell**	**Semfem**	**Maxwell**
Torque (Rated) T_R [N · m]	32.54	31.67	132.58	116.00
Torque Ripple (Rated) ΔT_{ripple} [%]	1.33	6.13	0.765	0.447
Breakdown Torque T_B [N · m]	61.61	59.94	262.98	120
Peak Radial Flux Density (Rated) $\boldsymbol{B}_r$ [mT]	946	886	762	816
Peak Coil Flux Linkage $\lambda_{ph,max}$ [mWb·t]	0.801	0.817	1.464	1.315
Peak Current (Rated) $I_{ph,max}$ [A]	374	392	290	277
Current Density (Rated) J_c [A · mm^{-2}]	3.851	3.873	3.528	3.226
Loss (Rated) P_c [W]	63.47	61.58	57.27	54.84

4.6 Concluding remarks

Both slip coupler designs have been optimised, and the performance has been verified using `Maxwell`. These slip couplers are designed and optimised specifically for a small scale wind turbine drivetrain. The 84:90 slip coupler has not yet been modelled in the wind turbine drivetrain, and this is the main focus of the subsequent chapter.

Chapter 5

Dynamic Wind Turbine Model

In this chapter, a wind turbine model is modelled with and without a slip coupler. The complete wind turbine drivetrain model is referred to as the *system*, or simply the *turbine*. The turbine rotor, which is the rotating hub and blades of the wind turbine, is referred to simply as the *rotor*. This should not be mistaken with the rotor part of the slip coupler. Figure 1.7 (a) shows the schematic diagram of the complete wind turbine drivetrain. Firstly, an overview of the rated drivetrain conditions is presented. After that, the transfer function of each component in the system is derived and discussed. Finally, the unforced and steady-state response of the wind turbine is evaluated from a mechanical perspective.

5.1 Model overview

In this section, the 2.2 kW wind turbine parameters and modelling approach are presented. The simulation software, namely `Matlab Simulink` is briefly discussed.

5.1.1 System description

Figure 5.1 shows the major *blocks* of a wind turbine model; namely the aerodynamic-, drivetrain- and generator block. The rotational velocities are noted as Ω, with subscripts t and g referring to the turbine and generator, respectively. When torque is discussed in the context of *produced* or *generated* torque, the large symbol T is used. When torque is discussed in the context of a transfer function, it is noted as τ. The 2.2 kW wind turbine, available as part of `Stellenbosch University` wind energy research group, is used as a case study. The parameters of this system are presented in Table 5.1.

The wind turbine is modelled with the aim of testing the torque behaviour of the 84:90 slip coupler when subjected to typical dynamic conditions found in any wind turbines. The 28:30 slip coupler, which is placed on the generator-side of the drivetrain has been tested extensively in the same system [30], and the study is, therefore, not repeated here.

Table 5.1: 2.2 kW Wind turbine model parameters

Parameter	Description	Value
$P_{g,rated}$	Rated generator power	2.2 kW
$V_{g,rated}$	Rated generator / grid voltage	230 / 400 V
$I_{g,rated}$	Rated generator current	3.2 A
F_s	Grid frequency	50 Hz
R_g	Per phase winding resistance	5.2 Ω
L_{ds}	Generator d inductance	66.6 mH
L_{qs}	Generator q inductance	67.8 mH
L_{es}	Per phase end-winding inductance	16.1 mH
λ_{ms}	Flux contribution of PM	1.17 Wb·turn
J_g	Generator inertia	0.2 kg · m^2
J_t	Turbine inertia	20kg · m^2
T_t	Rated turbine torque	132 N · m
T_g	Rated generator torque	35 N · m
N_p	Number of generator poles	10
G_R	Gear ratio	1:3.78
$\upsilon_{w,rated}$	Rated wind speed	11 m · s^{-1}
$n_{t,rated}$	Turbine speed	160 rpm

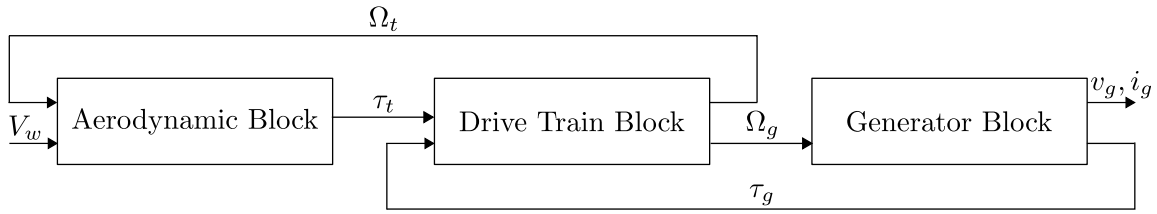

Figure 5.1: Simplified wind turbine diagram with interactions shown between drivetrain components.

The 28:30 behaviour as in Figures 4.6–4.7 is characteristic of a typical slip coupler, and the magnitude of the response is adjusted to suit the 132 N · m requirement.

5.1.2 Simulation software

The `Simulink` software, as made available by `Matlab`, is used to model the wind turbine. The turbine simulation is considered a *stiff* system because comparatively high shaft coefficient values relative to the rest of the wind turbine model. For this reason, the *ODE15s* solver is chosen. The relative simulation error tolerance is set to $1 \times 10^{-9} \cdot$ A *variable* time step is chosen, but the rule of thumb for fixed time steps is that the minimum time step should be 4 to 8 times smaller than the smallest time-constant of the model. The time tolerance is specified as $1 \times 10^{-12} \cdot$s.

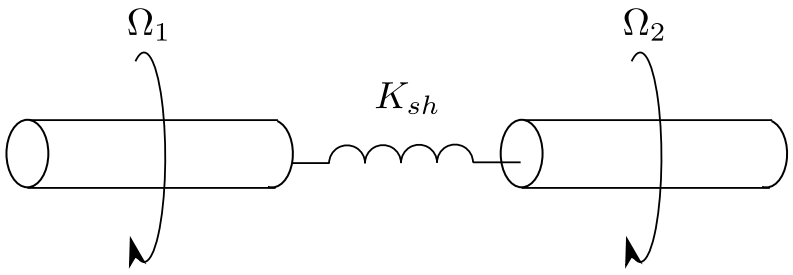

Figure 5.2: Model of a flexible shaft with spring constant K_{sh}.

5.2 Drivetrain model

This section provides the drivetrain *building blocks* of the wind turbine model. The flexible shaft, slip coupler transfer function and the gearbox model are discussed.

5.2.1 Flexible shafts

There are two connecting shafts considered. Firstly, there is a shaft which connects the stator of the slip coupler to the input side of the gearbox. The second shaft connects the generator to the output side of the gearbox. The shaft is considered flexible with negligible losses, and can be modelled as a torsional spring. This simplified model is shown in Figure 5.2. The spring constant, K_{sh}, is a function of the shaft material, and shaft geometry. The spring constant is expressed as

$$K_{sh} = \frac{J_{sh}G}{l_{sh}}, \tag{5.1}$$

where

J_{sh} = Shaft polar moment of inertia,
G = Modulus of rigidity,
l_{sh} = Length of the shaft.

It is assumed that the shafts are 0.5 m in length and the shaft radius is $r_{sh} = 0.02$ m, which means that $J_{sh} = 25.133$ µm^4. Furthermore, the shafts are assumed to be stainless steel, with a modulus of rigidity of $G = 77.2$ GPa. From Eq. (5.1), this means that $K_{sh} = 38.804$ kN $\cdot$ m $\cdot$ rad^{-1}. The torque transferred is generally expressed as

$$\tau_{sh} = K_{sh}(\theta_1 - \theta_2). \tag{5.2}$$

When taking the derivative of Eq. (5.2), the shaft equation becomes

$$\frac{d\tau_{sh}}{dt} = K_{sh}(\Omega_1 - \Omega_2). \tag{5.3}$$

Both shafts are considered equal in size and length for this model.

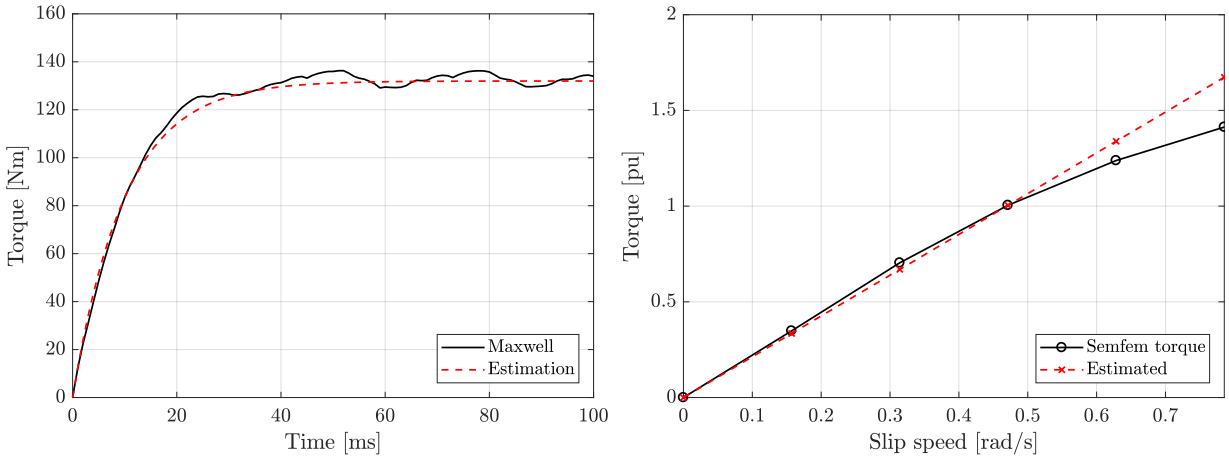

(a) (b)

Figure 5.3: The 84:90 slip coupler slip response used in the system model transfer function, showing (a) the transient torque response generated in `Maxwell` and (b) the slip coupler torque vs. slip curve.

5.2.2 Slip coupler transfer function

In this section, the slip coupler transfer function is discussed. The transient behaviour of the 28:30 slip coupler, as determined by `Maxwell`, is used to calculate the electric time constant. The torque vs. time curve is generated using `Maxwell's` *transient solver*. Figure 5.3 (a) shows the `Maxwell` and estimated torque response for a step input at 3 % slip. The estimated torque response of the slip coupler to a step input is

$$T_{sc}(t) = T_{ss} \cdot \left(1 - e^{-t/\Gamma_{sc}}\right) = 132 \cdot \left(1 - e^{-t/0.01}\right), \tag{5.4}$$

where

T_{sc} = Torque of slip coupler,
T_{ss} = Steady-state torque equal to T_t at slip of 3 %,
Γ_{sc} = Time constant of the slip coupler.

From the above equation, it is seen that Γ_{sc} is 10 ms. The mechanical time constant of the turbine is defined as $\Gamma_t = {}^{J_t}/_{B_t} = {}^{20}/_{0.079} = 253.16$ s, which means $\Gamma_{sc} << \Gamma_t$. Therefore, the transient behaviour of the slip coupler is neglected and it can be modelled as a simple torsional damper, expressed as

$$\tau_{sc} = C_{sc}\Omega_{sl}, \tag{5.5}$$

where Ω_{sl} [rad $\cdot$ s^{-1}] is the slip speed and C_{sc} is the damping coefficient of the slip coupler. The damping coefficient is simply the slope of the linear section in Figure 5.3 (b), which is $C_{sc} \approx 263$ [N $\cdot$ s $\cdot$ rad^{-1}]. The straight line response produced by Eq. (5.5) is also shown on the figure.

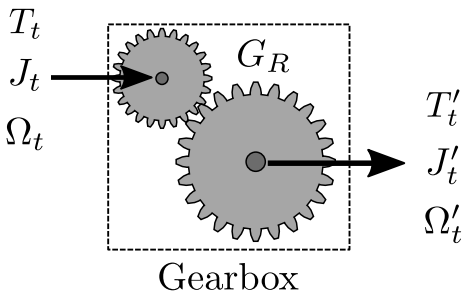

Figure 5.4: Depiction of a gearbox.

5.2.3 Simple gearbox model

The gearbox is placed along the drivetrain of the wind turbine. It has the purpose of increasing the rotational speed of the *rotor* by the effective gear ratio, G_R of the gearbox. The gearbox is assumed to be ideal, such that there are no losses present. The gearbox inertia is considered negligible, which is true for most wind turbine drivetrains. Figure 5.4 shows a depiction of the gearbox, which transmits the rotor torque T_t and angular velocity Ω_t. The equations of motion for a simple two-mass model with a gearbox is given in Appendix C.5. The magnitude of the transmitted parameters depend on the gear ratio G_R, such that,

$$T'_t = \frac{T_t}{G_R}, \tag{5.6}$$

$$J'_t = \frac{J_t}{G_R^2}, \tag{5.7}$$

$$\Omega'_t = G_R \Omega_t. \tag{5.8}$$

This simple model has some limitations, especially when higher-order disturbance frequencies act on the system. These disturbances are often a result of non-linearities such as flexible shafts, flexible gear housing, teeth and bearings. These components are not considered due to the increased complexity in analysis.

5.3 Generator model

In this section, the PMSG transfer function is discussed. The dq equivalent circuit of the PMSG is shown in Figure 5.5. All of the SG parameters are presented in Table 5.1. The dq voltages of the PMSG are expressed as

$$v_{qs} = -R_s i_{qs} - L_{qs}\frac{di_{qs}}{dt} - \Omega_e L_{ds} i_{ds} + \Omega_e \lambda_{ms}, \tag{5.9}$$

$$v_{ds} = -R_s i_{ds} - L_{ds}\frac{di_{ds}}{dt} + \Omega_e L_{qs} i_{qs}, \tag{5.10}$$

where $\Omega_e = (N_P/2)\Omega_g$. The core losses are neglected in this analysis. The dq inductances are

$$L_{qs} \quad = \frac{\lambda_{qs}}{-I_{qs}} + L_{es}, \tag{5.11}$$

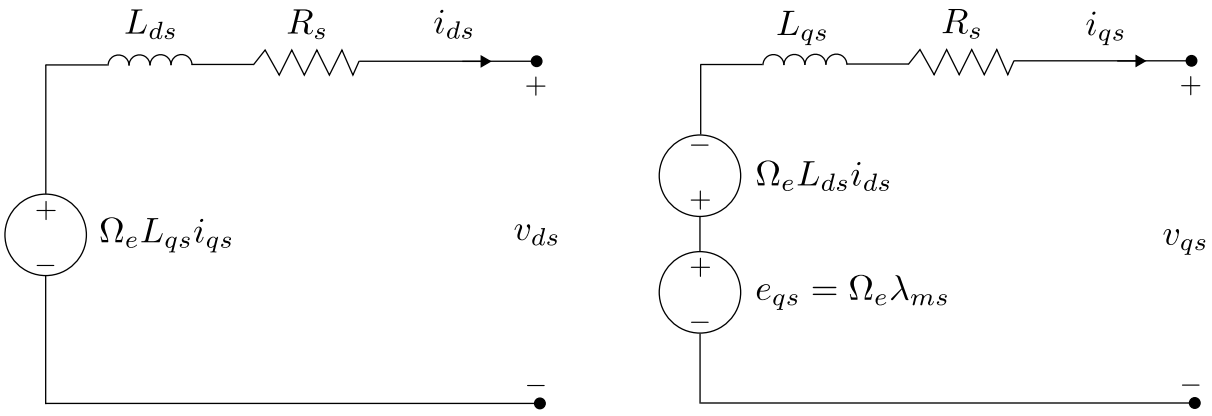

Figure 5.5: The dynamic dq-equivalent circuit of a grid-connected PMSG.

$$L_{ds} = \frac{\lambda_{ds} - \lambda_{ms}}{-I_{ds}} + L_{es}. \tag{5.12}$$

The torque generated by the generator is expressed as

$$T_g = \tfrac{3}{4} N_p [(L_{qs} - L_{ds}) i_{ds} i_{qs} + \lambda_{ms} i_{qs}]. \tag{5.13}$$

The PMSG is direct grid-connected, which means that the 10-pole SG needs to rotate at 600 rpm to maintain the grid connection. The transfer function, as implemented in `Matlab Simulink`, is presented in Appendix D.3.

5.4 Dynamic wind turbine model

The drivetrain is modelled with and without a slip coupler placed on the turbine side. The full drivetrain consists of a PMSG, gearbox, flexible shafts and slip coupler. The wind-energy conversion is simplified as a torque input in all the models. The equations of motion for the model without a slip coupler are presented in Appendix C.7. The equations of motion for the complete drivetrain are shown in Appendix C.8. The transfer functions of both models are given in Appendix D. As previously mentioned, the model parameters are presented in Table 5.1. The outcomes of the simulations are as follows:

- To model the system with and without a slip coupler on the turbine-side of the drivetrain. The generator is firstly disconnected ($\tau_g = 0$ N $\cdot$ m) from the drive train, and the unforced system response to a torque pulse is measured. The purpose of this simulation is to determine the shaft torsional behaviour.
- To determine the effect of the gear ratio, G_R, on the unforced system response. The complete drivetrain model, with a turbine-side slip coupler, is used to simulate the system behaviour.
- To determine the drivetrain response at steady-state operating conditions, with a PMSG connected to the grid. At steady-state, the drivetrain is only modelled with a slip coupler, because the system is inherently unstable without it.

- To determine the drivetrain behaviour for two types of wind conditions. These conditions are wind gust and tower shadow interference, and the slip coupler's ability to reduce these disturbances is evaluated.

5.5 Unforced response evaluation

The unforced behaviour of the drivetrain, with and without a slip coupler, is evaluated. The generator torque feedback is removed from the model, and the transient behaviour is investigated. Also, different gear ratios are used, and the generator inertia is adjusted accordingly. Specifically, the input torque experienced across the shaft into the gearbox is evaluated.

5.5.1 Transient response for a turbine-side pulse

In this section, the transient behaviour of both drivetrain models are evaluated. The purpose of this evaluation is to determine the benefit of placing a slip coupler on the turbine-side of the wind turbine. A 20 N · m pulse, with a frequency of 6.1 Hz, is generated on the turbine-side of the drivetrain. Figure 5.6 shows the drivetrain shaft speeds, before and after the gearbox. The rotational velocities of the shafts are not as directly affected due to the slow mechanical time constant of the system. The two shaft speeds differ by the G_R value. From Figure 5.6 (a), there is a slight oscillating component in the rotational shaft speed. The response in (b) shows that the slip coupler removes the torsional *ringing* component present in the shafts. Figure 5.7 shows the torque response of the drivetrain to such a pulse. In (a), the drivetrain experiences significant torsional vibration when a slip coupler is not present. In reality, there are other dissipating forces in the bearings

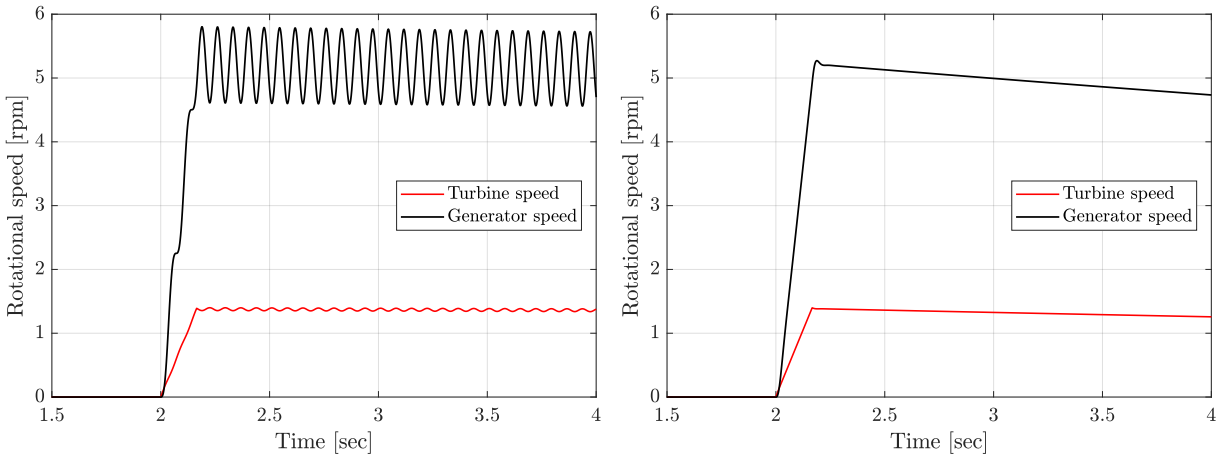

Figure 5.6: Unforced drivetrain response, for $G_R = 3.78$, to a turbine-side pulse, showing (a) the drivetrain rotational speed when no slip coupler is present and (b) the rotational shafts speed before and after the gearbox when a slip coupler is present.

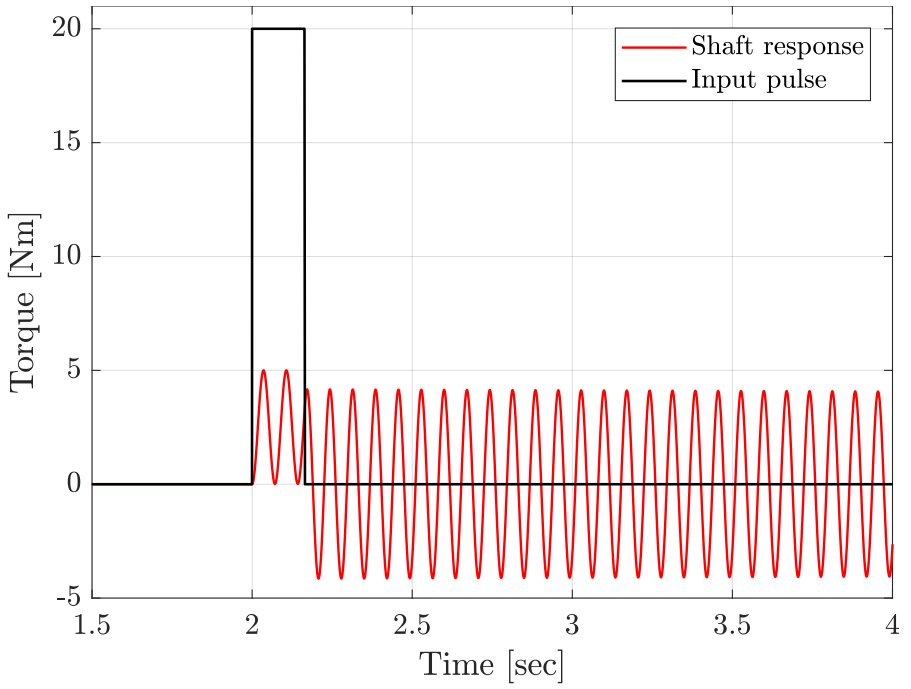

(a)

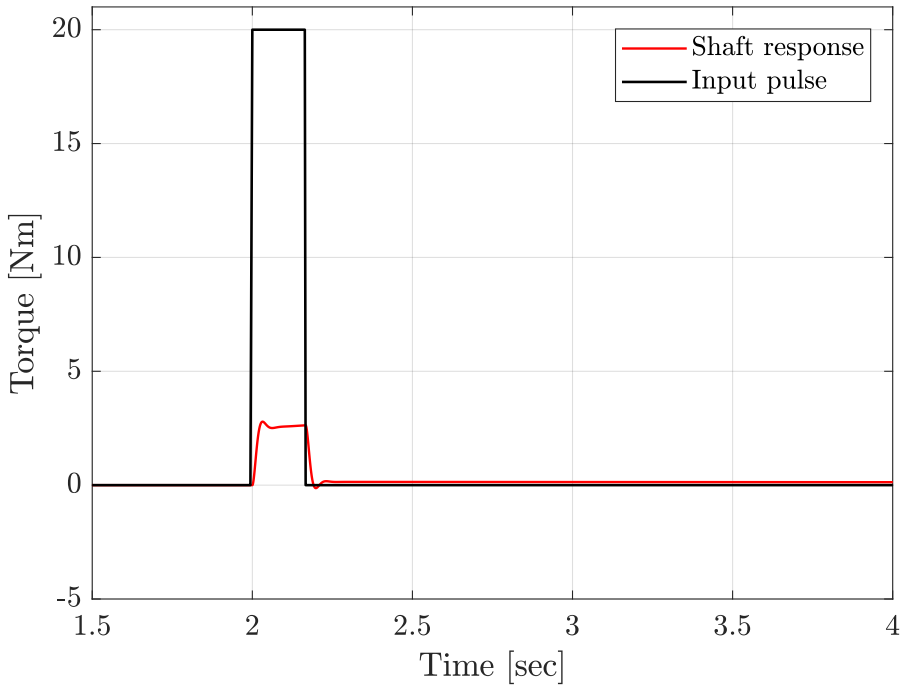

(b)

Figure 5.7: Transient torque response of the drivetrain for a turbine-side pulse, showing (a) the torque transfer into the gearbox when no slip coupler is present and (b) the torque transfer when a slip coupler is present.

and shafts which dampens the vibration sooner than is shown in the figure. Also, when the torsional vibrations are absorbed by the bearings and gearbox components, it directly contributes to decreased component lifetime. These dissipating forces do not completely remove the vibrational response. In contrast, the torque response of a drivetrain with a slip coupler, as in (b), is stable when compared the response in Figure 5.7 (a).

5.5.2 Effect of gear ratio on drivetrain response

The gear ratio of the gearbox directly affects the drivetrain response. Higher gear ratios increase the generator input speed, which means that the generator inertia decreases. Smaller generators, generally, have lower costs. Therefore, higher gear ratios are desirable. However, as will be shown in this section, higher gear ratios may have unwanted consequences. Firstly, it is assumed that the inertia of the generator is related to the gear ratio, G_R, as follows

$$J_g' = \left(\frac{J_g}{G_{R,new}}\right) G_{R,base}, \tag{5.14}$$

where

$G_{R,base}$ = Original gear ratio,
$G_{R,new}$ = Chosen gear ratio.

The above relationship is approximate and does not necessarily represent reality. However, the inertia difference between the two slip couplers in Chapter 3 approximates this relationship and adds credibility to the above assumption. The generator is pulsed with a 10 N $\cdot$ m, 1.5 Hz pulse, which is considered representative of an grid-side over-voltage condition during normal operation. The gear ratios used are $G_R \in (3.78, 7, 10)$, and the unforced shaft torque response is evaluated. In each case the generator inertia is adjusted according to Eq. (5.14). The transferred torque across the gearbox is expressed in Eq. (5.6). Therefore, for $G_R = 10$, a $\tau_g = 2$ N $\cdot$ m pulse translates to $\tau_{sh,1} = 20$ N $\cdot$ m response on the turbine side. In Figure 5.8, the torque response of the turbine shaft to a generator-side pulse is shown. As expected, the torsional response of the shaft on the turbine-side increases as G_R increases. Due to the short duration of the torque pulse, and the large mechanical time constant of the system, $\tau_{sh,1} \neq G_R \tau_g$. However, it is not recommended to increase the gear ratio beyond 7, because the system may become too sensitive to grid-side disturbances for higher values of G_R for this specific wind turbine.

5.5.3 Discussion of results

The unforced response of the 2.2 kW wind turbine is evaluated. The slip coupler has a beneficial impact on drivetrain stability and removes the torsional *ringing* experienced on the shafts on either side of the gearbox. Due to the slow mechanical time constant of the drivetrain, the rotational speed is not significantly affected by torsional vibration. However,

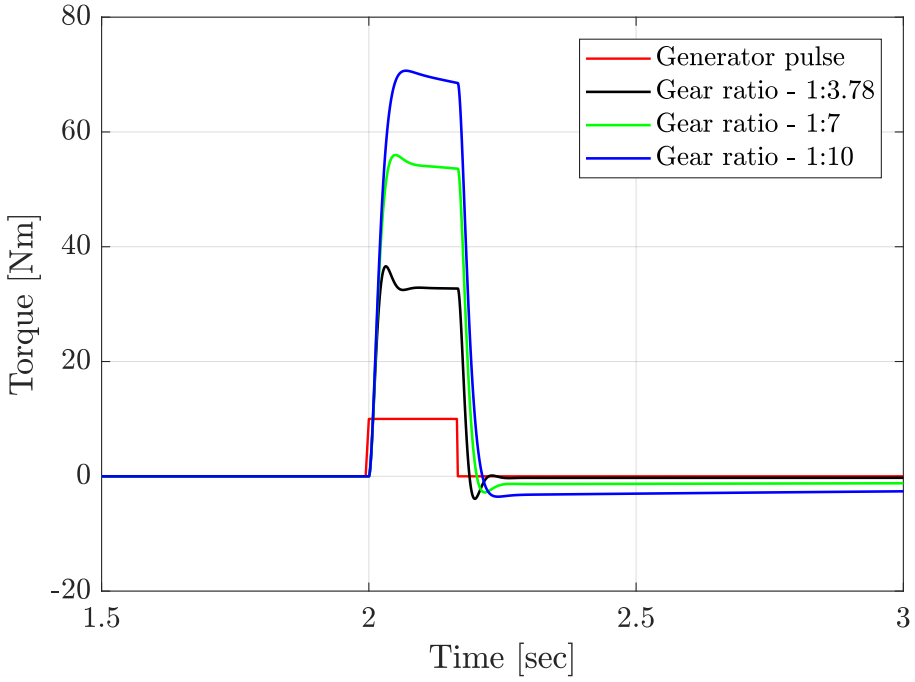

Figure 5.8: Drivetrain response to generator-side pulse, with different gear ratios investigated. Shown is the turbine-side shaft torque response to this pulse.

the slip coupler can reduce the magnitude of torsional vibration and perhaps allows a drivetrain to accommodate a gearbox with a larger gear ratio, than would otherwise be the case. However, higher gear ratios exacerbate grid-side fault conditions, and the gear ratio should be chosen with care.

5.6 Steady-state response evaluation

The PMSG is considered grid-connected for this investigation, which means that the generator torque is produced according to Eq. (5.13). The steady-state torsional response of the drivetrain is evaluated for two types of disturbances, namely a wind gust and $3f_p$ frequency interference. For a three-bladed turbine such as the one used in this case study the tower shadow interference contributes to $3f_p$ torque pulsations. The drivetrain is modelled with a slip coupler because the PMSG is not able to remain in stable steady-state operation without it.

5.6.1 Drivetrain response to wind gust

The wind gust component has a frequency of 3 Hz, with a magnitude of $0.21T_t$. This frequency is considered typical because wind gusts are generally slow-moving components. Figure 5.9 shows the turbine-side shaft response and the PMSG torque response to this component. In (a), the slip coupler does not filter out the 3 Hz component. Due to the slow mechanical time-constant, there is a delay in the torsional shaft response. Without

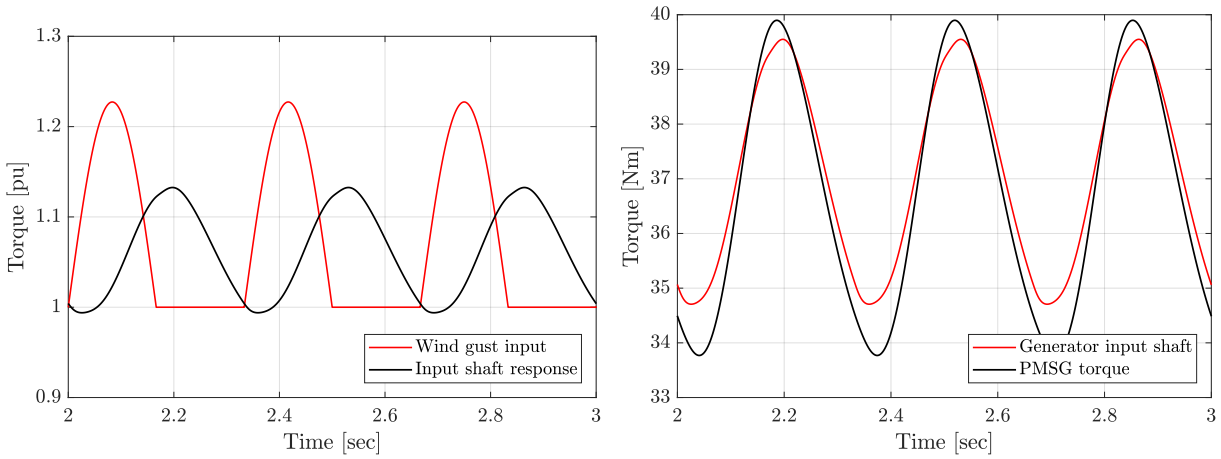

(a) (b)

Figure 5.9: Drivetrain (with slip coupler) torque response to a 3 Hz wind gust, showing (a) the wind gust component and turbine-side shaft torque response and (b) the generator-side shaft torque and PMSG torque.

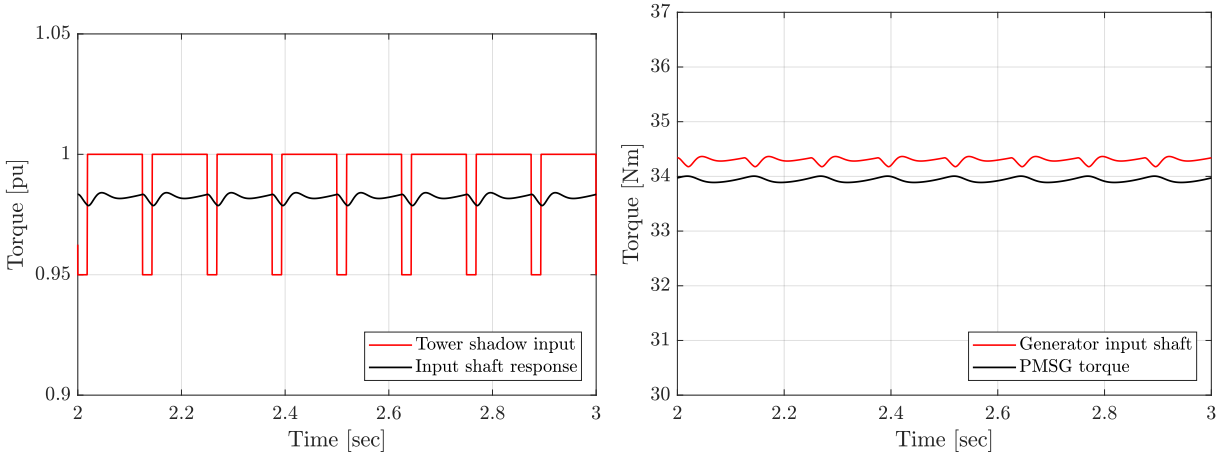

(a) (b)

Figure 5.10: Drivetrain (with slip coupler) torque response to a tower shadow interference, with (a) the tower shadow interference and turbine-side shaft torque, and (b) the generator-side shaft torque response and PMSG generated torque.

the slip coupler, however, this component would be enough to cause drivetrain instability. In (b), the generator torque responds directly to the increase in torque due to the wind gust. In conclusion, the slip coupler does not filter out a low-frequency component such as a wind gust.

5.6.2 Drivetrain response to tower shadow

In this section, the tower shadow interference is investigated. The tower shadow is approximated as a duty-cycle with a frequency of 8 Hz, and a pulse width of 12 %. The maximum torque loss due to tower shadow interference is assumed to be 5 % of the rated torque.

As previously mentioned, this component contributes to the $3f_p$ fluctuations of the wind turbine. Figure 5.10 shows the drivetrain response to this torque component. In (a), the tower shadow interference is shown, as well as the input shaft response to this component. The slip coupler minimises the torque response of the drivetrain to this component, which means that the gearbox also experiences less torsional vibration than would otherwise be the case. In (b), the generator shaft torque and PMSG torque is shown. The tower shadow interference has a negligible effect on the performance of the PMSG. In conclusion, tower shadow interference commonly occurs in all wind turbines, and a slip coupler placed on the turbine-side of the drivetrain significantly reduces this component.

5.7 Concluding remarks

A complete wind turbine drivetrain has been modelled, with and without a turbine-side slip coupler. The unforced response simulations show that the slip coupler removes higher-frequency torsional vibrations that act along the drivetrain. The gear ratio may be increased when a slip coupler is present, but for the 2.2 kW wind turbine the gear ratio should not exceed 1:7, due to increased system sensitivity to generator-side disturbances. In steady-state, the slip coupler is not able to filter out a 3 Hz wind gust torque, but stabilises the system. The slip coupler effectively removes the influence of tower shadow interference. In conclusion, the slip coupler is of great benefit in protecting the drivetrain from high-frequency torque components when placed on the turbine-side of a wind turbine, and further testing on a physical system is recommended.

Chapter 6

Conclusions and Future Work

In this thesis, two slip couplers have been designed and optimised for use in a 2.2 kW wind turbine. Both of these designs have the potential to make a small-scale wind turbine a more robust energy producing structure. The 28:30 slip coupler, when placed on the generator side of the drivetrain, is especially promising. The active mass of the 28:30 slip coupler has been reduced by almost half when compared to the slip coupler found in [1]. This reduction was made possible by making use of the NSGA-II and MMFD optimisation algorithms. The 84:90 slip coupler, when well designed, has the potential to reduce torque oscillations that occur due to turbine side wind disturbances. In this concluding chapter, the main findings of this study are discussed, together with the limitations of the results. Finally, some of the future work that stems from this research is discussed.

6.1 Research conclusions

The following conclusions are drawn from the research:

- From **Chapter 2**, it shows that the slip coupler is a polyphase electric machine, but can be evaluated using standard dq reference-frame equations. Both slip coupler designs have high efficiencies when taking only conductor losses into account. The 3D end-winding resistance and inductance is taken into account, which improves the accuracy of the evaluation. The slip frequency, which is a function of the number of poles, needs to be specifically chosen depending on the slip coupler placement along the drivetrain.
- The EM-FEA in `Python / Semfem` is a compelling, accurate and potentially fast method of evaluating the slip coupler performance. A static, electromagnetic FEA evaluation determines the slip coupler performance. Using `Semfem`, a geometric mesh is generated, and the static inductance values are estimated for a specified number of rotor positions. The inductance estimation method requires successive iterations to converge and can produce an accurate solution within four iterations. It is assumed

that the torque ripple is low enough not to have to evaluate more than one rotor position, which drastically reduces the simulation time. The mesh *fineness* is selected according to the best apparent trade-off between accuracy and required simulation time. In hindsight, the `Ansys Maxwell` results have shown that the torque ripple value may not be as low as was initially assumed. The FE script is well suited for use in optimisation, however, because of the comparatively low simulation time it takes to produce an accurate solution.

- In **Chapter 3**, the active mass of both slip couplers have been minimised using the NSGA-II and MMFD optimisation algorithms. The limitation to this optimisation is that the structural mass, such as bolts, fasteners and other components needed to construct the slip couplers is not considered. The thermal operating conditions have also not been considered, and the mechanical operating stresses are neglected. The optimised 28:30 slip coupler has an active mass of 3.65 kg, which is a significant reduction from the 7 kg design with which it was compared. The reason for this improvement is the use of the NSGA-II algorithm and a reduced overall simulation time without which the algorithm is too computationally expensive to use.

- In optimisation, Pareto-fronts are constructed for both slip couplers, as well as showing the dominated solution spaces generated by the `Visualdoc` optimisation software. Both slip couplers have very different feasible solution spaces, which is attributed to the different demands on the design. The NSGA-II optimisation parameters, such as the probability of mutation and cross-over needs to be carefully selected. Some studies in the literature have shown that the NSGA-II parameters need to be dynamically determined as the optimisation progresses. Unfortunately, `Visualdoc` does not allow the user this flexibility.

- By making use of colour gradients applied over the feasible solution space, further insight into the behaviour of both the slip coupler and optimisation is gained. The 28:30 slip coupler shows a clear *island* in the feasible solution space, which indicates that either the PM mass or conductor mass can be increased to increase the torque output of the design. The 84:90 does not show such an *island* because the optimisation algorithm struggled to keep the solutions within the feasible solution space.

- Some geometric relationships are derived by comparing the two slip coupler sizes and masses. The two slip couplers differ in mass by roughly the gear ratio of the drivetrain.

- In **Chapter 4**, both slip couplers have been simulated using the `Ansys Maxwell` software. The flux linkage, current density, losses and currents compare well with the `Semfem` results. The 28:30 slip coupler torque compares well in both software

packages, which confirms that `Semfem` is an excellent software to use in optimisation and performance evaluation.

- The 84:90 slip coupler torque, however, only compares well up to 2 % slip, after which the discrepancy between the two software results becomes large. The discrepancy is may be partly due to the *dq* transformation angle in `Semfem`, which differs from `Maxwell`.
- The 28:30 and 84:90 slip couplers are simulated in identical manners, yet `Maxwell` shows a 6 % torque ripple component for the 28:30 slip coupler and 1 % component for the 84:90 slip coupler. Both slip couplers have the same fundamental pole-to-slot ratio, and therefore this casts doubt on the `Maxwell` software package. This study is limited because the `Maxwell` results cannot be physically verified.
- In **Chapter 5**, the 84:90 slip coupler is simulated in a complete wind turbine drivetrain. This drivetrain has two flexible shafts, gearbox and generator components. The unforced response is evaluated and shows that a slip coupler filters out torque oscillations. The magnitude of the gear ratio is investigated, and the gear ratio can be increased to 7 when a slip coupler is present.
- Finally, the effect of tower shadow is significantly reduced during steady-state operation. The 3 Hz wind gust component is reduced but not removed by a slip coupler on the turbine side of the drivetrain.

6.2 Future work

There are some aspects of this study which present opportunities for future work. Some of the recommendations are:

- To physically construct and test both of the slip coupler designs presented in this study. Also, it should be attempted to measure the torque ripple present in these slip couplers under steady-state operation.
- To verify the slip couper designs using different EM-FEM software. `Maxwell` has proven to be adequate in confirming the results obtained in `Semfem`, but the torque and torque ripple discrepancies require external validation. A program such as `Siemens MagNet` may be suitable.
- After the 84:90 slip coupler is constructed, the results in Chapter 5 need to be physically confirmed. This is especially true for the flexible shafts, and perhaps also the gearbox. The torque oscillations are vibrational components which can be measured using accelerometers.

List of References

[1] P. J. J. van Wyk and M. J. Kamper, "Simplified analysis technique for double layer non-overlap multiphase slip permanent magnet couplings in wind energy applications," in *2015 IEEE International Electric Machines Drives Conference (IEMDC)*, May 2015, pp. 1317–1323.

[2] W. Baram and M. Knorr, "Synchronous couplings with smco5 magnets," *Proc. Second Intern. Workshop on Rare Earth-Cobalt Permanent Magnets and their Applications*, vol. 40, no. 1, p. 140, 1976.

[3] R. Hornreich and S. Shtrikman, "Optimal design of synchronous torque couplers," *IEEE Transactions on Magnetics*, vol. 14, no. 5, pp. 800–802, September 1978.

[4] X. Wang and D. Wang, "Calculation of eddy current loss and thermal analysis for adjustable permanent magnetic coupler," in *Proceedings of 2011 International Conference on Electronic Mechanical Engineering and Information Technology*, vol. 9, Aug 2011, pp. 4405–4408.

[5] A. S. Erasmus and M. J. Kamper, "Computationally efficient analysis of double pm-rotor radial-flux eddy current couplers," *IEEE Transactions on Industry Applications*, vol. 53, no. 4, pp. 3519–3527, July 2017.

[6] M. H. Nagrial, J. Rizk, and A. Hellany, "Design of synchronous torque couplers," *International Journal of Mechanical and Mechatronics Engineering*, vol. 5, no. 7, pp. 1319–1324, 2011.

[7] A. Canova and F. Cavalli, "Design procedure for hysteresis couplers," *IEEE Transactions on Magnetics*, vol. 44, no. 10, pp. 2381–2395, Oct 2008.

[8] J. H. J. Potgieter and M. J. Kamper, "Design of new concept direct grid-connected slip-synchronous permanent-magnet wind generator," *IEEE Transactions on Industry Applications*, vol. 48, no. 3, pp. 913–922, May 2012.

[9] K. S. E. Skaar and R. Nilsen, "Distribution, coil-span and winding factors for pm machines with concentrated windings." June 2006.

[10] J. Manwell, J. McGowan, and A. Rogers, *Wind Energy Explained: Theory, Design and Application*. John Wiley and Sons, 2010.

[11] I. P. Girsang, J. S. Dhupia, E. Muljadi, M. Singh, and L. Y. Pao, "Gearbox and drivetrain models to study dynamic effects of modern wind turbines," in *2013 IEEE Energy Conversion Congress and Exposition*, Sept 2013, pp. 874–881.

[12] N. S. F. M. Murad, M. N. Kamarudin, S. M. Rozali, and M. H. Hairi, "Achieving optimum tip-speed-ratio of a two-mass wind turbine system," in *2016 IEEE International Conference on Power and Energy (PECon)*, Nov 2016, pp. 757–762.

[13] R. Mahalakshmi, J. Viknesh, and K. C. S. Thampatty, "Mathematical modelling of grid connected doubly fed induction generator based wind farm," in *2016 IEEE International Conference on Power Electronics, Drives and Energy Systems (PEDES)*, Dec 2016, pp. 1–6.

[14] G. Masters, *Renewable and Efficient Electric Power Systems*, 1st ed. Chicester: John Wiley and Sons, 2004.

[15] Z. Xuesong, L. Ji, and M. Youjie, "Review on wind speed model research in wind power systems dynamic analysis," in *2009 International Conference on Sustainable Power Generation and Supply*, April 2009, pp. 1–5.

[16] D. S. L. Dolan and P. W. Lehn, "Simulation model of wind turbine 3p torque oscillations due to wind shear and tower shadow," *IEEE Transactions on Energy Conversion*, vol. 21, no. 3, pp. 717–724, Sept 2006.

[17] J. H. J. Potgieter and M. J. Kamper, "Modeling and stability analysis of a direct-drive direct-grid slip-synchronous permanent-magnet wind generator," *IEEE Transactions on Industry Applications*, vol. 50, no. 3, pp. 1738–1747, June 2014.

[18] S. Gerber, "A finite element based optimisation tool for electrical machines," 2011. [Online]. Available: http://hdl.handle.net/10019.1/6635

[19] S. Gerber and R. Wang, "Evaluation of movement facilitating techniques for finite element analysis of magnetically geared electrical machines," *IEEE Transactions on Magnetics*, vol. 51, no. 2, pp. 1–6, Feb 2015.

[20] G. Vanderplaats, "Very large scale optimization." in *Vanderplaats Research and Development, Inc.*, 2007.

[21] V. Research and I. Development, "Multidisciplinary optimization with visualdoc," in *10th World Congress on Structural and Multidisciplinary Optimization*, May 2013.

[22] K. Deb, A. Pratap, S. Agarwal, and T. Meyarivan, "A fast and elitist multiobjective genetic algorithm: Nsga-ii," *IEEE Transactions on Evolutionary Computation*, vol. 6, no. 2, pp. 182–197, April 2002.

[23] D. Guo, J. Wang, J. Huang, R. Han, and M. Song, "Chaotic-nsga-ii: An effective algorithm to solve multi-objective optimization problems," in *2010 International Conference on Intelligent Computing and Integrated Systems*, Oct 2010, pp. 20–23.

[24] C. O. Onwubiko, *Introduction to engineering design optimization.* Prentice-Hall, 2000.

[25] A. D. Belegundu and T. R. Chandrupatla, *Optimization concepts and applications in engineering.* Pearson Education Taiwan, 2003.

[26] G. Harik, E. Cantú-Paz, D. E. Goldberg, and B. L. Miller, "The gambler's ruin problem, genetic algorithms, and the sizing of populations," *Evol. Comput.*, vol. 7, no. 3, pp. 231–253, Sep. 1999. [Online]. Available: http://dx.doi.org/10.1162/evco.1999.7.3.231

[27] K. D. Tran, "Elitist non-dominated sorting ga-ii (nsga-ii) as a parameter-less multi-objective genetic algorithm," in *Proceedings. IEEE SoutheastCon, 2005.*, April 2005, pp. 359–367.

[28] A. Erasmus and M. Kamper, "Multi-objective design optimisation and pareto front visualisation of radial-flux eddy current coupling for a wind generator drivetrain," in *ECCE, 2016 IEEE*, September 2016.

[29] I. ANSYS. Ansys maxwell. [Online]. Available: http://www.ansys.com

[30] D. K. Ockhuis, A. S. Erasmus, and M. J. Kamper, "Small-scale geared turbine system with slip-synchronous technology," *WindAc Africa 2016*, Jan 2016.

[31] S. Das, N. Karnik, and S. Santoso, "Time-domain modeling of tower shadow and wind shear in wind turbines," *ISRN Renewable Energy*, 2011.

[32] J. H. J. Potgieter and M. J. Kamper, "Calculation methods and effects of end-winding inductance and permanent-magnet end flux on performance prediction of nonoverlap winding permanent-magnet machines," *IEEE Transactions on Industry Applications*, vol. 50, no. 4, pp. 2458–2466, July 2014.

[33] M. J. Kamper, "Design optimisation of cageless flux barrier rotor reluctance synchronous machine," Ph.D. dissertation, 1996.

[34] V. B. Honsinger, "Theory of end-winding leakage reactance," *Transactions of the American Institute of Electrical Engineers. Part III: Power Apparatus and Systems*, vol. 78, no. 3, pp. 417–424, April 1959.

Appendices

Appendix A

Park's Transformation

The transformation of a three-phase quantity in *abc*-coordinate system to *dq*-coordinate system is known as the Park's Transformation. Written in matrix form, the Park's transformation is defined as

$$\begin{bmatrix} u_d \\ u_q \\ u_0 \end{bmatrix} = \boldsymbol{K}_P(\theta) \begin{bmatrix} u_a \\ u_b \\ u_c \end{bmatrix}, \tag{A.1}$$

where

$$\boldsymbol{K}_P(\theta) = \frac{2}{3} \begin{bmatrix} \cos\theta & \cos\left(\theta - \frac{2\pi}{3}\right) & \cos\left(\theta + \frac{2\pi}{3}\right) \\ \sin\theta & \sin\left(\theta - \frac{2\pi}{3}\right) & \sin\left(\theta + \frac{2\pi}{3}\right) \\ \frac{1}{2} & \frac{1}{2} & \frac{1}{2} \end{bmatrix}. \tag{A.2}$$

The inverse Park's transformation allows transformation from the *dq*-coordinate system to the *abc*-coordinate system. The inverse transformation is

$$\begin{bmatrix} u_a \\ u_b \\ u_c \end{bmatrix} = \boldsymbol{K}_P^{-1}(\theta) \begin{bmatrix} u_d \\ u_q \\ u_0 \end{bmatrix}, \tag{A.3}$$

where

$$\boldsymbol{K}_P^{-1}(\theta) = \frac{2}{3} \begin{bmatrix} \cos\theta & \sin\theta & 1 \\ \cos\left(\theta - \frac{2\pi}{3}\right) & \sin\left(\theta - \frac{2\pi}{3}\right) & 1 \\ \cos\left(\theta + \frac{2\pi}{3}\right) & \sin\left(\theta + \frac{2\pi}{3}\right) & 1 \end{bmatrix}. \tag{A.4}$$

Appendix B

Winding Calculations

B.1 Winding resistance

The winding resistance calculation used in this study can be found in [33]. The skin effect can ignored, which means the winding resistance is

$$R_c = \frac{2W\rho_c(l + l_e)}{n_a \cdot {}^{A_c}/_z}, \tag{B.1}$$

where

W = Number of turns in series per phase,
l = Stack length,
l_e = Average length of the end conductor,
${}^{A_c}/_z$ = Active copper area of the conductor,
ρ_c = Resistivity of the conductor,
n_a = Number of parallel circuits.

The resistivity, ρ_c, is expressed as

$$\rho_c = \rho_{20}[1 + Y_t(t_c - 20)], \tag{B.2}$$

where

t_c = Conductor temperature,
ρ_{20} = Conductor resistivity,
Y_t = Thermal coefficient.

In this study, the conductors are *1050A* aluminium, with $\rho_{20} = 2.82 \times 10^{-8}\,\Omega \cdot \text{m}$. Also, Y_t =$4.3 \times 10^{-3}\,\text{K}^{-1}$.

B.2 End-winding leakage inductance

The method used to calculate the leakage inductance component can originally be found in [34]. This method has been adapted in [32], and has also been used in this study. The

end-winding leakage inductance is

$$L_e = V_{(u)} N_{ph} d_i \left(\frac{2W k_d k_p(u)}{N_p} \right)^2 k_{e(p)}, \tag{B.3}$$

where

N_{ph} = Number of phases,
k_d = Standard distribution factor,
d_i = Stator inner diameter,
$V_{(u)}$ = Shape factor,
$k_{(p)}$ = End-winding pitch factor.

The end-windage leakage, L_e is measured in 10^{-8} H. The subscript u denotes

$u = 1$ for v-shaped end-windings,
$u = 2$ for elliptical shaped end-windings,
$u = 3$ for rectangular shaped end-windings.

The $k_{(p)}$ is calculated as

$$k_{p(1)} = \frac{3 \sin[\pi(c_s/6q)]}{4 - (c_s/3q)^2}, \tag{B.4}$$

$$k_{p(3)} = \sin\left(\pi c_s/6q\right), \tag{B.5}$$

$$k_{p(2)} \approx \tfrac{1}{2}(k_{p(1)} + k_{p(3)}), \tag{B.6}$$

where

c_s = Coil span,
q = Number of slots per pole per phase.

It should be noted that due to the high number of poles of the slip coupler, these equations are only a first approximation and are not necessarily a very accurate method of calculating the end-winding inductance.

Appendix C

Drivetrain Models

Various wind turbine drivetrain models are presented in this appendix. Each model has different levels of complexity, where the most complex model is a full drivetrain with a gearbox, turbine, generator, flexible shafts and a slip coupler. The purpose of this appendix is to present the minimum number of equations needed to create a transfer function control block only.

C.1 One-mass model

Figure C.1 shows the free-body-diagram (FBD) of a simple rotating mass. The equation of motion is

$$\tau_{in} - b_1\Omega_1 - \tau_g = J_1\frac{d\Omega_1}{dt}, \tag{C.1}$$

where

b_1 = Dissipator, usually to model windage and friction losses
J_1 = Mass moment of inertia of the flywheel.

Different inertias along the same drivetrain train can be lumped together, such that $J_e = J_1 + J_2 + \cdots J_i$.

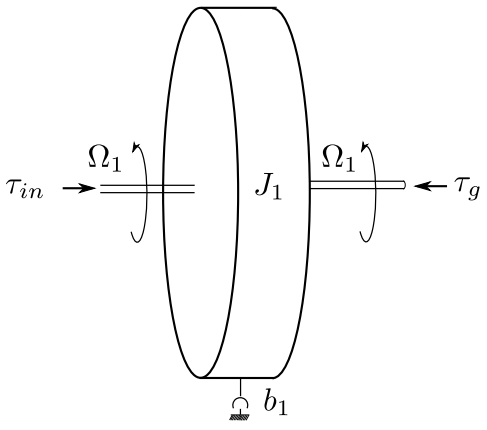

Figure C.1: Simple one-mass model with a input torque, energy dissipation and counter-torque.

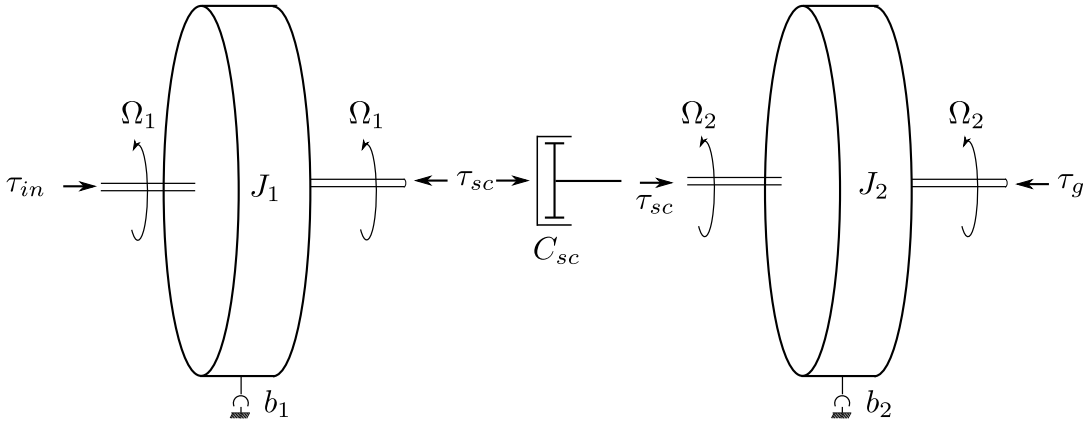

Figure C.2: Two-mass model with a slip coupler placed between two flywheels.

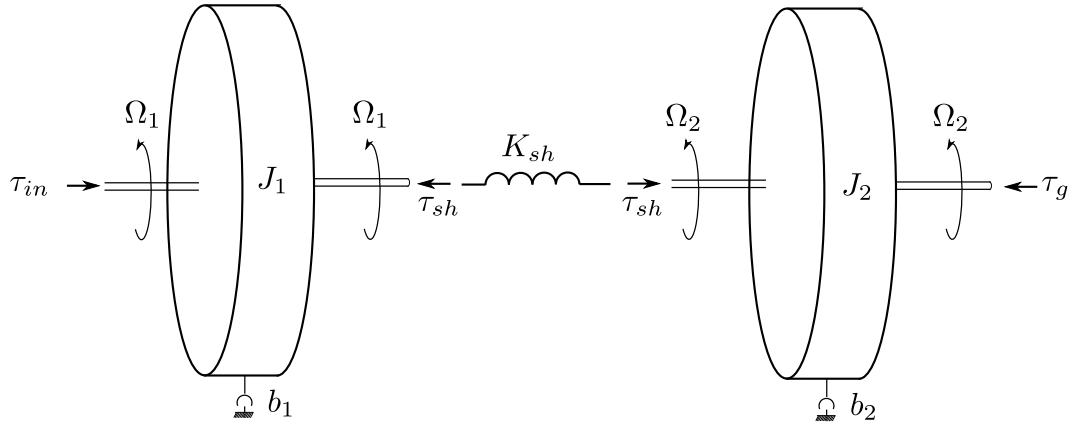

Figure C.3: Two-mass model with a flexible shaft placed between two flywheels.

C.2 Two-mass model with slip coupler

Figure C.2 shows the FBD of a two-mass model, where the slip coupler *decouples* the two flywheel inertias. The equations of motion are

$$\tau_{in} - b_1\Omega_1 - \tau_{sc} = J_1\frac{d\Omega_1}{dt}, \tag{C.2}$$

$$\tau_{sc} = C_{sc}(\Omega_1 - \Omega_2), \tag{C.3}$$

$$\tau_{sc} - b_2\Omega_2 - \tau_g = J_2\frac{d\Omega_2}{dt}, \tag{C.4}$$

where C_{sc} is the coupling constant.

C.3 Two-mass with flexible shaft

Figure C.3 shows the FBD of a two-mass model with a flexible shaft connecting the two flywheels. The equations of motion are

$$\tau_{in} - b_1\Omega_1 - \tau_{sh} = J_1\frac{d\Omega_1}{dt}, \tag{C.5}$$

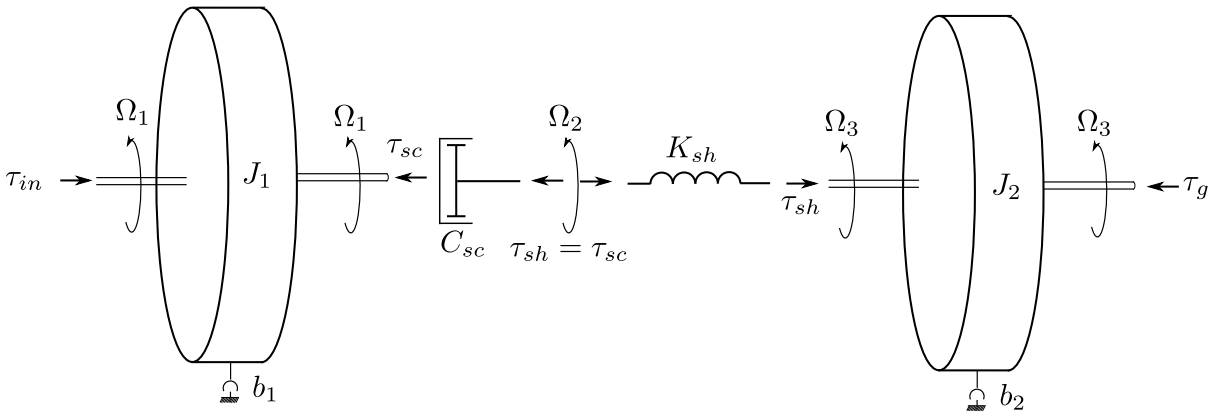

Figure C.4: Two-mass model with a slip coupler and flexible shaft placed between two flywheels.

$$\tau_{sh} = K_{sh}(\theta_1 - \theta_2), \tag{C.6}$$

$$\tau_{sh} - b_2\Omega_2 - \tau_g = J_2\frac{d\Omega_2}{dt}, \tag{C.7}$$

where K_{sh} is the shaft constant. The shaft acts as a spring, storing energy when the flywheels rotate at a constant speed, and releasing it when there is a sudden speed difference between the two. Another way to present the shaft equation is

$$\frac{d\tau_{sh}}{dt} = K_{sh}(\Omega_1 - \Omega_2). \tag{C.8}$$

C.4 Two-mass model with slip coupler and flexible shaft

Figure C.4 shows the FBD of a two-mass model with a slip coupler and flexible shaft. The equations of motion are

$$\tau_{in} - b_1\Omega_1 - \tau_{sc} = J_1\frac{d\Omega_1}{dt}, \tag{C.9}$$

$$\tau_{sc} = C_{sc}(\Omega_1 - \Omega_2), \tag{C.10}$$

$$\tau_{sc} = \tau_{sh}, \tag{C.11}$$

$$\frac{d\tau_{sh}}{dt} = K_{sh}(\Omega_2 - \Omega_3), \tag{C.12}$$

$$\tau_{sh} - b_2\Omega_3 - \tau_g = J_2\frac{d\Omega_3}{dt}. \tag{C.13}$$

From Eq. (C.10), the coupled speed term can be presented as

$$\Omega_2 = \Omega_1 - \frac{\tau_{sc}}{C_{sc}}, \tag{C.14}$$

and from Eq. (C.12), the coupled speed term is

$$\Omega_2 = \Omega_3 + \frac{1}{K_{sh}}\frac{d\tau_{sh}}{dt}. \tag{C.15}$$

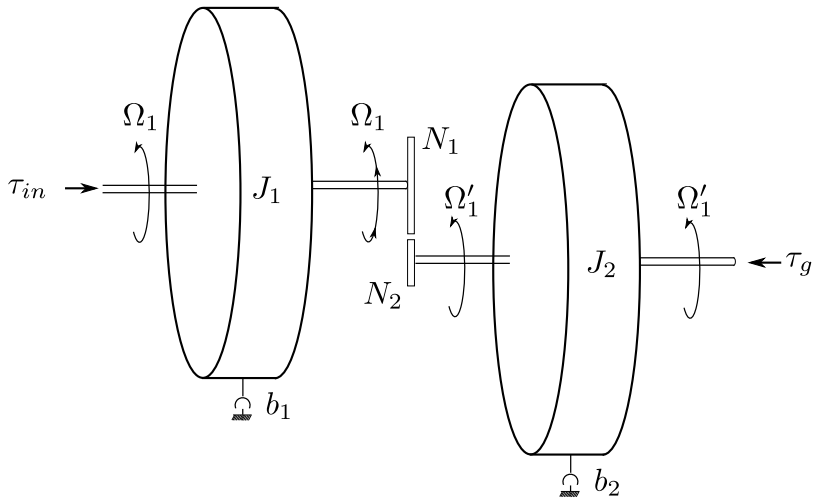

Figure C.5: Simple drivetrain model with a gearbox and two flywheels.

C.5 Simple two-mass model with a gearbox

Figure C.5 shows FBD of a drivetrain with two flywheels and a gearbox, represented by the ratio

$$G_R = \frac{N_1}{N_2} = \frac{r_1}{r_2} = \frac{\Omega_1}{\Omega_2} = \frac{\tau_{in}}{\tau'_{in}}, \tag{C.16}$$

For any ideal gearbox there is energy conservation, which means that the components on either side of the gearbox can be *reflected* to one side of the gearbox, as long as the energy remains equivalent. For inertia and the dissipator *reflected* over to the J_2 side, this means

$$J_e = J_1 \left(\frac{1}{G_R}\right)^2, \tag{C.17}$$

$$b_e = b_1 \left(\frac{1}{G_R}\right)^2. \tag{C.18}$$

For arguments sake, the left side of the gearbox with τ_{in} is referred to as the *motor-side* of the gearbox. The right side of the gearbox is referred to as the *load-side* of the gearbox. Therefore, if all the components are *reflected* to the *motor-side*, the equation of motion becomes

$$\tau_{in} - \tau'_g - (b_e)\Omega_1 = J_e \frac{d\Omega_1}{dt}, \tag{C.19}$$

where

$$b_e = b_1 + b_2 G_R^2, \tag{C.20}$$

$$J_e = J_1 + J_2 G_R^2, \tag{C.21}$$

$$\tau'_g = G_R \tau_g. \tag{C.22}$$

When the components are *reflected* to the *load-side* of the gearbox, the equation of motion becomes

$$\tau'_{in} - \tau_g - (b_e)\Omega'_1 = J_e \frac{d\Omega'_1}{dt}, \tag{C.23}$$

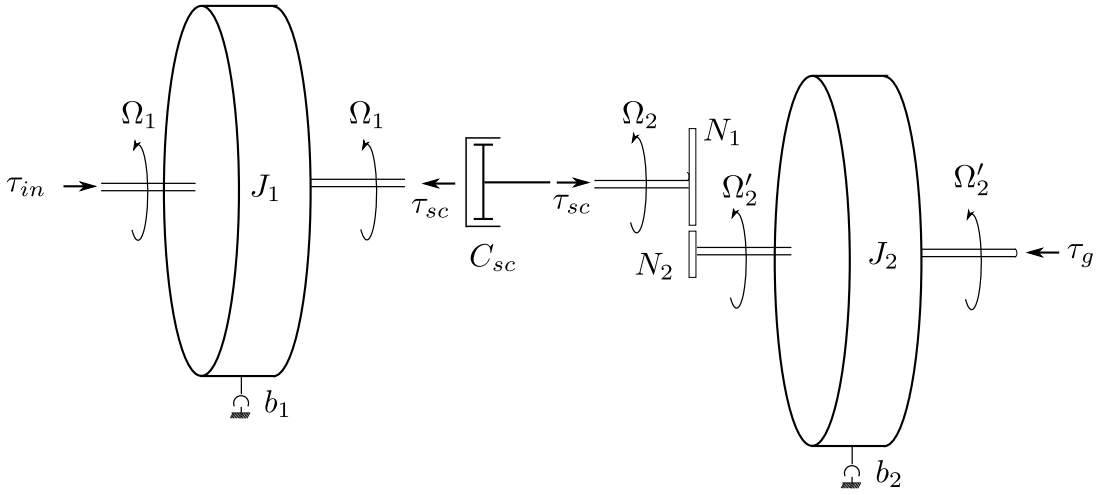

Figure C.6: Two-mass model with a gearbox, two flywheels and a slip coupler on the *motor-side* of the drivetrain.

where

$$b_e = b_1\left(\frac{1}{G_R}\right)^2 + b_2, \tag{C.24}$$

$$J_e = J_1\left(\frac{1}{G_R}\right)^2 + J_2, \tag{C.25}$$

$$\tau_{in}' = \left(\frac{1}{G_R}\right)\tau_g. \tag{C.26}$$

The litmus test for these equation is that the drivetrain should respond identically in both cases, albeit with a rotational speed difference.

C.6 Two-mass model with gearbox and slip coupler

Figure C.6 shows the FBD of a geared drivetrain with a *motor-side* slip coupler. The *load-side* inertia J_2 is *reflected* across to the *motor-side* of the drivetrain. The equations of motion for this model is

$$\tau_{in} - b_1\Omega_1 - \tau_{sc} = J_1\frac{d\Omega_1}{dt}, \tag{C.27}$$

$$\tau_{sc} = C_{sc}(\Omega_1 - \Omega_2), \tag{C.28}$$

$$\tau_{sc} - b_{2e}\Omega_2 - \tau_g' = J_{2e}\frac{d\Omega_2}{dt}, \tag{C.29}$$

where

$$\tau_g' = GR\tau_g, \tag{C.30}$$

$$b_{2e} = b_2G_R^2, \tag{C.31}$$

$$J_{2e} = J_2G_R^2. \tag{C.32}$$

Again, the slip coupler decouples the inertias of the flywheels and the inertias can, therefore, not simply be added together.

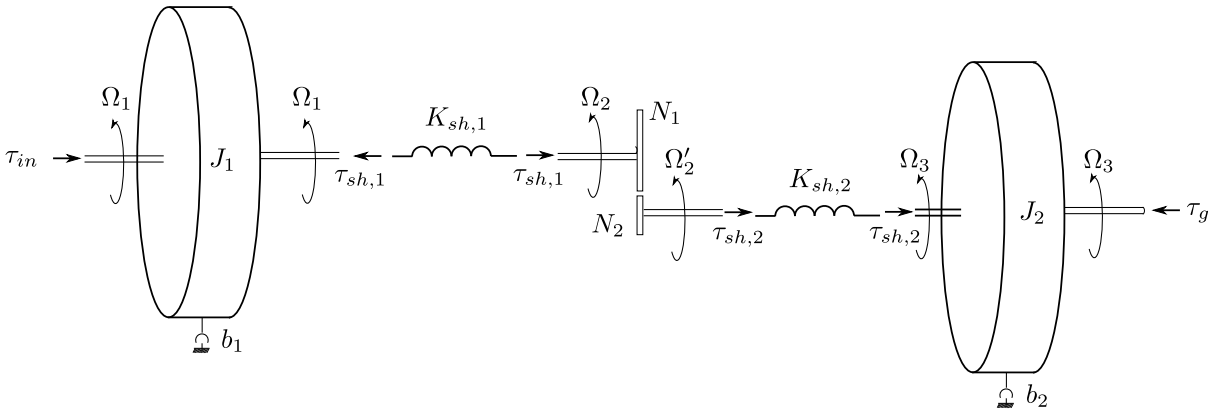

Figure C.7: Two-mass geared model with two flexible shafts running into and out of the gearbox.

C.7 Two-mass geared model with flexible shafts

Figure C.7 shows the FBD of a geared, two-mass drivetrain with two connecting flexible shafts. For this model, all components are kept in their respective positions and nothing is *reflected* across the drivetrain. The equations of motion for this model are

$$\tau_{in} - b_1\Omega_1 - \tau_{sh,1} = J_1\frac{d\Omega_1}{dt}, \tag{C.33}$$

$$\frac{d\tau_{sh,1}}{dt} = K_{sh,1}(\Omega_1 - \Omega_2), \tag{C.34}$$

$$\frac{d\tau_{sh,2}}{dt} = K_{sh,2}(G_R\Omega_2 - \Omega_3), \tag{C.35}$$

$$\tau_{sh,1} = G_R\tau_{sh,2}, \tag{C.36}$$

$$\tau_{sh,2} - b_2\Omega_3 - \tau_g = J_2\frac{d\Omega_3}{dt}. \tag{C.37}$$

From Eq. (C.34)–(C.36), the coupled speed term is

$$\Omega_2 = \frac{1}{K_{sh,2}G_R}\left[K_{sh,2}\Omega_3 + \left(\frac{1}{G_R}\frac{\tau_{sh,1}}{dt}\right)\right]. \tag{C.38}$$

It should be possible to *reflect* the *load-side* inertia and shaft across to the *motor-side*, but the overall system response will remain identical.

C.8 Two-mass geared model with slip coupler and flexible shafts

Figure C.8 shows the FBD of a geared two-mass model with a slip coupler on the *motor-side* and two flexible shafts connecting the drivetrain components. The equations of motion are

$$\tau_{in} - b_1\Omega_1 - \tau_{sc} = J_1\frac{d\Omega_1}{dt}, \tag{C.39}$$

$$\tau_{sc} = C_{sc}(\Omega_1 - \Omega_2), \tag{C.40}$$

$$\tau_{sc} = \tau_{sh,1}, \tag{C.41}$$

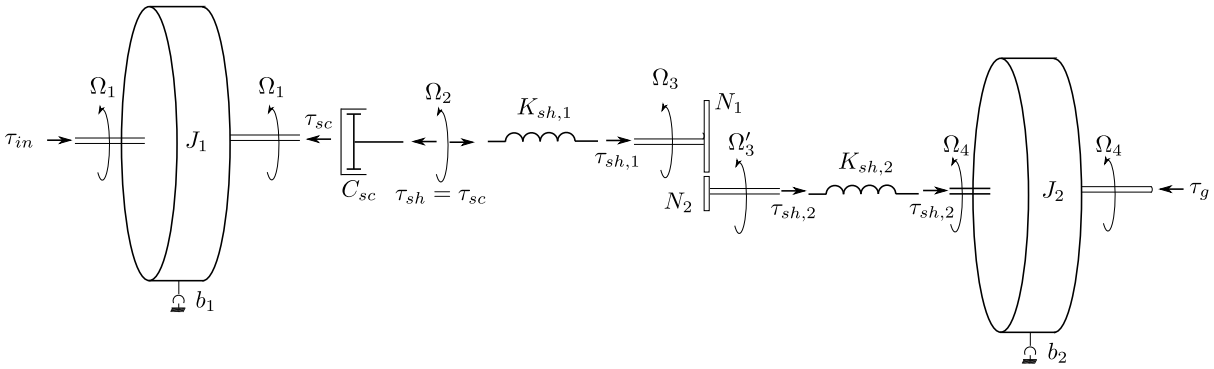

Figure C.8: Two-mass geared model with a *motor-side* slip coupler and two flexible shafts.

$$\frac{d\tau_{sh,1}}{dt} = K_{sh,1}(\Omega_2 - \Omega_3), \tag{C.42}$$

$$\tau_{sh,1} = G_R\tau_{sh,2}, \tag{C.43}$$

$$\frac{d\tau_{sh,2}}{dt} = K_{sh,2}(G_R\Omega_3 - \Omega_4), \tag{C.44}$$

$$\tau_{sh,2} - b_2\Omega_4 - \tau_g = J_2\frac{d\Omega_4}{dt}. \tag{C.45}$$

From Eq. (C.40), the first coupled speed term is

$$\Omega_2 = \frac{1}{K_{sh,1}}\frac{d\tau_{sc}}{dt} + \Omega_3, \tag{C.46}$$

and from Eq. (C.42)–(C.44), the second coupled speed term becomes

$$\Omega_3 = \frac{1}{K_{sh,2}G_R}\left[K_{sh,2}\Omega_4 + \left(\frac{1}{G_R}\frac{\tau_{sh,1}}{dt}\right)\right]. \tag{C.47}$$

Appendix D

Wind Turbine Transfer Functions

In this appendix, the two complete drivetrain transfer functions used in the study are presented. The purpose of simulating two drivetrains is to determine the effect of a slip coupler vs not having a slip coupler in place. Both models have flexible shafts on either side of the gearbox. A complete PMSG transfer function is also included.

D.1 Drivetrain transfer function with flexibles shafts

The transfer function of the full drivetrain, without a slip coupler, is shown in Figure D.1. The free-body diagram of this model is shown in Appendix C.7. The equations of motion for this model is shown in Appendix C. Both shafts are considered to have identical shaft stiffness values. The ideal shaft sizes are not investigated.

D.2 Complete drivetrain transfer function with slip coupler

Figure D.2 shows the transfer function of the full drivetrain. This drivetrain includes the slip coupler on the *rotor* side of the drivetrain. The free-body diagram of this model, as well as the equations of motion, is shown in Appendix C.8. This represents the complete drivetrain model which is used for the remainder of this study.

D.3 PMSG transfer function

The PMSG equations are presented in Chapter 5. The PMSG is directly connected to the grid, and therefore the SG needs to rotate at synchronous speed. This interaction with the grid is modelled as shown in Figure D.3. The PMSG transfer function is shown in Figure D.4.

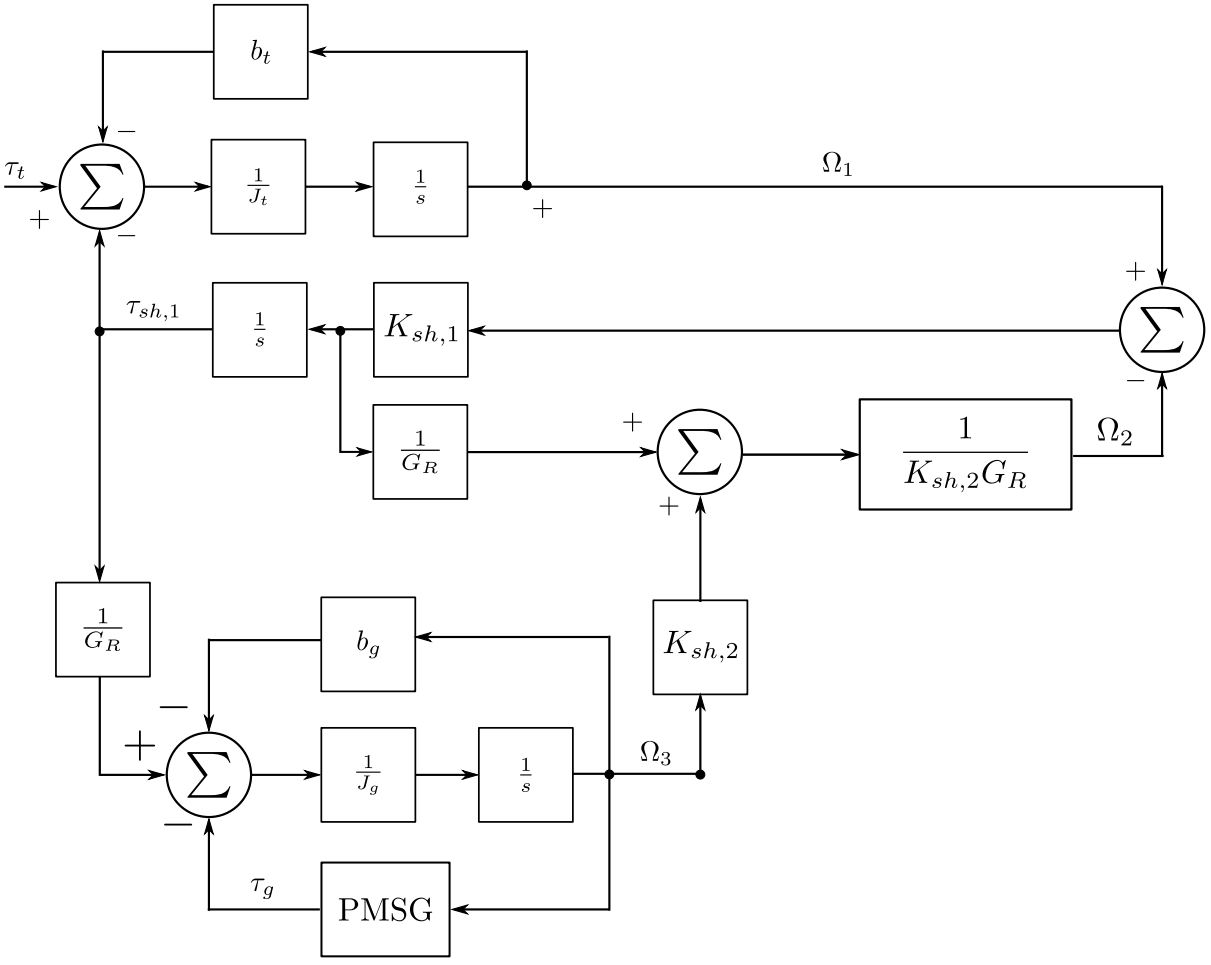

Figure D.1: Transfer function of a wind turbine drivetrain without a slip coupler.

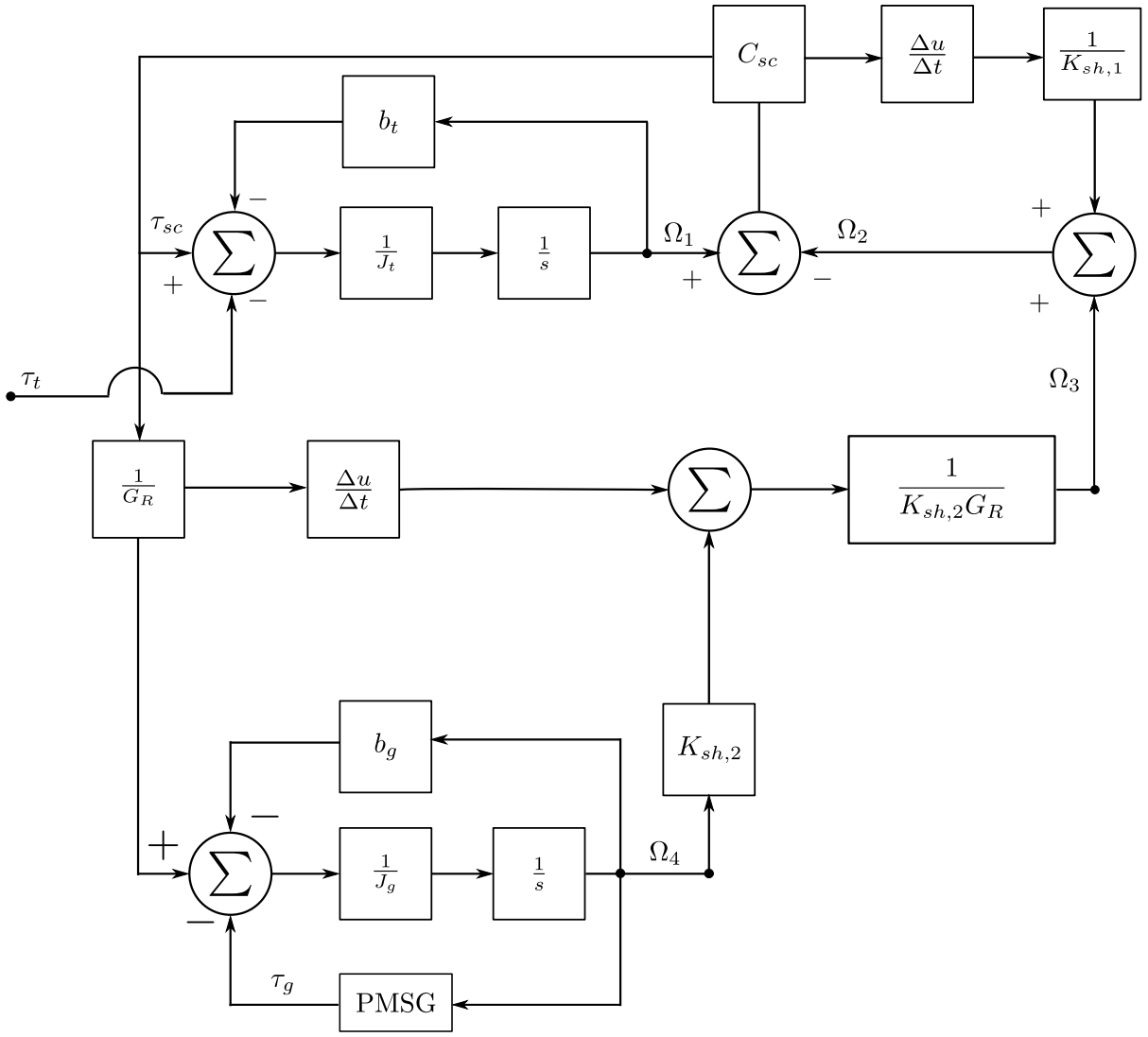

Figure D.2: Transfer function of a wind turbine drivetrain with a slip coupler and flexible shafts.

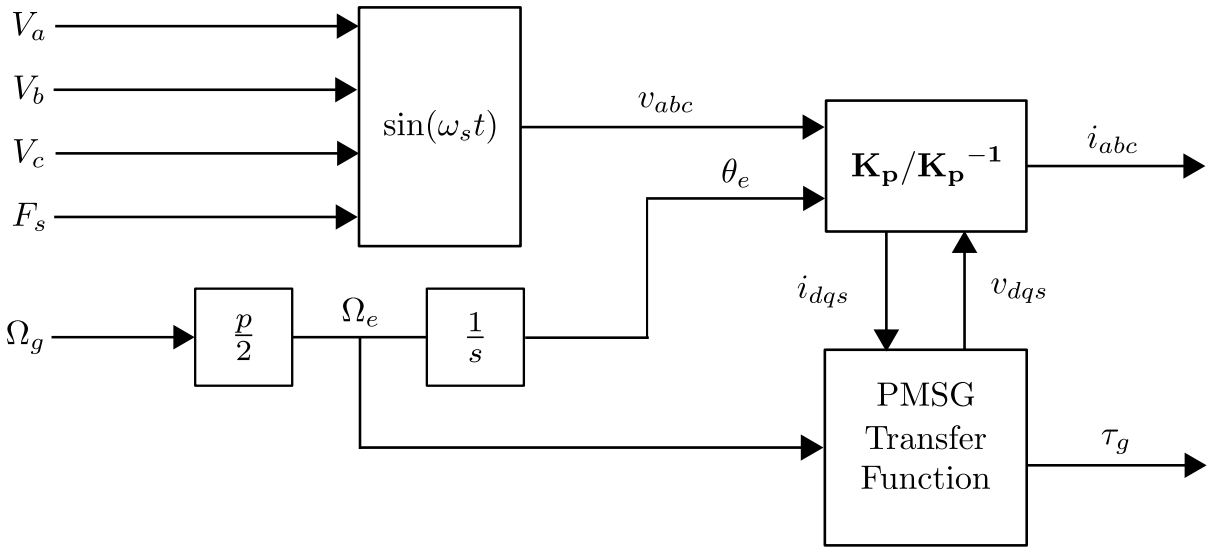

Figure D.3: Complete PMSG transfer function showing grid connection and *dq* transformation block.

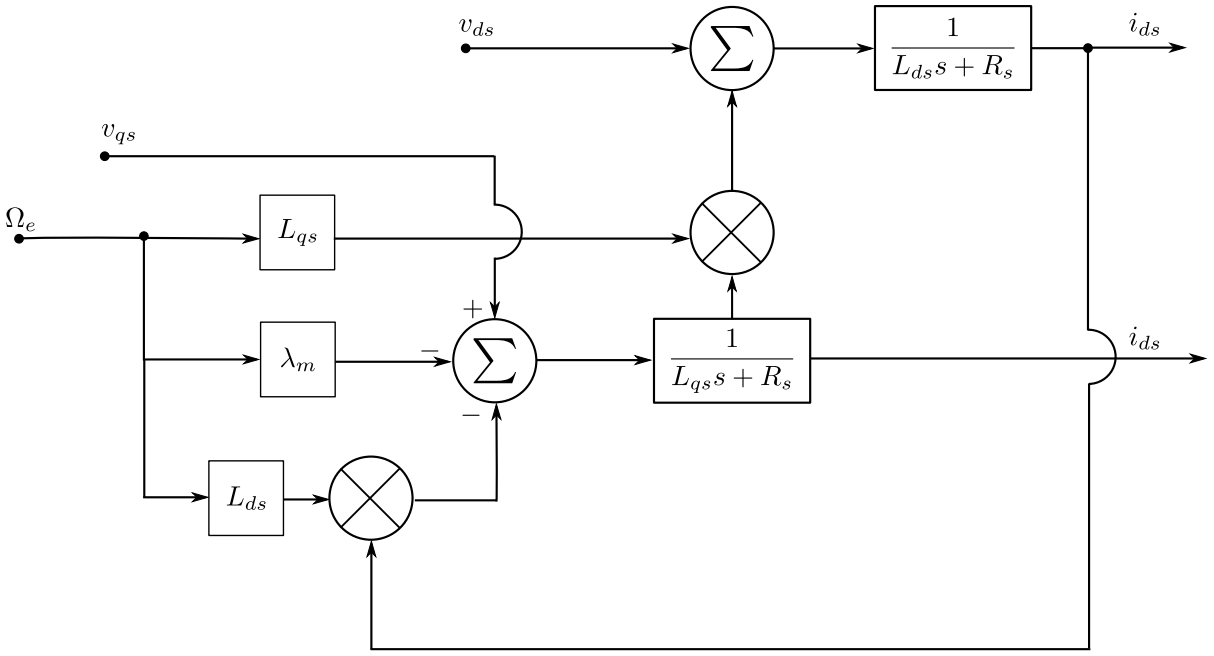

Figure D.4: PMSG transfer function.

Appendix E

Python/Semfem Script

```
#_____________________________________________________________________________#
                    #... Rotor Winding Resistance Estimation ...#
#_____________________________________________________________________________#
Y_t   = 0.0043                                          #... Material Constant ...#
Ro_20 = 2.82e-8                                      #... Density of Aluminium ...#
Ro_t  = Ro_20*(1 + Y_t*(T_coil - 20))       #... Ro at elevated temperatures ...#
W     = sf.semfem_coil_turns[0]            #... Number of series turns/phase ...#
L_e   = pi*W_end_r                   #... length of end winding (s = r*theta) ...#
A_coil  = m.acoil[1]*f_fill
R_coil  = (2*W*Ro_t*(S_length + L_e))/(A_coil)   #... bottom coil resistance ...#
R_True  = (2*W*Ro_t*(S_length))/(A_coil)         #... bottom coil resistance ...#
R_e     = (2*W*Ro_t*(L_e))/(A_coil)        #... bottom end winding resistance...#
#_____________________________________________________________________________#
                      #... End Winding Leakage Inductance ...#
#_____________________________________________________________________________#
kd    = 1                                           #... concentrated windings ...#
D_s   = R_r_out - R_t_height                    #... rotor slot inner diameter ...#
p_a   = Nm/2                                                  #... pole pairs ...#
q     = (Ns/Nm)/n_phase                              #... slots/poles/phase ...#
                                              #... equation specific constants ...#
K_p1 = (3*sin((pi*N_s)/(6*q)))/(4-(N_s/(3*q))**2)
K_p3 = sin((pi*N_s)/(6*q))
K_p2 = (K_p1 + K_p3)/2
K_e5 = 3
V_2  = 920
V_3  = 1040
L_end  = V_2*n_phase*D_s*(((W*kd*K_p2)/(p_a))**2)*K_e5*1e-8 #... Henry/Phase ...#
#_____________________________________________________________________________#
```

```
                    #... Initial Current Estimation ...#
#_____________________________________________________________________________#
w_out  = n_rated*(2*pi/60)                          #... convert to rad/s ...#
w_in   = w_out/(1-s_max)
w_slip   = w_in - w_out                                   #... slip speed ...#
w_slip_e = (Nm/2)*w_slip                        #... electrical slip speed ...#
f_slip   = w_slip_e/(2*pi)                        #... slip frequency ...#
print ("Slip Frequency: %s" % f_slip)
P_cu          = T_rated*w_slip                    #... mechanical power ...#
i_c_initial   = sqrt((2*P_cu)/(n_phase*R_coil))   #... lower coil current ...#
Flm = zeros((nstep, 1))
Id_r    = zeros((nstep, 1))
Iq_r    = zeros((nstep, 1))
Id_r1 = zeros((nstep, 1))
Iq_r1 = zeros((nstep, 1))
Iq_temp = i_c_initial
Id_temp = 0
position = zeros(nstep)
e_position = zeros(nstep)
#_____________________________________________________________________________#
                    #... dq-Flux Itteration Method ...#
#_____________________________________________________________________________#
for n in xrange(n_itteration):
    Lqr = zeros((nstep, 1))
    Ldr = zeros((nstep, 1))
    fld_r   = zeros((nstep, 1))
    flq_r   = zeros((nstep, 1))
    #... ABC currents ...#
    ia = zeros(n_phase/3)
    ib = zeros(n_phase/3)
    ic = zeros(n_phase/3)
    #... Initial currents ...#
    for i in xrange(nstep):
        c  = 1
        s_vec = -(i/(nstep))*pm_pitch_angle*3          #...rotation angle ...#
        #... Rotor Position ...#
        sf.semfem_p_vec[i,0] = s_vec + (6)*(pi/180)*(2/Nm)
        sf.semfem_p_vec[i,1] = 0                    #... Stator Position ...#
        position[i] = s_vec*180/pi
```

```
        offset = pi/2
        e_position[i] = position[i]*(Nm/2)

        for x in xrange(int(n_phase/3)):
            if (c % 2 == 0):
                E_angle =  x*R_s_pitch + s_vec - pi/2 #... Electrical Angle ...#
            else:
                E_angle =  x*R_s_pitch + s_vec
            ia[x], ib[x], ic[x] = sf.dq_abc(Id_temp, Iq_temp, E_angle*(Nm/2))
               #... Assigning currents to phases ...#
            sf.semfem_i_vec[i,x]                      = ia[x]
            sf.semfem_i_vec[i,x+int((2/3)*n_phase)]   = ib[x]
            sf.semfem_i_vec[i,x+int((1/3)*n_phase)]   = ic[x]
            c += 1

    bs_time  = time.time()
    if (SOLVER == 'BAND'):
        m = sf.band_solver(m, sf.GAUSS, 1)
    elif (SOLVER == 'AGE'):
        m = sf.age_solver(m, sf.GAUSS)
    solver_time =  time.time() - bs_time

    m_time = time.time()
    #...dq- flux and current calculation ...#
    for i in xrange(nstep):
        s_vec = -(i/(nstep))*pm_pitch_angle*3
        E_angle =  s_vec
        fld_r[i,0], flq_r[i,0]  = sf.abc_dq(sf.semfem_flink_vec[i,0], #...
         sf.semfem_flink_vec[i,int((2/3)*n_phase)], #...
         sf.semfem_flink_vec[i,int((1/3)*n_phase)], E_angle*(Nm/2) )
        Id_r[i,0], Iq_r[i,0]    = sf.abc_dq(sf.semfem_i_vec[i,0], #...
         sf.semfem_i_vec[i, int((2/3)*n_phase)], #...
         sf.semfem_i_vec[i, int((1/3)*n_phase)], E_angle*(Nm/2) )
              #_____________________________________________________#
                            #... Ld & Lq Method ...#
              #_____________________________________________________#
    if (n == 0):
        Flm = fld_r
        Lqr = flq_r/Iq_r + L_end
```

```
    Ldr = Lqr
elif (n != 0):
    Lqr = flq_r/Iq_r + L_end
    Ldr = (fld_r - Flm)/Id_r + L_end
                    #... calculating new current values ...#
Denominator = (R_coil**2+(w_slip_e**2)*Lqr[:,0]*Ldr[:,0])
Id_r1[:,0] = (-(w_slip_e**2)*Lqr[:,0]*Flm[:,0])/Denominator
Iq_r1[:,0] = (-w_slip_e*Flm[:,0]*R_coil)/Denominator

Id_temp = mean(Id_r1[:,0])
Iq_temp = mean(Iq_r1[:,0])
method_time = m_time - time.time()
```